Study on Low-Temperature Graphitization in Solid Phase Reaction

固相反応における低温グラフェン化に関する研究

Nagoya Institute of Technology

By

Sahar Elnobi Ibrahim Ali

Thesis submitted for the award of the Doctoral (PhD) Degree of

Engineering

Department of Physicals Science and Engineering

Graduate School of Engineering

Nagoya Institute of Technology

Nagoya

Japan

Supervisor: Prof. Dr. Masaki Tanemura

March 2021

Dedicated to my beloved mother and father, teachers, friends and husband!

Declaration

I confirm that the work presented in this thesis is my own. Where I have consulted the work of others, it has been clearly stated.

Contents

SUBJECT **PAGES**

CHAPTER 2

EXPERIMENTAL METHODS AND CHARACTERIZATIONS

CHAPTER 3

CHAPTER 4

CHAPTER 5

CHAPTER 6

CONCLUSION AND FUTURE WORK

Acknowledgments

Alhamdulillah,

Up to this moment that putting my hands to type acknowledgments for thesis, I can't believe how fast time goes by. On this short page, the greatest thanks and gratitude at first of all to ALLAH who always helps and guides me to accomplish this work. I want to gratitude all surrounding me. This thesis would not have been possible without the help of many people.

I express my sincere thanks to my supervisor, ***Prof. Dr. Masaki Tanemura***, Physics Science, and Engineering Dept., Nagoya Institute of Technology, Japan, for his esteemed supervision, great help, incessant support, guidance, great efforts, and valuable advice in supervising my doctoral researches. I would also like to thank ***Prof. Dr. Golap Kalita*** for his kind support, ***Prof. Dr. Tetsuo Soga*** and ***Prof. Dr. Toshio Kawahara*** for their careful reading of this thesis. Their comments and suggestions were the main sources for the essential correction with improvement in this form.

I would like to thank ***Dr. Subash Sharma*** for his assists and cooperation in completing my research studies. I am also thankful to my colleagues ***Dr. Mona Ibrahim*** and ***Mr. Balaram Paudel Jaisi*** for their cooperation, support, and encouragement. I would especially thankful to all masters and bachelor students of my lab for their help. They were always there to support me with motivations and advice and make my student life become cheerful and enjoyable moments.

My father and mother, thanks for your support and unconditional love. A special thanks to my lovely daughters ***Menna and Mai*** and my beloved husband ***Amr Attia***. He is the backbone and the origin of my happiness. His constant love and support without any complaint have enabled me to successfully end my Ph.D.

Sahar Elnobi

Abstract

Nowadays, graphitized carbon including graphene is recently one of the most advanced materials for up-scaling in environment-friendly industrial applications due to its incomparable electronic and optical properties, high thermal conductivity, and excellent mechanical properties. The prerequisite for a broader range of applications is to lower its growth temperature. Thus, its low-temperature growth is one of the challenges in the graphene research field. Many techniques have been utilized to fabricate this two-dimensional material including graphite exfoliation, chemical vapor deposition (CVD), and solid-phase reaction. In the solid-phase reaction method, a solid carbon source, such as a polymer film or an amorphous carbon (a-C) film, is annealed on a metal catalyst substrate, e.g. nickel (Ni) and cobalt (Co). In this dissertation, I challenged the synthesis of graphitized nanocarbon at ultra-low temperatures using metallic nanoparticles (NPs). Also, I have challenged to fabricate Li-embedded carbon nanocomposites (Li-C NCs) for easy and safe handling for the in-situ transmission electron microscopy (TEM) observation. The movement of Li atoms during the in-situ TEM observation may induce the graphitization of a-C. This will be also the strategy for low-temperature graphitization.

Chapter 1 includes the introduction of the history, structure, and unique properties of graphene and potential applications. Graphene synthesis techniques, motivation, and the purpose of the thesis are also included in this chapter.

Chapter 2 discusses the experimental methods (magnetron sputtering and ion beam deposition) and the detailed characterization process used in the present work.

Chapter 3 reports a great decrease in graphitization temperature for well-known catalyst Ni using NP form. Amorphous carbon (a-C) films with Ni NPs were deposited onto microgrids and SiO_2/Si substrate by a simple one-step magnetron sputtering method. The a-C surrounding and in-between the Ni NPs started to be graphitized during the film deposition even at room temperature (RT) and at 50^{o}C. Based on the detailed high resolution TEM (HR-TEM) analyses, the decreased oxidation for NPs and the enhanced solubility of carbon into Ni NPs were believed to be keys for the lower temperature graphitization.

In Chapter 4, encouraged by the success in the previous chapter, Co which possesses higher catalytic activity in graphitization for the chemical vapor deposition (CVD) method than Ni was attempted. Amorphous-C films containing metallic Co NPs were deposited by a simple one-step sputter-deposition technique at RT. The graphitized layers at around and between Co NPs in the amorphous C matrix were confirmed by HR-TEM with a fast Fourier-transform (FFT). The 2D peak and graphite (002) peak were clearly observed in Raman spectra and X-ray diffraction (XRD), respectively, for the Co-C film deposited on SiO_2/Si. The X-ray photoelectron spectroscopy (XPS) analyses were used to determine the metallic state of Co NPs and sp^2 graphitization in the film. From a comparison in catalytic activity in the RT graphitization between Ni and Co NPs, Co NPs were concluded to be more suitable than Ni NPs for the ultra-low temperature graphitization.

In Chapter 5, encouraged by the finding in the previous chapters that the metallic state is preserved for the NPs dispersed in carbon matrix, metallic Li-embedded in carbon was challenged by the ion irradiation method. Vertically aligned conical Li-C NCs, sometimes with a nanofiber on top, grew on a graphite foil. As was expected, metallic Li was preserved inside the carbon matrix. Li-C NCs were found to be highly stable under ambient conditions, making TEM characterization possible without any sophisticated handling in glovebox. The developed

Li-C NCs was also extendable to the synthesis of stable Li-C NCs in the film form. In fact, no significant loss in crystallinity and change in morphology of the Li-C film was observed after heating at 300^{o}C for 10 min. The next step will be the in situ TEM observation of the low temperature graphitization during charge-discharge process for this Li-C NCs. This will be helpful also for the development of the novel electrode materials for future Li-air batteries.

Chapter 6 summarizes this work and explores future prospects.

List of Figures

Chapter 1

1. Introduction

Technology has progressed unexpectedly in the past few decades, guided largely by the rapid advancement of information technology (IT). This rapid development has already even reached the advanced technology of achieving and managing the smaller component's structural and functional parts below the microscale stage. This expands the opportunity to recognize products that have better integration density and speed, more potent and lighter, however on the identical time devour low energy in addition to costs of production. The nanotechnology concept has become as famous and wide withinside the mainmast media, even reaching the overall public and attracting greater funding and investment in this research area. One of the critical scientific aspects that need to be considered, in this nanotechnology field, is nanomaterials research which is the fundamental information that important for further development in the field of application.

1.1. Nanomaterials

Nanomaterials have been a subject that has drawn a great deal of interest in recent years due to their remarkable mechanical, electrical, optical, and magnetic properties. As the technology to monitor and manipulate these materials is progressively improved, they exhibit unlimited potential, which is predictable to be used in a wide variety of applications. There may be various kinds of nanomaterials, such as ceramics, polymers, metals, non-metals, and composite materials. In principle, nanomaterials are characterized as a group of materials where at least one dimension is less than approximately 100 nm. A nanometer is one-millionth of a millimeter-approximately 100,000 times smaller than a human hair's diameter. This is an entirely different feature that cannot be seen through naked eyes or optical microscopes.

Nanomaterials have actually been unintentionally manufactured and used since a long time ago. Recent studies have shown, for instance, that nanomaterials play an important role in the Lycurgus cup and Damascus steel [1, 2]. The Romans' Lycurgus cup contains NPs of silver and gold with a diameter of ~70 nm, which gives optical effects that create a variety of colors. On the other hand, Damascus, the blades that were used by the Muslims in the crusades, which have a distinctive wavy banding pattern known as damask, remarkable mechanical properties, and an extraordinarily sharp cutting edge contained nanowires and multi-walled carbon nanotubes in the material. The advancement of nanotechnology has been motivated by the refining of microscopies, such as scanning tunneling microscopy and transmission electron microscopy (TEM), which open up the nano-level direction of discovery.

1.2. Carbon

Carbon is considered one of the fundamental elements of all recognized types of organic life, and one of the most abundant elements on earth as well. Bulk carbons also referred to as graphite, were very well known as the lead for pencils. Recently, carbon materials have been developed to form a brand of the inorganic non-metallic material that has an important place in materials science. Due to its valency, carbon is capable of forming several allotropes [**Fig.1.1**]. So, various graphite structures are divided into different uses and features. For example, a mixture of crystalline carbon structures known as a-C. In the fifteenth century, a significant quantity of graphite was discovered in England, which became exceptionally pure crystal. Graphite is known to be one of the oldest soft allotropes materials and is used as brake linings, lead of pencils, and electrodes. Moreover, graphite-based materials can be used for the manufacture of carbon fibers with extremely strong mechanical properties, making them ideal for aeronautical products and sports equipment [3]. By the late 18th century, it was discovered that graphite and diamonds were in various aspects of the structure of carbon. The 0-dimension

(0D) of carbon allotropes, discovered in 1985 by British chemist H.W. Kroto and a US scientist R. E. Smalley, is known as (C60) fullerene or buckyballs. Their new material is composed of a stacked graphene sheet of connected hexagonal rings and has a nanoscale spherical structure. The distinctive properties and characteristics of fullerene often generate intense research interest as the next generation materials. These results then lead to the manufacture of carbon nanofibers (CNFs) [4, 5].

The first observation of 1-dimensional (1D) carbon nanotubes (CNT) graphite allotropes in 1991 were discovered by Iijima, which generates enormous interest as next-generation materials due to its novel properties, extraordinary mechanical, electrical, and chemical characteristics [6, 7]. CNTs may be graded as single-walled CNTs (SWCNTs), double-walled CNTs (DWCNTs), and multiwalled CNTs (MWCNTs) depending on the number of walls. Moreover, according to the rolling up angle ("chiral vector"), they are referred to as armchair, zigzag, and chiral nanotubes. In fact, because of the fact that they exhibit prominent electrical and mechanical properties, the invention of CNTs has led to serious research on carbon-based materials. Recently, a 2-dimensional (2D) graphite structure known as graphene was discovered in 2004. Graphene is believed to be the post-silicon in electronic devices due to the tunable band gap, excellent mechanical, chemical, and optical properties, and electrical properties [8].

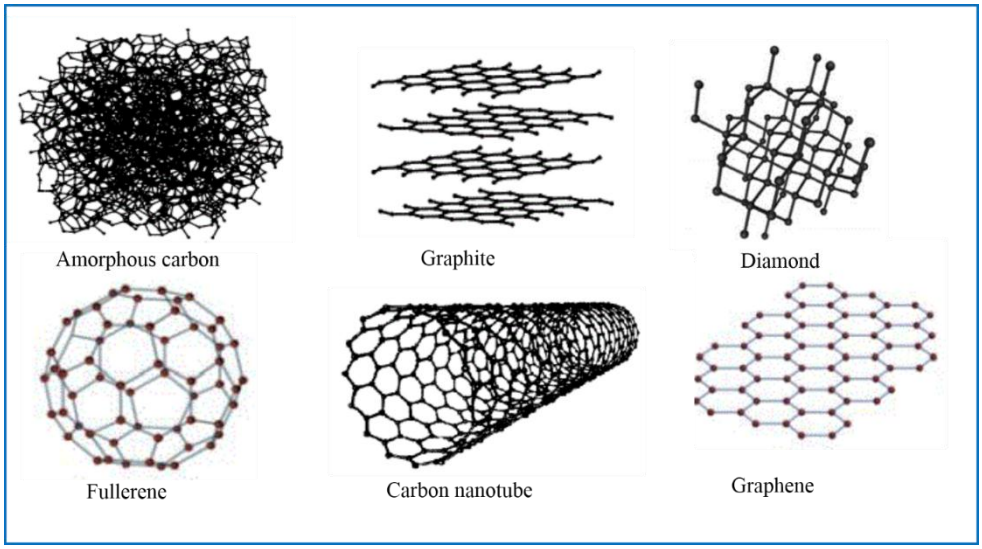

Figure 1.1: Different types of carbon allotropes [9].

The in situ observation studies for ion-induced CNFs only first been reported in 2008. The field emission (FE) measurement of single CNF by in situ scanning electron microscopy (SEM) was demonstrated by Sim et al in the different separation gaps from 20-550 nm [10]. They noticed that the field enhancement factor was related to the electrode separations. Moreover, the maximum current flow onto the single CNF was registered at 15 μm before the CNF began to fracture. One of the techniques to obtain that essential knowledge is in situ TEM analysis. Wang et al, for example, reported structural damage by in situ TEM to single multi-wall carbon nanotubes (MWCNT) during the FE process [11]. They found that MWCNT layers were removed one by one, resulting in the emitter tip become sharper during the FE process. For electron imaging applications, De Jonge et al investigated the FE properties of MWCNT. They reported that a single MWCNT emits most of the emission current into a single narrow beam [12]. In situ FE measurement of a single CNT was also performed by Smith et al to research the effects of distance between anode and cathode on FE properties [13]. They found that the field enhancement factor of the emitter would also decrease as the distance difference decreased, which they believed to be equivalent to a wide area of CNT FE measurements. This finding was consistent with the results recorded by Sim et al, who demonstrated the single CNF

FE measurement [14]. The previous work in my laboratory showed that different kinds of metal elements could be incorporated into ion-induced amorphous CNFs by the simultaneous supply of metal particles during the growth of CNFs and that the structural transformation could be induced by high electron current flow along those metal-incorporated CNFs during FE process [15, 16].

1.3. Introduction to Graphene

Graphene has been one of the most studied subjects in physics and material science in the last few years [17, 18]. Past physics hypes on other carbon allotropes such as fullerenes and nanotubes outweigh the tremendous rise in publications each year [19]. A 2D carbon material, graphene [**Fig. 1.1**], was discovered by the Manchester Group in 2004 [8]. They simply put a graphite flake on scotch tape and peel it off repeatedly until the thinnest flakes are found. The Nobel Prize in Physics 2010 was jointly awarded to Geim and Novoselov for "groundbreaking studies on the 2D material graphene" because of their outstanding and innovative research work. "The term" graphene "incorporates the information of “graph” due to graphite and" ene "due to double carbon-carbon bonds [20]. Since then, due to its outstanding electrical and mechanical properties, it has also attracted considerable interest [21].

Graphene also has several specific features, such as bipolar supercurrent, relativistic particle chiral tunneling, absence of Anderson position, and irregular quantum Hall effect [8]. These specific characters make it possible to provide a research platform for quantum mechanics and a condensed matter physics. The single graphene layer has excellent electronic properties and is a semimetal or zero-gap semiconductor. Graphene's electron mobility is very high; it is approximately 10 times faster than a commercial silicon wafer. A significant application is that graphene can be used as a transparent electrode that can be used widely in

liquid crystal display (LCD), organic light-emitting display (OLED) or organic solar cells in the future [22].

1.4. Structure and Properties of Graphene

1.4.1. Structure

It is well known that nanomaterials' morphologies, sizes, surface area, and phases have a great effect on their properties and practical applications. Therefore, great attention has been drawn to the synthesis of nanostructured materials, including CNTs, CNFs, and graphene [23]. The use of carbon materials for a large number of applications comes from the unique variety of structures and properties of the materials that provide a chemical connection to nanostructures, crystallite arrangement, and microstructures between carbon atoms. The three-dimensional (3D) crystalline forms of the element carbon are both diamond and graphite. Graphite is made up entirely of hybridized sp^2 bonds, while diamond consists of hybridized sp^3 bonds. Graphene is a single layer of sp^2 hybridized carbon atoms, 2D, structured in a hexagonal lattice structure, as shown in **Fig. 1. 2.** Each atom has four bonds: one σ bond with each of its three neighbors and one π-bond that is oriented out of plane [24]. The carbon atoms in diamond are arranged in a lattice with a face-centered cubic (fcc) crystal structure that has excellent physical characteristics, most of which derive from the strong covalent bonding (sp^3 hybridization) between its atoms. In the presence of an external perturbation (another atom) and one s-orbital and three p-orbitals (p_x, p_y, p_z) being formed, four valance electrons of C atom in 2s and 2p states excited together, for sp^2 hybridization. One s-orbital and two p-orbitals lead to the sp^2 hybridization, which results in a graphene honeycomb structure planer assembly with a characteristic angle of 120^o between the hybridized orbitals (covalent σ-bonds). The remaining p-orbital perpendicular to the hybridized network contributes to the weak interaction of van der Waals between graphene layers with the π-bond thus formed [**Fig. 1.3(b)**] [25].

In 1947, for the definition of the 3D material, P. R. Wallace used graphene as a basic theoretical model and studied the band structure of graphite [26]. The carbon atoms are arranged into a hexagonal lattice in each layer with a separation of 1.42 Å [**Fig. 1.3(a)**], (sp^2 hybridization), and 3.37 Å [26, 27] is the distance between planes (layers). In essence, the two known forms of graphite, α (hexagonal) and β (rhombohedral), have the same physical properties. Graphitic carbon nanomaterials can be individuals from the same group because they consist mainly of sp^2 carbon atoms arranged in a hexagonal lattice. Inside the graphene sheet, Wallace successfully defined graphene as a zero bandgap semiconductor (semi-metal) and with an extraordinarily high mean free path [25, 28]. The linear energy distribution around the Dirac point [**Fig. 1.3 (c)**]. Due to the 2D honeycomb structure of graphene (lattice constant 2.46 Å) distinguishes this material from other property semiconductors and thus paves the avenues range of application [9, 29].

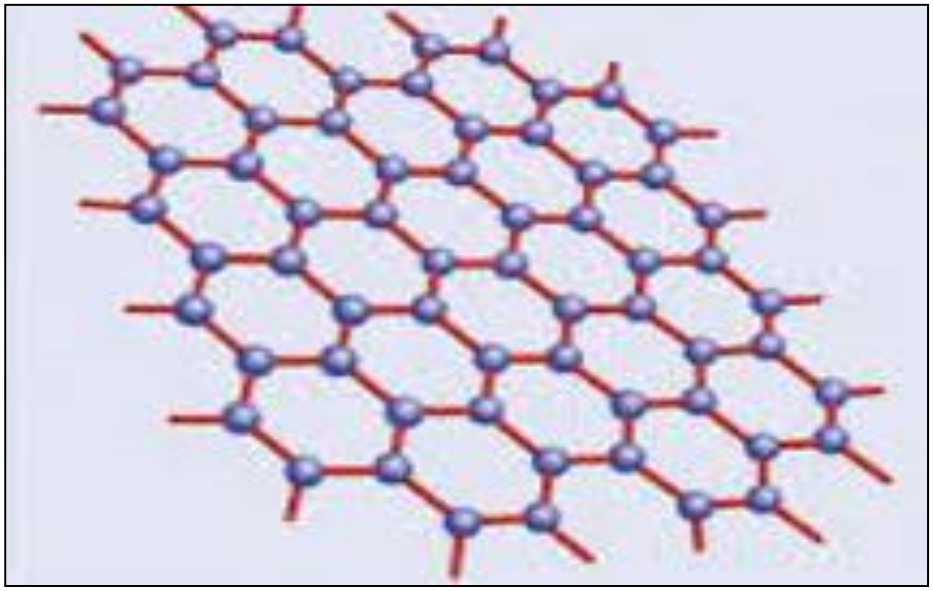

Figure 1.2: The structure of graphene [9].

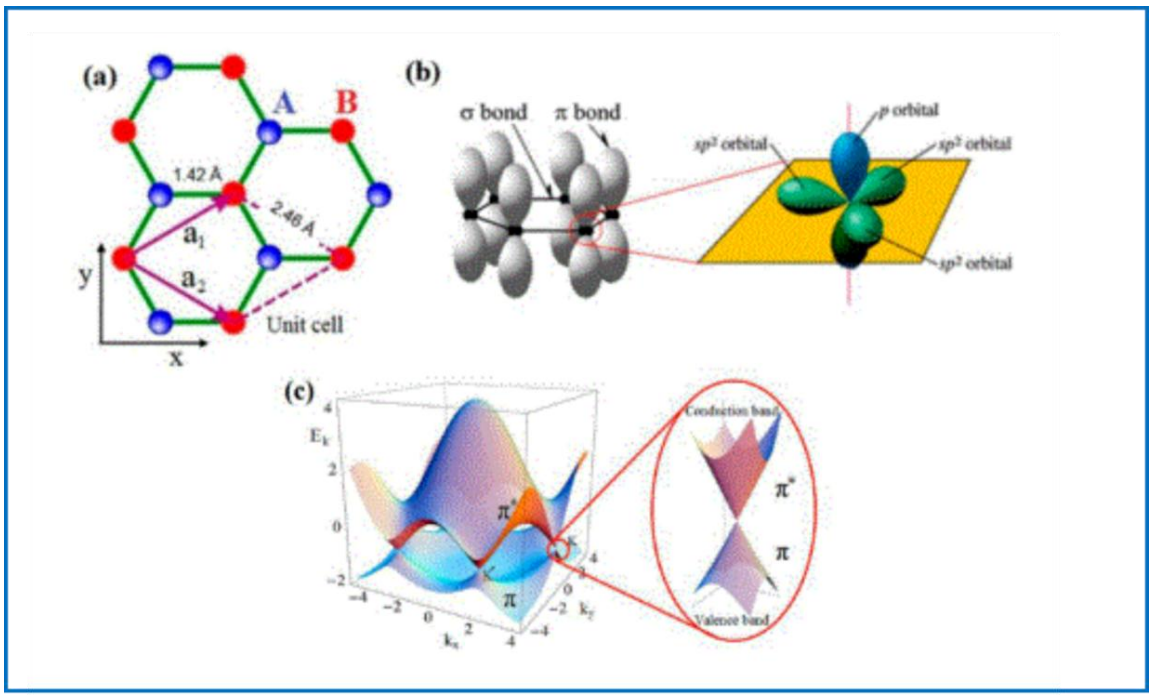

Figure 1.3: (a) The crystal structure of single layer graphene. (b) π-bond σ-bonds configuration in a honeycomb. (c) Electronic band structure of graphene. [25].

1.4.2. Properties of Graphene

1.4.2.1. Electrical and Electronical Properties

Each atom of carbon (C) is bound to three other atoms of C in graphene and leaves one free electron. Graphene has an electrical conductivity of 6000 S cm^{-1} [30]. In addition, at low temperatures, the resistance of graphene is 10^{-6} Ω cm. Graphene is a semiconductor with a zero band gap [31]. Therefore, if extrinsic dispersion in graphene is eliminated, the electronic mobility of 200,000 cm^2 V^{-1} S^{-1} can be achieved at RT [32–34]. In suspended graphene samples, Du et al [30] recorded low-temperature mobility approaching 200,000 cm^2 $V^{-1}S^{-1}$ for carrier densities below 5×10^{9} cm^{-2}.

1.4.2.2. Optical Properties

The remarkable optical properties of graphene include its high transmittance of 97.7% of visible light [35]. This characteristic makes graphene an appropriate material for the manufacture of transparent and flexible electrodes [36], touch screens [37], photodetectors [38], and solar cells [39].

1.4.2.3. Mechanical Properties

One of the hardest and strongest materials known is a single-layer of graphene. Graphene is harder than a diamond and stronger than steel (~300 times). Young's graphene modulus with an ultimate tensile strength of 130 GPa [40] is a remarkably high ~1 TPa. This nanosheet can be extended up to 20 % of its initial length, even though graphene is robust. This robustness may be used for strengthening other materials [41] or for manufacturing composite materials with graphene [42]. The mechanically powerful composite material can be fabricated with graphene with these mechanical properties.

1.4.2.4. Thermal Properties

Graphene has very high thermal conductivity. The experimental thermal conductivity of bulk graphite was reported as 2000 W m^{-1} K^{-1} by Ho et al. [43]. Nika et al. compared the thermal conductivity of bulk graphite and graphene, the thermal conductivity of single-layer graphene depends on the flake size and ranges from 3000-5000 W m^{-1} K^{-1} [44]. The thermal conductivity of graphene is 5000 W m^{-1} K^{-1} whereas, the thermal conductivity of single-walled nanotube (SWNT) is 3500 W m^{-1} K^{-1} [45]. The graphene thermal conductivity upper limit was estimated to be 6600 W m^{-1} K^{-1} [46].

1.4.2.5. Chemical Properties

While graphite is regarded as one of the most chemically inert materials, graphene possesses an imperfect chemical inertness due to its honeycomb structure and its composition

of only carbon atoms [47]. Bunch et al [48] found that a monolayer graphene membrane is impermeable to standard gases, including helium. Graphene can also be used as a protective coating that inhibits underlying metal corrosion [49]. In addition, by nitrogen species, graphene nanoribbons were covalently functionalized by high-power electric Joule heating in ammonia gas, resulting in n-type electronic doping consistent with theory [50].

1.5. Methods of Graphene Synthesis

There are several methods to synthesize graphene for various purposes. An effective synthesis technique can be chosen based on the availability of facilities and the quality of the required graphene. Graphene samples were directly achieved from graphite and are therefore of very high quality. However, these samples are limited to a few microns in size [17], and it is very difficult to monitor the flake size and layer number even at the level of expertise. Further investigation is highly desirable in order to make graphene more reliable in all respects. The mainstream synthesis process practiced since the discovery of graphene in 2004 is summarized briefly in **Table 1.1.**

Table 1.1: Summary of the techniques of graphene synthesis with their unique advantages [51].

Technique	Brief Description	Product details	Advantage	Disadvantage
Micro Mechanical exfoliation	Graphene layers exfoliate by using sticky tape	Mono to few layered flakes size: (μm-cm)	Best for Fundamental research, High quality, simple and cheap.	Varied number of layers, small scale production, inconsistent
Liquid phase exfoliation (LPE)	Specialized solvent is utilized for the exfoliation of graphite by ultra-sonication	Mono to few layer graphene flakes dispersed in liquid Size: up to μm	Easy and time efficient method, cheap and scalable, produced highly concentrated graphene oxide suspension	Uncontrollable size and layer number, significant defects, extraction from liquid essential
Reduction of graphene oxide (GO)	Chemically reduced the GO exfoliated solvent into graphene	Mono to few layer graphene suspension Size: up to μm	Versatile technique for large area production, can be stored in water	Hazardous chemical involved, only final product is stable in hydrophilic polymers
Thermal decomposition of SiC	High tempera-ture employed to evaporate Si form SiC wafer	Mono to few layer graphene films Size: up to cm	Epitaxial growth, low number of defects, control in thickness of film	Small scale producing, expensive, unscalable
CVD	Gaseous carbon source dehydrogenated into graphene on the metal surface at high temperature	Mono, bi and few layer graphene Size: cm to m	Scalable method, wide range of metals utilized as a substrate, large area up to few inch uniform film, various technique approaching monolayer film	Effort essential for the control of nucleation, High temperature, energy and time inefficient

1.5.1. Micromechanical Cleavage of Highly Ordered Pyrolytic Graphite (HOPG)

The technique of micromechanical exfoliation was used for decades before graphene was discovered. The exfoliation technique was the first way to obtain a few layers of graphene from graphite by mechanically or chemically breaking the interaction between neighboring graphene layers and peeling off graphene layers from graphite. Novoselov et al [8] made the first successful attempt to obtain a few layers of graphene by exfoliation. Lu et al. proposed that more extensive graphite surface rubbing against other flat surfaces may be a way to get several or even single graphite plate atomic layers [52]. This technique is now optimized to yield high-quality layers, with size limited by the single-crystal grains in the starting graphite, of the order of millimeters [17]. The original principle of this method is to use appropriate mechanical force by the use of adhesive tape to resolve the interaction of van der Waals between the interlayers of bulk material (graphite) without altering the in-plane covalent bonding.. Several exfoliations are carried out from bulk graphite and then into the adhesive tape itself in order to achieve a monolayer from a few layers graphene [8]. Finally, the adhesive tape is pressed over the desired substrate (SiO_2) and the graphene flakes are left on the substrate [**Fig. 1.4(a)**].

1.5.2. Liquid Phase Exfoliations

Graphene can also be exfoliated by liquid-phase exfoliation (LPE) techniques in liquid environments using ultrasound to extract individual layers [**Fig. 1.4(b)**]. In general, the LPE method includes three stages: (a) wet chemical dispersion of graphite in a solvent; (b) ultra-sonication induced exfoliation of bulk graphite into thin layer graphite flakes; (c) ultracentrifugation purification of graphite flakes [53]. The LPE technique is versatile and cost-effective and is compatible with composite material applications [54], conductive ink, and thin-film transistor ink-jet printing [55].

1.5.3. Epitaxial Growth on Silicon Carbide (SiC)

One of the most popular techniques is the epitaxial growth of graphene by thermal desorption of SiC substrate. Graphene growth on SiC is referred to as epitaxial growth and is achieved in an ultra-high vacuum by annealing the SiC substrate at high temperatures (> 1000 oC) [59, 60]. Despite the large (~25%), the lattice mismatch between graphene (2.46 Å) and SiC (3.073 Å), epitaxial graphene growth SiC is possible and carbon rearranges itself in the hexagonal lattice as Si evaporates from the SiC substrate [**Fig. 1.4 (c)**] [60, 61]. The number of graphene layers grown on the substrate depends on the temperature and the typical result is 1-3 graphene layers. Rollings et al [57] were successful to fabricate one thick graphene film atom. Further modifications were made at a lower temperature using Ni thin film-coated SiC substrate that assisted to obtain continuous large-area graphene layers [58]. In this technique, both C-terminated (000-1) and Si-terminated (0001) surfaces are used as templates [62, 63], but the lateral size of the graphene domains formed on the C-face is almost three times that of the Si-face [64, 65]. This method developed single to few-layer graphene on Si- to C-faces [60, 66-68]. The advantage of the graphene synthesized by this technique is that it is compatible with the SiC technology in power electronics that has been developed. The downside of this technique is that it controls the homogeneity of the layer thickness and thus prevents its potential use in applications [53, 69]. In addition, costly SiC wafer costs should be tackled for large-scale development by possible alternative means (using thin SiC grown on either Si or sapphire as a substrate) [70, 71].

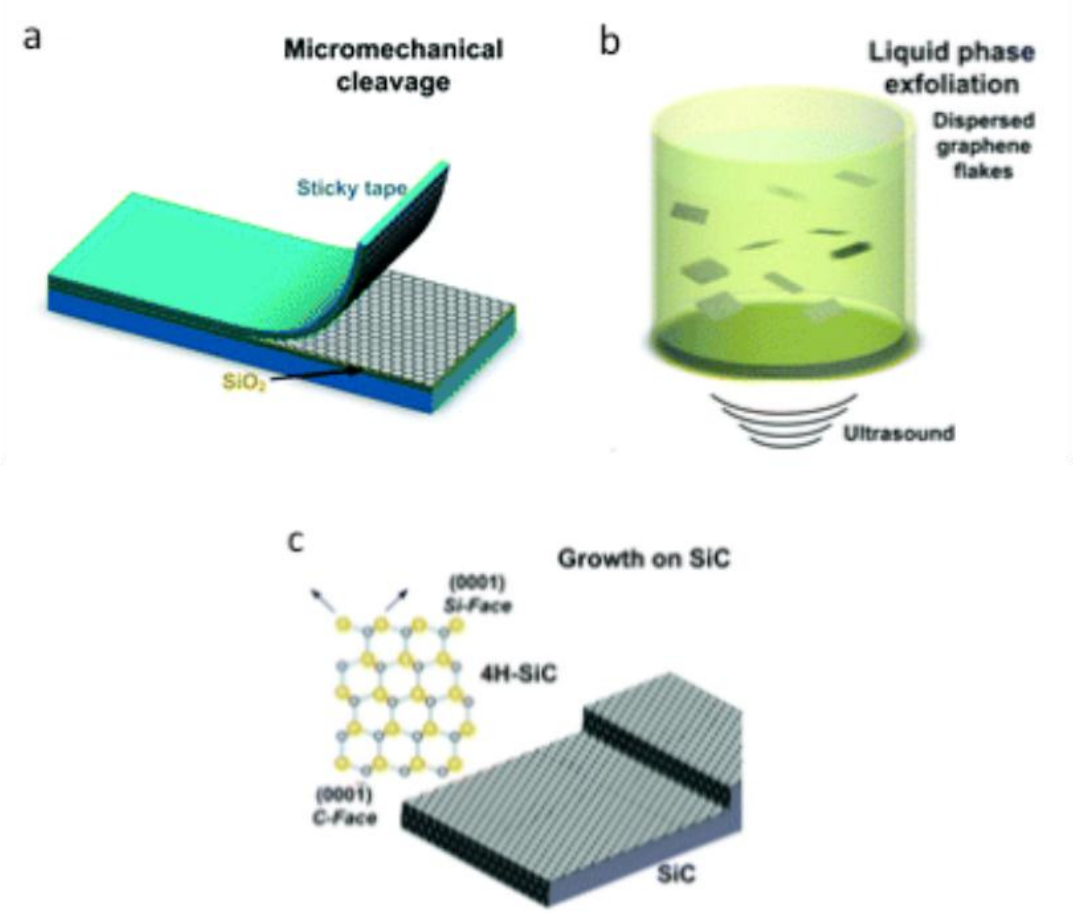

Figure 1.4: The schematic diagram illustrates the main graphene synthesis techniques. (a) A sticky tape on SiO_2 is used for micromechanical cleavage. (b) Liquid phase exfoliation showing bulk graphite dispersed into graphene flakes by ultra-sonication in solvents. (c) Epitaxial growth of graphene on the surface of the crystalline SiC. At elevated temperatures, Si atoms evaporate (arrows), leaving a carbon-rich surface that forms graphene sheets [53].

1.5.4. Reduction of Graphene Oxide (GO)

The basic concept of graphene-like sheet synthesis from graphite oxide (GO) is the exfoliation of graphene oxide into individual sheets of graphene oxide and the further chemical reduction of the individual sheets of graphene oxide obtained [72]. For the development of graphene in this route, the most common methods developed by Brodie [73], Hummer [74], and Staudenmeire [75] are used. GO is an insulating material (~1012 $\Omega\square^{-1}$) [76] with a photo-luminance (PL) characteristic [53] and is used for light-emitting devices [77] and bio-imaging applications [78]. However, the GO sheet can be reduced to a graphene sheet by using a reduction agent and washing process [79], which further restores electrical conductivity by healing the sp^2 network [72] as shown in **Fig. 1.5**. This method is a powerful and cost-effective technique for the processing of graphene on a large scale. During the reduction process, structural defects existed on the graphene sheet [80] and hazardous chemicals used during the process should be resolved in the future to make this process more beneficial.

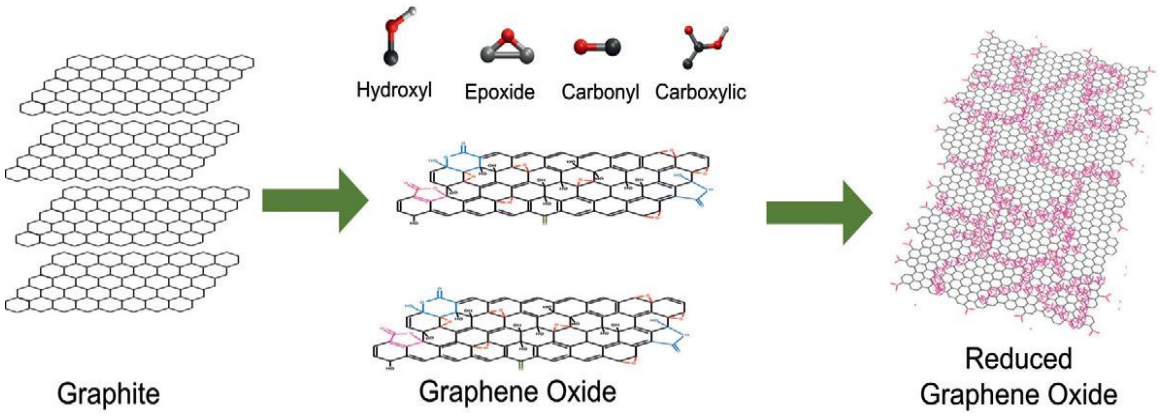

Figure 1.5: In the presence of strong acids, graphite can be oxidized into GO through different methods, and various functional groups have been added. Partial recovery of electronic property can be reached by following a reduction treatment [53].

1.5.5. Chemical Vapor Deposition

CVD is the researchers' first choice because it is the cheapest approach to make the desired layer, wide area, and high-quality graphene easier on different substrates. There are many CVD types, such as plasma-enhanced, low pressure, ultra-high pressure CVD (APCVD) atmospheric pressure, etc. The simplest type of CVD is APCVD, which illustrated with a schematic diagram in **Fig. 1.6(a)**. In the case of thermal CVD, most of the graphene synthesis has been done using Ni or Cu substrate and precursor gas mixture of H_2 and CH_4 or other hydrocarbons and Ar gas as the carrier gas. The quality and thickness of the graphene produced depend on the rate of cooling and heating, process temperature, gas ratio, thickness, and substrate crystallinity. Carbon precursors can be in gaseous forms such as methane, ethane, or other hydrocarbon containing gasses, liquid forms such as fatty oils, benzene, etc., and solid forms such as camphor, polymers, etc. These precursors provide the necessary hydrocarbons required for the formation of graphene. At high temperatures, hydrocarbons decompose and dissolve (depending on solubility) on the exposed surface of the catalytic substrate. The process of segregation-precipitation takes place on the substrate's surface to form graphene. Volatile by-products are also produced in the process, which is carried out with the carrier gas [**Fig. 1.6(b)**]. Using the thermal CVD process, Yu et al. showed three to four graphene layers grown on 500 nm thick polycrystalline Ni foils [84]. Similarly, high-quality, continuous graphene on Cu foil by thermal CVD has been demonstrated by X. Li et al. [81]. The PECVD technique is also useful for the synthesis of graphene, as this method decreases energy consumption and prevents the formation of amorphous carbon (a-C) [82].

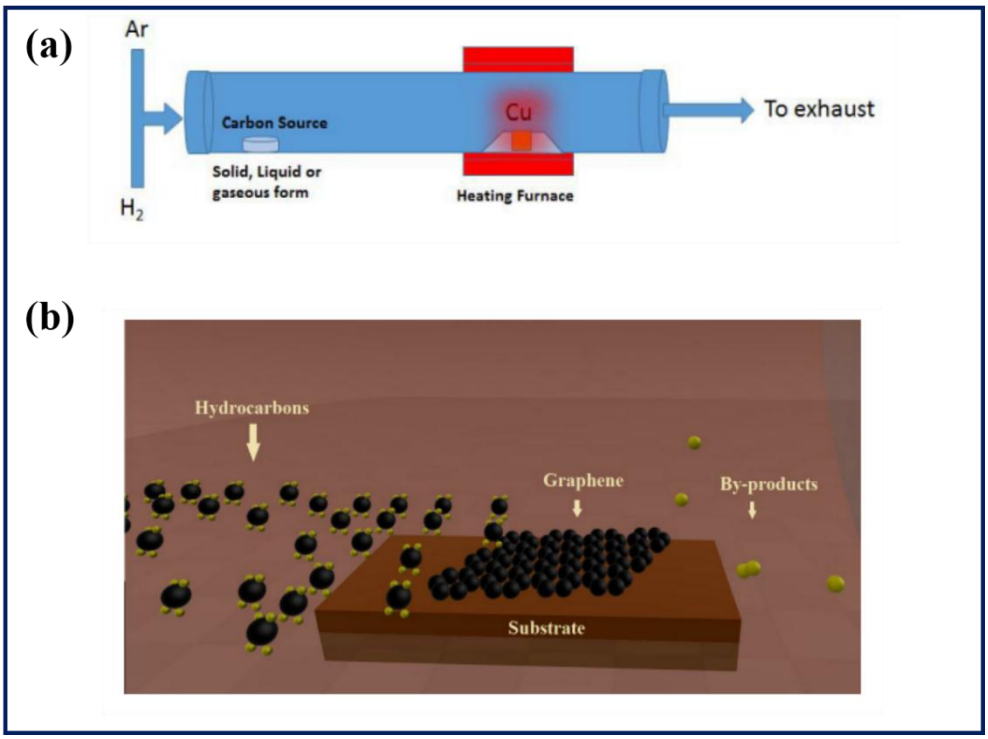

Figure 1.6: Schematic diagram of (a) CVD setup, (b) graphene formation process [83].

1.5.5. Solid Phase Reaction

The growth of graphene using the CVD method involves an additional transfer step for the manufacture of devices; this is not favorable for practical application. The synthesis of transfer-free graphene directly on the substrate is emerging and of significant importance in order to make the most of the promising physical and electrical properties of graphene and incorporate them into electronic devices. Recently, several studies have demonstrated graphene synthesis from a solid source rather than using conventional sources of hydrocarbon gas. Also, Graphene synthesis from the solid source depends on the metal-assisted high-temperature crystallization of a thin a-C film. In the metal-assisted crystallization process, a-C atoms diffuse through the metal layer at a high temperature to form graphene at the top of the metal surface [84-86]. However a surface-to-surface transfer process is also included in this method. Therefore, if the a-C solid-phase reaction and diffusion process can control to obtain graphene

under the metal layer, rather than graphene at the top of the metal surface, it will be very motivating [84-88]. For example, large area graphene and a controllable thickness can be synthesized at as low a temperature as 800^{o}C from solid carbon sources such as polymer films or small molecules deposited on a metal catalyst substrate [89]. The solid carbon source used in the studies was a spin-coated poly methyl methacrylate (PMMA) thin film (100 nm) and the metal catalyst substrate was a Cu film. At a temperature as low as 800^{o}C and as high as 1000^{o}C for 10 min, a single uniform layer of graphene was produced on the substrate with a reduction of gas flow (H_2/Ar) at low-temperature conditions [89].

1.6. Applications of Graphene

The remarkable properties of graphene described earlier open up their application in regions spreading across all science disciplines. Some novel applications of graphene were described in **Fig. 1.7**. Graphene-based field emission, gas sensors, and biosensors, transparent electrodes, and storage of lithium-ion have already been reported [37, 90-95]. Due to its high carrier mobility, graphene is considered a post-silicon material for electronic device applications [96]. Graphene-based devices with a data capacity of 0.2 T bits /cm^3, which is ten times the existing universal serial bus (USB) drives available, have been reported. This can help to increase the storage capacity of data in order to cope with the growing demand in the future [97-100]. Another potential application of graphene is in solar cell technology. Recent solar cells are suffering from the high cost of production. The cost and weight of homojunction carbon solar cells can decrease, but the performance of graphene-based solar cells needs to be improved. Doping graphene with nitrogen or boron to make it n-type or p-type respectively [101-103] can generate homojunction carbon solar cells.

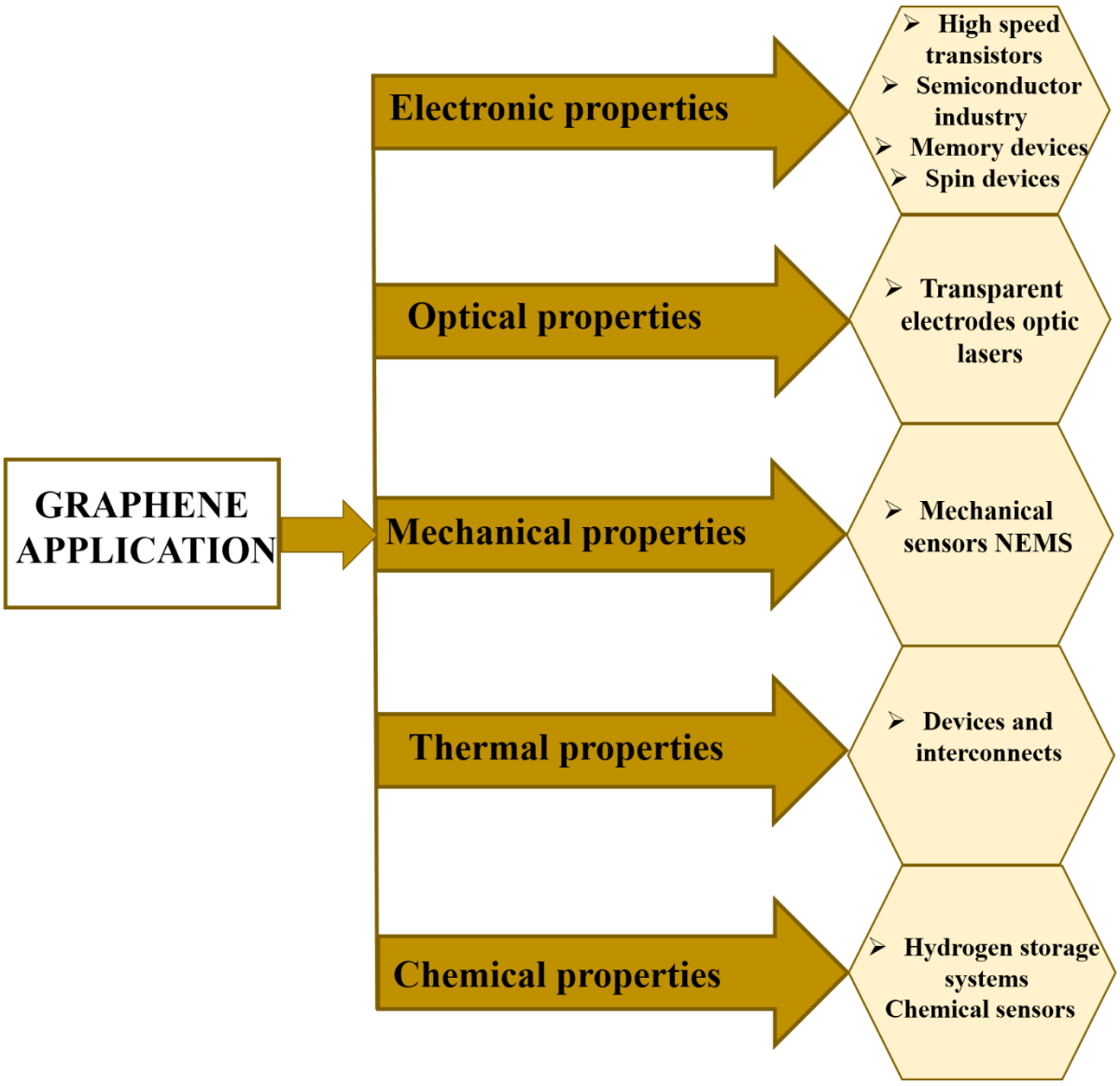

Figure 1.7: Some applications of graphene [99].

1.7. Challenge of Graphene Direct Growth at Low Temperature for Future Device Applications

Graphene is a 2D monolayer of sp^2-hybridized carbon atoms arranged in a honeycomb lattice, has attracted many interests due to its incomparable electronic properties, high thermal conductivity, and excellent mechanical properties [9, 105], which leads to a lot of potential applications such as being used as interconnections for nanoelectronics devices, energy storage devices, and next generation semi-conductor [106, 107].

It should be noted that most of the reported graphene syntheses include a high-temperature process. CVD, which is one of the most common graphene synthesis techniques, can synthesize high-quality graphene on metal catalyst foils only at high temperatures. Furthermore, CVD grown graphene film should be transferred onto the desired substrate for device applications. A metal substrate is chemically etched during the transfer of CVD-grown graphene, accompanied by repetitive and time-consuming cleaning cycles. However, low-temperature growth can be performed for a wider variety of practical applications. Therefore, many efforts have been devoted to the development of low-temperature graphene growth. In this respect, the main focus of material scientists and researchers was on two standard problems: i) direct growth and ii) graphene growth at low temperatures.

1.7.1. Direct Growth on Suitable Substrates

Direct graphene growth on insulating substrates is necessary in order to avoid the transfer process in CVD. So, two different growth methods, catalytic and non-catalytic growth, have been used directly on the flexible and rigid substrates to grow graphene monolayers [108-112]. Graphene synthesis has also been demonstrated by metal-assisted thin C film crystallization at an elevated temperature. C atoms diffuse through the metal layer at a high temperature in the metal-assisted crystallization process to form graphene at the top of the surface and at the interface between the catalyst metal and the substrate. For example, Nakajima et al. have demonstrated the formation of multilayer graphene (MLG) films directly on SiO_2 glass substrate using a-C at a temperature as low as 400°C by a simple sputtering technique using Co catalysts with high carbon solid solubility of Co [87]. So, the graphene growth at temperatures lower than 400^{o}C is still quite challenging.

1.7.2. Low-Temperature Growth.

For the well-known CVD growth, for instance, approaches using novel carbon sources, such as benzene, and using plasma enhancement have been proposed for the graphene synthesis [113-115]. In graphene research, one of the big issues is its low-temperature growth for a wider range of practical applications [116–118]. To achieve this, several novel catalysts have been proposed. For example, Kwak et al. have demonstrated the formation of graphene films directly on glass and plastic substrates using graphite powders at 25-160 °C via diffusion-assisted synthesis (DAS) method, where graphite powders were converted into graphene film through the diffusion of carbon along the Ni grain boundaries under quite high mechanical pressure (<1MPa) [120]. Xiong et al. [120] used magnetron sputtering to explore the growth mechanism of graphene from a solid carbon source through a nickel catalyst layer. They demonstrated a solid-state reaction between nickel and diffusing carbon forming a metastable nickel carbide compound at temperatures as low as 400^{o}C.

Recently, Lu et al. have synthesized graphene at 350°C, by vacuum annealing of a thin film of Ni-C-Ni sandwiched structure on a SiO_2/Si substrate [121]. In my group also, they have demonstrated the graphene formation on SiO_2 substrates by vacuum annealing at 150 and 250^{o}C for stacked a-C and catalyst films of low melting point, such as indium (In) and tin (Sn), respectively [24, 122] Recently, Asaka et al. have demonstrated the spontaneous local graphitization at RT for an a-C film deposited onto NaCl substrates with a pre-deposition of Ni NPs [123]. So, the use of NPs must be promising for the low-temperature graphitization (LTG) in the solid phase reaction. In this thesis, I dealt with the spontaneous graphitization at RT by simple one-step syntheses of Ni and Co-C films for the first time, leading to an additional strategy to achieve lower temperature graphene growth using metallic NPs catalyst which is lead to low melting point (MP) and high solubility. The MP of a crystal is well known to

strongly depend on its size, decreasing with decreasing crystal size. The solubility of carbon in NPs generally tends to increase with decreasing NP size, because a large fraction of the C atoms would be expected to be close to the surface, and the surface-to-volume ratio increases as the NP size decreases [124-128]. Atomic diffusion on metal surfaces for NPs is generally predicted to be much faster than for the bulk [129, 130]. So, the low-temperature graphene formation would be due to the decreased MP of the small size of NPs and increasing the solubility. The relationship between the particle size, melting point, and solubility is shown in **Fig. 1.8** [124, 131].

In this thesis, I also fabricated Li-C NCs for easy and safe handling based on the detailed observation using TEM for the first time. During the in-situ TEM observation of Li-C NC, the movement of Li atoms will induce the graphitization of a-C. This will be also the new strategy for the low temperature graphitization. So, Li-C NC may be promising as the catalyst for the LTG during the in-situ TEM observation. Recently, carbon matrix encapsulated metal/metal oxides, such as NiO, $NiCo_2O_4$, Fe_2O_3, Fe_3O_4, MnO_2, CuO, ZnO, Ge, and Sn/SnO_2, forming carbon-metal composites have been reported to display high specific capacity and excellent cycling performance as anode materials of the Li ion batteries (LIBs) [132-144]. Use of three-dimensional structures such as wires, fibers and tubes as current collectors has demonstrated a drastic reduction of Li dendrite formation [145, 146]. So, Li-C NC will be attract for the anode material of LIBs.

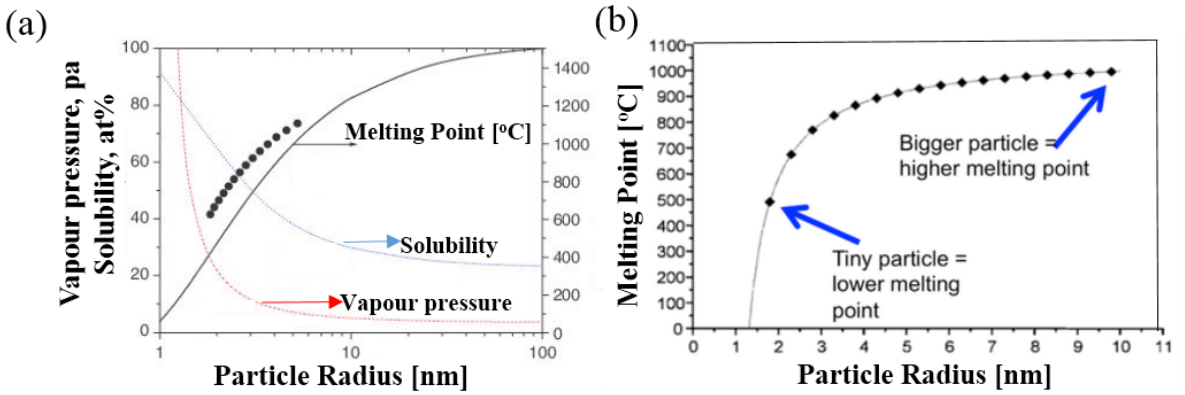

Figure 1.8: Relation between particle size, melting point, solubility, and vapour pressure of (a) iron (b) gold NPs [124, 131].

1.8. Motivations and Purposes of the Thesis

As described in the previous sections, the transfer-free graphene growth at lower temperatures has remained the key challenge in graphene research for practical applications. The previous work in my laboratory showed the low melting point metal, such as Sn and In, is promising for the low-temperature graphene growth [24, 122]. So, one of the key factors to achieve the goal must be the low melting point of the catalyst. Of course, Sn and In fulfil this prerequisite. Another approach to realize the low melting point is the use of NP form. If this strategy is successful, even the well-known catalyst of high melting point for the graphene growth, such as Ni whose melting point is 1455 °C, will act as the catalyst for the low temperature graphene growth. In fact, HR-TEM observation by Asaka et al. demonstrated the graphitic structure around Ni NPs for a-C films deposited onto NaCl substrates pre-coated with Ni NPs [123]. So, the next steps are the elucidation of (i) how to simplify the sample preparation process and (ii) what about other catalyst metals.

This dissertation was prepared to answer those questions. First, I launched the systematic investigation on the LTG for a-C films containing Ni NPs, which were prepared by a simple one-step magnetron sputtering method. Also, I dealt with the dependence of deposition

temperature and Ni content on the graphitization. Second, I tackled the synthesis of spontaneous graphitization at RT by simple one-step syntheses of Co-C films for the first time, in order to confirm the above-described strategy to achieve the ultra-low temperature graphene growth. Finally, based on the findings attained for Ni and Co NPs, I challenged the fabrication of novel Li-embedded nanocarbon (NC) composites using an ion beam setup, which can be easily extended to deposit Li-C NC films on any arbitrary substrates. For this Li-C NC, the movement of Li atoms during the charge-discharge process is expected to induce the graphitization of a-C. This will be also the new strategy for low-temperature graphitization. Of course, the proposed Li-C NC will be a candidate of the anode material for LIBs of next generation.

1.9. References

[1] M. Reibold, P. Paufler, A. A. Levin, W. Kochmann, N. Pätzke, and D. C. Meyer, Nature 2006, **444**, 286.

[2] E. Fitzer, A. Gkogkidis, M. Heine, HTHP, 1984, **16**, 363.

[3] I. Freestone, N. Meeks, M. Sax, and C. Higgitt, Gold Bull., 2007, **40**, 270.

[4] H. W. Kroto, J. R. Heath, C. O'brien, R. F. Curl, and R. E. Smalley, Nature, 1985, **318**, 162.

[5] F. Benissad, P. Gadelle, M. Coulon, and L. Bonnetain, Carbon 1988, **26**, 61.

[6] S. Iijima, Nature London, 1991, **354**, 56.

[7] W.A. de Heer, A. Chatelain, D. Ugarte, Science, 1995, **270**, 1179.

[8] K. S. Novoselov A. K. Geim, S. V. Morozov, D. Jiang, Y. Zhang, S. V. Dubonos, V. Grigorieva, and A. A. Firsov, Science, 2004, **306**, 666.

[9] A. K.Geim, K. S. Novoselov, Nat. Mater., 2007, **6**, 183.

[10] H. S. Sim, S. P. Lau, L. K. Ang, G. F. You, M. Tanemura, K. Yamaguchi, M. Zamri, Appl. Phys. Lett., 2008, **93**, 023131.

[11] Z. L. Wang, R. P. Gao, W. A. de Heer, and P. Poncharal, Appl. phys. Lett., 2002, **80**, 856.

[12] N. de Jonge, Y. Lamy, K. Schoots, T. H. Oosterkamp, Nature, 2002, **420**, 393.

[13] R. C. Smith, D. C. Cox, and S. R. P. Silva, Appl. Phys. Lett., 2005, **87**, 103112.

[14] H. S. Sim, S. P. Lau, L. K. Ang, G. F. You, M. Tanemura, K. Yamaguchi, and M. Zamri, Appl. Phys. Lett., 2008, **93**, 023131.

[15] M. Zamri, P. Ghosh, Z. P. Wang, M. Kawagishi, A. Hayashi, Y. Hayashi, and M. Tanemura, J. Vac. Sci. Technol. , 2010, **28**, C2C9.

[16] M. Z. M. Yusop, P. Ghosh, Y. Yaakob, G. Kalita, M. Sasase, Y. Hayashi, and M. Tanemura, ACS Nano, 2012, **6**, 9567.

[17] K. Geim, Science, 2009, **324**, 1530.

[18] H. C. Neto, F. Guinea, N. M. R. Peres, K. S. Novoselov, and A. K. Geim, Rev. Mod. Phys, 2009, **81**, 109.

[19] k. Barth and W. Marx, Tech. Rep., 2008, **118**. 1640.

[20] H. P. Boehm, R. Setton, E. Stumpp, J. Appl. Chem., 1994, **66**, 1893.

[21] M. Khan, M. N. Tahir, S. F. Adil, H. U. Khan, M. R. H. Siddiqui, A. A. Al-warthan, W. Tremel, J. Mater. Chem. A, 2015, **3**, 18753.

[22] J. B. Wu, H. A. Becerril, Z. Bao, et al., Appl. Phy. Lett., 2008, **92**, 263302.

[23] Y. Manawi, Ihsanullah, A. Samara, T. Al-Ansari, and M. Atieh, Mater., 2018, **11**, 822.

[24] M. I. Araby, M. S. Rosmi, R. Vishwakarma, S. Sharma, Y. Wakamatsu, K. Takahashi, G. Kalita, M. Kitazawa, and M. Tanemura, RSC Adv., , 2017, **7**, 47353.

[25] L., Gao, G.-X., Ni, B. Liu, A. H., Castro Neto, K. P., Loh. Nature, 2014, **505**, 190.

[26] P. R.Wallace, Phy. Rev.,1947, **71**, 622.

[27] G. S. Painter, D. E. Ellis, Phy. Rev., 1970, **1**, 4747.

[28] J. W. McClure, Phy., Rev., 1957, **108**, 612.

[29] K. S. Novoselov, A. K. Geim, S. V. Morozov, D. Jiang, M. I. Katsnelson, I. V. Grigorieva, S. V. Dubonos, A. A. Firsov, Nature, 2005, **438**, 197.

[30] X. Du, I. Skachko, A. Barker, E. Y. Andrei, Nat. nanotechnol., 2008, **3**, 491.

[31] J. C. Meyer, A. K. Geim, M. I. Katsnelson, K. S. Novoselov, T. J. Booth, S. Roth, Nature, 2007, **446**, 60.

[32] S. V. Morozov, K. S. Novoselov, M. I. Katsnelson, F. Schedin, D. C. Elias, J. A. Jaszczak, and A. K. Geim, Phy.Rev. Lett., 2008, **100**, 016602.

[33] A. S. Mayorov, R. V. Gorbatchev, S. V. Morozov, L. Britnell, R. Jalil, L. A. Ponomarenko, P. Blake, K. S. Novoselov, K. Watanabe, T.Taniguchi, and A. K. Geim, Nano Lett., 2011, **11**, 2396.

[34] J. H. Chen, C. Jang, S. Xiao, M. Ishigami, and M. S. Fuhrer, Nat. Nanotechnol., 2008, **3**, 206.

[35] R. R. Nair, P. Blake, A. N. Grigorenko, K. S. Novoselov, T. J. Booth, T. Stauber, N. M. R. Peres, and A. K. Geim, Science, 2008, **320**, 1308.

[36] K. S. Kim, Y. Zhao, H. Jang, S. Y. Lee, J. M. Kim, K. S. Kim, J. H. Ahn, P. Kim, J. Y. Choi, and B. H. Hong, Nature, 2009, **457**, 706.

[37] S. Bae, H. Kim, Y. Lee, X. Xu, J. S. Park, Y. Zheng, J. Balakrishnan, T. Lei, H. R. Kim, Y. I. Song, Y.J. Kim, K. S. Kim, B. Ozyilmaz, J. H. Ahn, B. H. Hong, and S. Iijima, Nat. Nanotechnol., 2010, **5**, 574.

[38] X. Wang, L. Zhi, and K. Müllen, Nano Lett., 2008, **8**, 323.

[39] F. Xia, T. Mueller, Y. m. Lin, A. Valdes-Garcia, and P. Avouris, Nat. Nanotechnol., 2009, **4**, 839.

[40] C. Lee, X. Wei, J. W. Kysar, and J. Hone, Science, 2008, **321**, 395.

[41] C. L. P. Pavithra, B. V. Sarada, V. Rajulapati Koteswararao, T. N. ABD Rao, and G. A. Sundararajan, Sci. Rep, 2014, **4**, 4049.

[42] Q. Wang, C. Wang, M. Zhang, M. Jian, and Y. Zhang, Nano Lett., 2016, **16**, 6695.

[43] C. Y. Ho, R. W. Powell, P. E. Liley, J. Phys. and Chem. Ref. Data, 2009, **1**, 279.

[44] D. L. Nika, S. Ghosh, E. P. Pokatilov, A. A. Balandin, Appl. Phys. Lett. 2009, **94,** 203103.

[45] A. A. Balandin, S. Ghosh, W. Bao, I. Calizo, D. Teweldebrhan, F. Miao, C. N. Lau, Nano Lett., 2008, **8**, 902.

[46] J.-W.Jiang, J.-S.Wang, and B. Li Phys. Rev., 2009, **79**, 205418.

[47] D. C. Elias, R. R. Nair, T. M. G. Mohiuddin, S. V. Morozov, P. Blake, M. P. Halsall, A. C. Ferrari, D. W. Boukhvalov, M. I. Katsnelson, A. K. Geim, and K. S. Novoselov, Science, 2009, **323**, 610.

[48] J. S. Bunch, S. S. Verbridge, J. S. Alden, A. M. Van der Zande, J. M. Parpia, H. G. Craighhead, and P. L. McEuen, Nano Lett., 2008, **8**, 2458.

[49] D. Prasai, J. C. Tuberquia, R. R. Harl, G. K. Jennings, and K. I. Bolotin, ACS Nano, 2012, **6**, 1102.

[50] X. Wang, X. Li, L. Zhang, Y. Yoon, P. K. Weber, H. Wang, J. Guo, and H. Dai, Science, 2009, **324**, 768.

[51] K. P.Sharma, Synthesis and characterization of graphene and hexagonal BN crystals on Cu by chemical vapor deposition using solid precursors (Doctoral dissertation), 2018.

[52] X. Lu, M. Yu, H. Huang, R. S. Ruoff, Nanotechnol., 1999, **10**, 269.

[53] F. Bonaccorso, A. Lombardo, T. Hasan, Z. Sun, L. Colombo, A. C. Ferrari, Mater. Today 2012, **15**, 564.

[54] M. Lotya, Y. Hernandez, P. J. King, R. J. Smith, V. Nicolosi, L. S. Karlsson, M. Blighe, S. De, Z. Wang, I. T. Mcgovern, V. Alzari, D. N. Scognamillo, S. G. S. Duesberg, J. N. Coleman, J. Am. Chem. Soc. 2009, **131**, 3611.

[55] F. Torrisi, T. Torrisi, W. Hasan, Z. Wu, A. Sun, T. Lombardo, G.-W. Kulmala, S. Hsieh, F. Jung, P. Bonaccorso, P. J. Paul, D. Chu, A. C. Ferrari, ACS Nano, 2012, **6**, 2992.

[56] Z. Wu, W. Ren, L. Gao, B. Liu, C. Jiang, and H.Cheng, Carbon 2009, **47**, 493.

[57] E. Rollings, G. H. Gweon, S. Y. Zhou, B.S. Mun, J. L. McChesney, B.S. Hussain, A.V. Fedorov, P.N. First, P.N. First, W. A. de Heer, A. Lanzar, Phys. and Chem. Solids, 2006, **67**, 2172.

[58] S. Amini, J. Garay, G. Liu, A. A. Balandin, R. J. Abbaschian, Appl. Phys., 2010, **108**, 094321.

[59] X. Li, Y. W. Zhu, W. Cai, M. Borysiak, B. Han, D. Chen, R. D. Piner, L. Colombo, R. S. Ruoff, Nano Lett., 2009, **9**, 4359.

[60] K. V. Emtsev, A. Bostwick, K. Horn, J. Jobst, G. L. Kellogg, L. Ley, J. L. McChesney, T. Ohta, S. A. Reshanov, J. Röhrl, E. Rotenberg, A. K. Schmid, D. Waldmann, H. B. Weber, T. Seyller, Nat. Mater. 2009, **8**, 203.

[61] K. V. Emtsev, F. Speck, T. Seyller, L. J. Ley, D. Riley, Phys. Rev. B, 2008, **77**, 155303.

[62] I. Forbeaux, J. M. Themlin, A. Charrier, F. Thibaudau, J. M. Debever, Appl. Surf. Sci. 2000, **162**, 406.

[63] A. Charrier, A. Coati, T. Argunova, F. Thibaudau, Y. Garreau, R. Pinchaux, I. Forbeaux, J. M. Debever, M. Sauvage-Simkin, , J. M. J. Themlin, Appl. Phys. 2002, **92**, 2479.

[64] J. Hass, J. E. Millán-Otoya, P. N. First, E. H. Conrad, Phys. Rev. 2008, **78**, 205424.

[65] J. Hass, R. Feng, T. Li, X. Li, Z. Zong, W. A. De Heer, P. N. First, E. H. Conrad, C. A. Jeffrey, C. Berger, Appl. Phys. Lett. 2006, **89**, 143106.

[66] S. Shivaraman, R. A. Barton, X. Yu, J. Alden, L. Herman, M. Chandrashekhar, J. Park, P. L. McEuen, J. M. Parpia, H. G. Craighead, M. G. Spencher, Nano Lett. 2009, **9**, 3100.

[67] Cai, T. Jia, Z. Yan, B. Yu, D. Wu, X. Appl. Phys. Lett. 2015, **106**, 013106.

[68] W. A. de Heer, C. Berger, M. Ruan, M. Sprinkle, X.Li, Y. Hu, B. Zhang, J. Hankinson, E. Conrad, Proc. Natl. Acad. Sci. 2011, **108**, 16900.

[69] H. Huang, W. Chen, S. Chen, A. T. S. Wee, ACS Nano 2008, **2**, 2513.

[70] T. J. Mcardle, J. O. Chu, Y. Zhu, Z. Liu, M. Krishnan, C. M. Breslin, C. Dimitrakopoulos, R. Wisnieff, A. Grill, Appl. Phys. Lett. 2011, **98**, 2012.

[71] C. Coletti, K. V. Emtsev, A. A. Zakharov, T. Ouisse, D. Chaussende, U. Starke, Appl. Phys. Lett. 2011, **99**, 2012.

[72] S. Stankovich, R. D. Piner, S. T. Nguyen, R. S. Ruoff, Carbon 2006, **44**, 3342–3347.

[73] B. C. Brodie Ann. Chim. Phys., 1860, **59**, 466.

[74] W. Hummers, R. J. Offeman Am. Chem. Soc., 1958, **80**, 1339.

[75] L. Staudenmaier Dtsch. Chem. Ges, 1898, **31**, 1481.

[76] A. B. Héctor, M. Jie, L. Zunfeng, M. Randall, B. Stoltenberg Zhenan, C. Yongsheng, ACS Nano 2008, **2**, 463.

[77] P. Y. Matyba, H. amaguchi, G. Eda, M. Chhowalla, L. Edman, N. D. Robinson, ACS Nano, 2010, **4**, 637.

[78] X. Sun, Z. Liu, K. Welsher, J. T. Robinson, A. Goodwin, S. Zaric, H. Dai, Nano Res. 2008, **1**, 203.

[79] C. K. Chua, M. Pumera, Chem. Soc. Rev., 2014, **43**, 291.

[80] S. Pei, H. M. Cheng, Carbon, 2012, **50**, 3210.

[81] X. Li, W. Cai, J. An, S. Kim, J. Nah, D. Yang, R. Piner, A. Velamakanni, I. Jung, E. Tutuc, S. K. Banerjee, L. Colombo, R. S. Ruoff, Science, 2009, **324**, 1312.

[82] J. J. Wang, M. Y. Zhu, R. A. Outlaw, X. Zhao, D. M. Manos, B. C. Holloway, V. P. Mammana, Appl. Phys. Lett., 2004, **85**, 1265.

[83] R. R. Vishwakarma, Controllable doping and low temperature growth of graphene on insulating substrates: Towards graphene applications in next generation electronics (Doctoral dissertation), 2017.

[84] R. Hirano, K. Matsubara, G.Kalita, Y.Hayashia, M. Tanemura, Nanoscale, 2012, 4, 7791.

[85] A. Ismach, C. Druzgalski, S. Penwell, A. Schwartzberg, M. Zheng, A. Javey, J. Bokor, Y. Zhang, Nano Lett., 2010, **10**, 1542.

[86] Y.Nakajima, H.Murata, N. Saitoh, N. Yoshizawa, T. Suemasu, K.Toko, ACS Omega, 2019, **4**, 667.

[87] M. Zheng, K. Takei, B. Hsia, H. Fang, X. Zhang, N. Ferralis, H. Ko, Y. L. Chueh, Y. Zhang, R. Maboudian , A. Javey, Appl. Phys. Lett., 2010, **96**, 063110.

[88] M. S. Uddin, H. Ichikawa, S. Sano and K. Ueno, Jpn J Appl Phys., 2016, **55**, 06JH02.

[89] Z. Sun, Z. Yan, J. Yao, E. Beitler, Y. Zhu, and J. M. Tour, Nat.lett., 2010, **468**,549.

[90] Z.-S. Wu, S. Pei, W. Ren, D. Tang, L. Gao, B. Liu, F. Li, C. Liu, H.-M. Cheng, N. Chiu, T. Huang, H. Lai, Adv. Mater., 2013, **21**, 1756.

[91] F. Schedin, A. K. Geim, S. V. Morozov, E. W. Hill, P. Blake, M. I. Katsnelson, K.S. Novoselov, Nat. Mater., 2007, 6, 652.

[92] R. Raccichini, A. Varzi, S. Passerini, B. Scrosati, Nat. Mater., 2015, **14**, 271.

[93] J. D. Fowler, M. J. Allen, V. C. Tung, Y. Yang, R. B. Kaner, B. H. Weiller, ACS Nano., 2009, **3**,301.

[94] G. Eda, H. Emrah Unalan, N. Rupesinghe, G.A.J. Amaratunga, M. Chhowalla, Appl. Phys. Lett., 2008, **93**, 233502.

[95] S. Alwarappan, A. Erdem, C. Liu, C.-Z. Li, J. Phys. Chem. C. 2009, **113**, 8853–8857.

[96] W. Choi, I. Lahiri, R. Seelaboyina, Y.S. Kan, Crit. Rev. Solid State Mater. Sci., 2010, **35**, 52.

[97] X.D. Zhuang, Y. Chen, G. Liu, P.P. Li, C.X. Zhu, E.T. Kang, K.G. Neoh, B. Zhang, J.H. Zhu, Y.X. Li, Adv. Mater., 2010, **22**, 1731.

[98] W. Zhang, Q. Zhang, M.-Q. Zhao, L.T. Kuhn, Nanotechnol., 2013, **24**, 275301.

[99] G. Liang, S. Bala Kumar, M.B.A. Jalil, S.G. Tan, Appl. Phys. Lett., 2011, **99**, 97.

[100] X. Li, Q. Zhang, X. Chen, M. Gu, Sci. Rep., 2013, **3**, 2819.

[101] H. Wang, K. Sun, F. Tao, D. J. Stacchiola, Y. H. Hu, Angew. Chemie-Int. Ed., 2013, **52** 9210.

[102] X. Miao, S. Tongay, M.K. Petterson, K. Berke, A.G. Rinzler, B.R. Appleton, A.F. Hebard, Nano Lett., 2012, **12**, 6.

[103] J. Liu, Y. Xue, Y. Gao, D. Yu, M. Durstock, L. Dai, Adv. Mater., 2012, **24**, 2228.

[104] M.E. Ayhan, Synthesis of Graphene by Chemical Vapor Deposition and Solid Phase Reaction Process (Doctoral dissertation), 2014.

[105] J. Deng, R. Zheng, Y. Zhao, G. Cheng, ACS Nano., 2012, **6**, 3727.

[106] Y. Zhu, S. Murali, W. Cai, X. Li, J. W. Suk, J. R. Potts, R. S. Ruoff, Adv. Mater. 2010, **22**, 3906.

[107] M. J. Allen, V. C. Tung, R. B. Kaner, Chem. Rev. 2010, **110**, 132.

[108] M. H. Rummeli, A. Bachmatiuk, A. Scott, F. Borrnert, J. H. Warner, V. Hoffman, J.-H. Lin, G. Cuniberti, and B. Buchner ACS Nano., 2010, **4**, 4206.

[109] J. Chen, Y. Wen, Y. Guo, B. Wu, L. Huang, Y. Xue, D. Geng, D. Wang, G. Yu, and Y. Liu, J. Am, Chem. Soc., 2011, **133**, 17548.

[110] L. Zhang, Z. Shi, Y. Wang, R. Yang, D. Shi, and G. Zhang, Nano Res., 2011, **4**, 315-21.

[111] R. Steingrüber, M. Ferstl, and W. Pilz, Microelectron. Eng., 2001, **57**, 285.

[112] J.-H. Lee, M.-S. Kim, J.-Y. Lim, S.-H. Jung, S.-G. Kang, H.-J. Shin, J.-Y. Choi, S.-W. Hwang, and D. Whang, Appl. Phys. Lett., 2016, **109**, 053102.

[113] V. P. Pham, H.-S. Jang, D. Whang and J.-Y. Choi, Chem. Soc. Rev., 2017, **46**, 6276.

[114] R. Muñoz, L. Martínez, E. López-Elvira, C. Munuera, Y. Huttel and M. García-Hernández, Nanoscale, 2018, **10**, 12779.

[115] M. H. Rümmeli, A. Bachmatiuk, A. Scott, F. Börrnert, J. H. Warner, V. Hoffmann, J.-H. Lin, G. Cuniberti and B. Büchner, ACS Nano, 2011, **4**, 4206.

[116] M. Marchena, D. Janner, T. L. Chen, V. Finazzi and V. Pruneri, Opt. Mat. Express, 2016, **6**, 3324.

[117] J. I. Fujita, T. Hiyama, A. Hirukawa, T. Kondo, J. Nakamura, S. I. Ito, R. Araki, Y. Ito, M. Takeguchi and W. W. Pai, Sci. Rep., 2017, **7**, 12371.

[118] R. Addou, A. Dahal, P. Sutter and M. Batzill, Appl. Phys. Lett., 2012**, 100**, 21601.

[119] J. Kwak, J. H. Chu, J. K. Choi, S. D. Park, H. Go, S. Y. Kim, K. Park, S. D. Kim, Y. W. Kim, E. Yoon, S. Kodambaka and S. Y. Kwon, Nat. Commun., 2012, **3**, 645.

[120] W. Xiong, Y.S. Zhou, W.J. Hou, T. Guillemet, J.F. Silvain, Y. Gao, M. Lahaye, E. Lebraud, S. Xu, X.W. Wang, D.A. Cullen, K.L. More, L. Jiang, Y.F. Lu, RSC Adv. 2015, **5**, 99037.

[121] L. Lu, J. T. M. De Hosson and Y. Pei, Mater. Des., 2018, **144**, 245.

[122] R. Vishwakarma, M. S. Rosmi, K. Takahashi, Y. Wakamatsu, Y. Yaakob, M.I. Araby, G. Kalita, M. Kitazawa, M. Tanemura, Sci. Rep. 2017, **7**, 43756.

[123] K. Asaka, Y. Saito, Carbon., 2016,**103**, 352.

[124] A. G. Nasibulin, P. Queipo, S. D. Shandakov, D. P. Brown, H. Jiang, P. V. Pikhitsa, O. V. Tolochko and E. I. Kauppinen, J. Nanosci. Nanotechnol., 2006, **6**, 1233.

[125] S. Mclellan and C. Thomsen, Philos. Trans. R. Soc., A, 2004, **362**, 2271.

[126] R. B. Mclellan, Scr. Metall., 1969, **3**, 389.

[127] M. Diarra, A. Zappelli, H. Amara, F. Ducastelle and C. Bichara, Phys. Rev. Lett., 2012, **109**, 185501.

[128] L. Baraton, Z. He, C. S. Lee, J. L. Maurice, C. S. Cojocaru, A. F. Gourgues-Lorenzon, Y. H. Lee and D. Pribat, Nanotechnology, 2011, **22**, 85601.

[129] R. Anton, Carbon, 2009, **47**, 856.

[130] S. Helveg, C. L´opez-Cartes, J. Sehestad, P. L. Hansen, B. S. Clausen, J. R. Rostrup-Nielsen, J. R. Rostrup-nielsen, F. Abild-pedersen and J. K. Nørskov, Nature, 2004, **427**, 5.

[131] G. Schmid, B. Corain, J. Inorg. Chem., 2003, **17**, 3081.

[132] S. Yang, X. Feng, S. Ivanovici, K. Mullen, Angew. Chem. Int. Ed. 2010, **49**, 8408.

[133] S. Yang, G. Cui, S. Pang, Q.Cao, U. Kolb, X. Feng, J. Maier, K. Mullen, Chem. Sus. Chem., 2010, **3**, 236.

[134] L. Bin, Q. Tengfei, Y. Delai, W. Lianzhou, Z. Linjie, Nano Energy, 2016, **22**, 232-240.

[135] M. Y. Cheng, B. J. J. Hwang, Power Sources, 2010, **195**, 4977.

[136] Z. Fan, B. Wang, Y. Xi, X. Xu, M. Li, J. Li, G. Yang, Carbon, 2016, **99**, 633.

[137] M. Nagao, M. Otani, H. Tomita, S. Kanzaki, A. Yamada, R. Kanno, J. Power Sources, 2011, **196**, 4741.

[138] L. Zeng, C. Zheng, C. Deng, X. Ding, M. Wei, ACS Appl. Mater. Interfaces, 2013, **5**, 2182.

[139] F. Wu, R. Huang, D. Mu, X. Shen, B. Wu, J. Alloys Compd., 2014, **585**, 783.

[140] M. Yang, Q. Gao, Microporous Mesoporous Mater., 2011, **143**, 230.

[141] R. Guo, L. Zhao, W. Yue, Electrochim. Acta., 2014, **152**, 338.

[142] L. Shen, E. Uchaker, C. Yuan, P. Nie, M. Zhang, X. Zhang, G. Cao, ACS Appl. Mater. Interfaces, 2012, **4**, 2985.

[143] J. Ma, D. Xiang, Z. Li, Q. Li, X. Wang, L. Yin, Cryst. Eng. Comm., 2013, **15**, 6800.

[144] X. Xu, Z. Fan, X. Yu, S. Ding, D. Yu, X. W. Lou, Adv. Energy Mater., 2014, **4**, 1400902.

[145] C.-P. Yang, Y.-X. Yin, S.-F. Zhang, N.-W. Li, Y.-G. Guo, Nat. Commun., 2015, **6**, 8058.

[146] A. Zhang, X. Fang, C. Shen, Y. Liu, C. Zhou, Nano Res., 2016, **9**, 3428.

Chapter 2

2. Experimental Methods and Characterizations

2.0. Background

This chapter is devoted to the detailed explanation of the main experimental methods that used for the synthesis of metal incorporated CNFs and metal-carbon nanocomposite for the ultra-low temperature graphene growth with their characterization technique employed in this thesis. This chapter is divided into two main sections: (a) experimental methods included to details of magnetron sputtering technique and ion beam irradiation method. (c) brief introduction to the instruments utilized for the characterization of synthesized materials.

2.1. Experimental Methods

2.2.1. Magnetron Sputtering

A wide variety of techniques can be employed for the deposition of thin films, sputter deposition belongs to a physical vapor deposition (PVD) technique of the thin film deposited since the primary mode of film synthesis is physical [1]. The general sputtering technique can be used to deposit a large range of materials for example metals, semiconductors, insulators, etc. The sputtering technique has some advantages of a simple tool, easy control, large coating area, and solid adhesion. When a solid surface is bombarded with energetic ions, surface atoms of the solid are scattered backward caused by collisions between both the surface atoms and the energetic particles [2], as shown in **Fig. 2.1**.

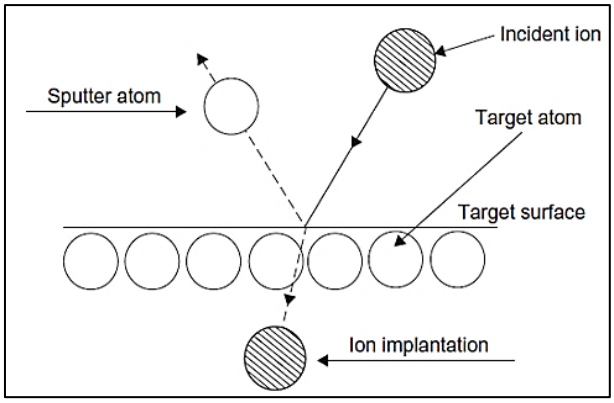

Figure 2.1: Physical sputtering processes [2].

There are many types of magnetron sputtering (see **Fig. 2.3**), such as direct current (DC) magnetron sputtering and radio frequency (RF) magnetron sputtering; each has a different working principle and application objects. The main advantage of RF magnetron sputtering over DC magnetron sputtering is that it does not require the target as an electrode be electrically conductive. Therefore, any material can be sputter-deposited theoretically using RF magnetron sputtering.

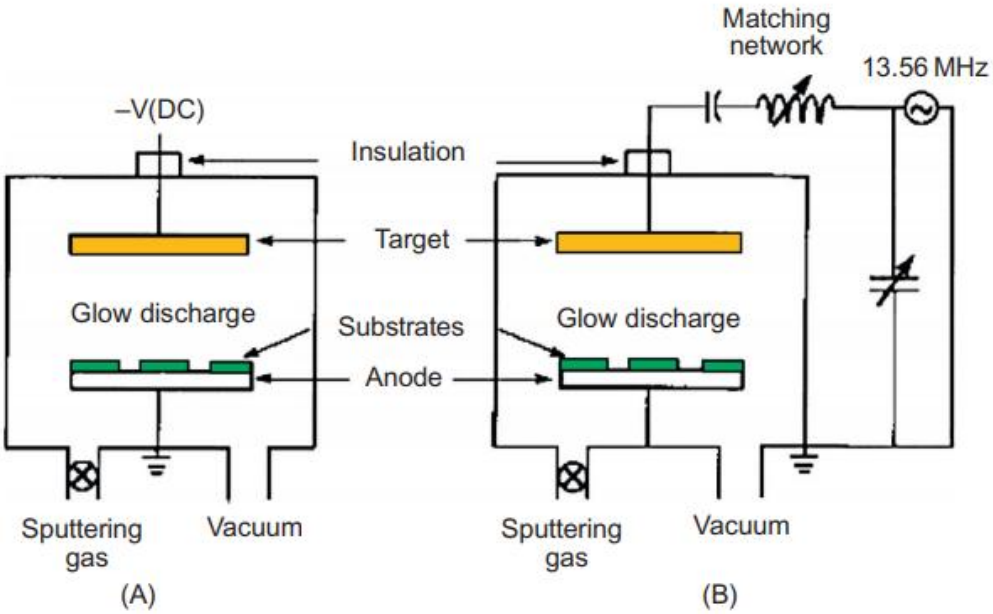

Figure 2.2: Schematic diagram of the principles of (A) direct current (DC) and (B) radio-frequency sputtering systems [3].

2.2.1.1. RF Magnetron Sputtering

The magnetron sputtering method developed in the 1970s achieves high speed, low temperature, and low damage. Adding a closed magnetic field parallel to the target surface in the bipolar sputtering, the secondary electron is bound to a specific area of the target surface to enhance the ionization efficiency by means of the orthogonal electromagnetic field formed on the surface of the target, increasing the ion density and energy, and finally realizing the high-rate sputtering. Magnetron sputtering is a dominant technique to grow thin films because a large quantity of thin films can be prepared at relatively high purity and low cost. This involves ejecting material from a "target" that is a source onto a "substrate" such as a silicon wafer [3], as displayed in **Fig. 2.3**. For a more detailed description of the principles behind the sputtering process and technical reviews of the current state of the art the reader is referred to references [4-8].

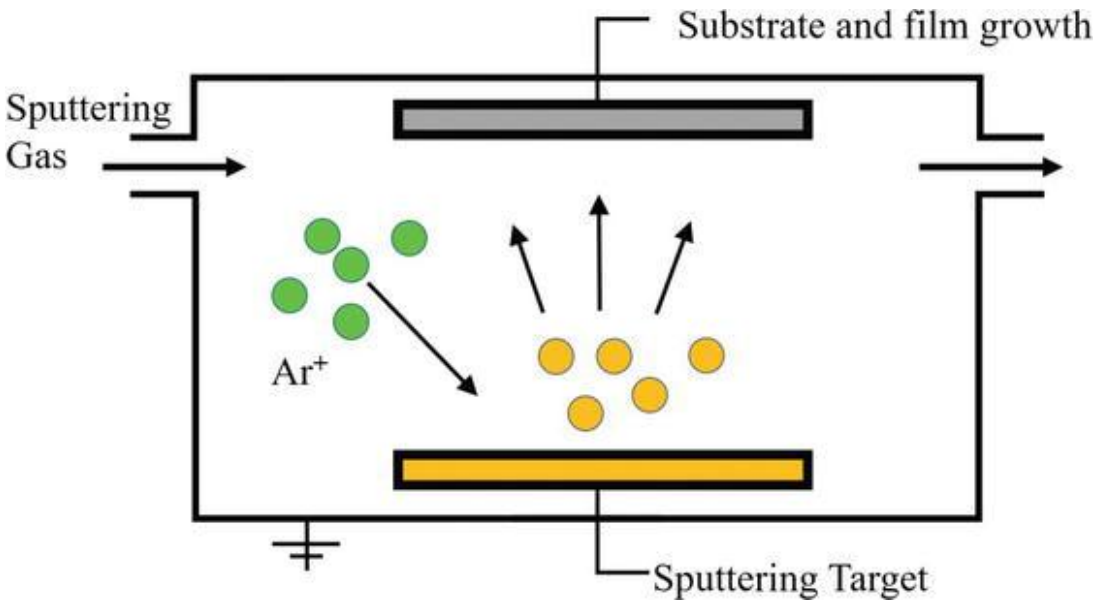

Figure 2.3: Schematic diagram of magnetron sputtering [3].

A simplified outline of the features of RF sputtering system is as described in the following:

- It is sputtering system of an insulator, metal, and a semiconducting material.
- Turbo molecular pump is used for main pumping.
- Multiple depositions are available by dia. 2 inch, 3 cathodes.
- Sputtering speed 30 nm/min (SiO_2) is available by magnetron sputtering.
- It has substrate heating system (350 degrees ^oC).
- RF power supply max 300W (0 – 300W variable)

The Ni-C and Co-C films central to both ***chapter 3*** and ***chapter 4*** have been deposited by Radiofrequency (RF) magnetron sputtering (SCOTT-C3 (VTR-151M/SRF), ULVAC KIKO Inc.) under base pressure of 3.0×10^{-4} Pa. Ar plasma was used for the film deposition. The RF power was set to 30 W.

2.2.2. Ion Beam Irradiation Method

The metal-carbon nanocomposite (metal-C NC, ***chapter 5***) were fabricated on the edge of a graphite foil by ion beam irradiation method at RT for this study. The substrate was sputtered with Ar^+ ions, using a Kaufman-type ion gun (Iontech. Inc. Ltd., model 3-1500-100FC, City, State Abbrev if USA or Canada, Country). The sample fabrication was carried out at an ion incident angle of 45° from the surface normal since an oblique Ar^+ ion bombardment is known to be suitable for the ion-induced CNF synthesis [9]. The ion beam employed was 6 cm in diameter. Ar^+ ions with energy of 700 or 1000 eV were continuously bombarded on the graphite foil and metal for 30 min at RT. The basal and working pressures for the fabrication of the ion-induced CNFs were 5×10^{-5} and 5×10^{-2} Pa, respectively. The system was evacuated by a rotary pump and a turbo molecular pump.

Commercially available graphite foils, PERMA-FOIL®, TOYO TANSO Co. Ltd. (Nishiyodogawa-ku, Osaka, Japan), with dimensions of 10 mm × 20 mm × 0.1 mm, were used as substrates. For the fabrication of the composite ion-induced CNFs, The graphite foil was placed vertically on a thick graphite sheet. Three to four shots of the metal (in this thesis; Li) were placed in front of the standing graphite foil plate as a metal supply source, and was co-sputtered with Ar^+ ions [**Fig. 2.4**]. After the ion irradiation, the SEM and TEM (JEM ARM 200F operated at 200 kV) were used for characterized the surface morphology and crystallinity of the samples.

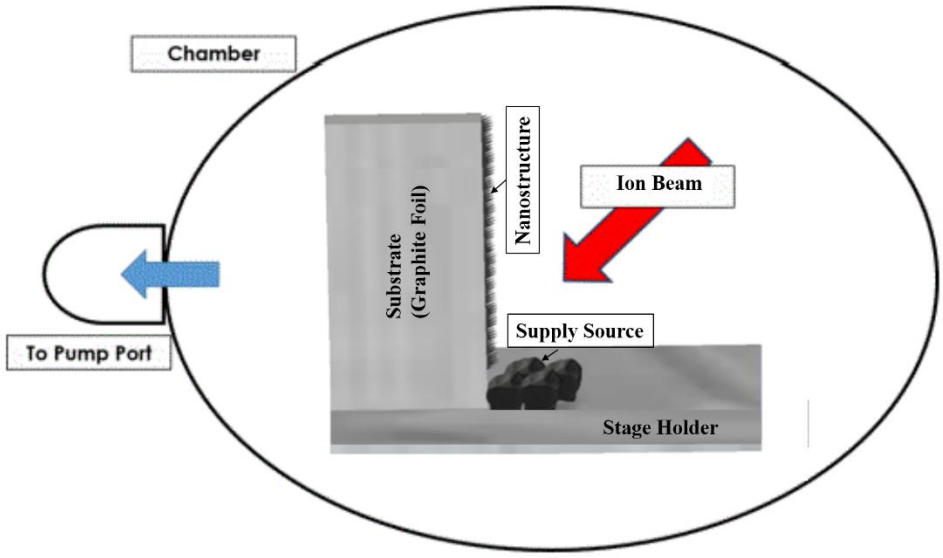

Figure 2.4: Schematic diagram of an ion beam irradiation deposition experimental setup.

2.2.2.1. Formation of Carbon Nanofibers (CNFs)

Further information of the detailed mechanism of the ion-induced CNF growth can be found elsewhere [10-12]. In brief, (i) the re-deposition of sputtered carbon atoms from the surface onto the sidewall of the conical protrusions, (ii) the surface diffusion during ion irradiation of the re-deposited carbon atoms towards the tip of the respective cones, and thus (iii) the formation of a CNF. A schematic diagram of the ion-induced CNF growth mechanism

is shown in **Fig. 2.5**. As mentioned above, in this CNF growth, different kinds of metals and semiconductors can be supplied to fabricate composite CNFs.

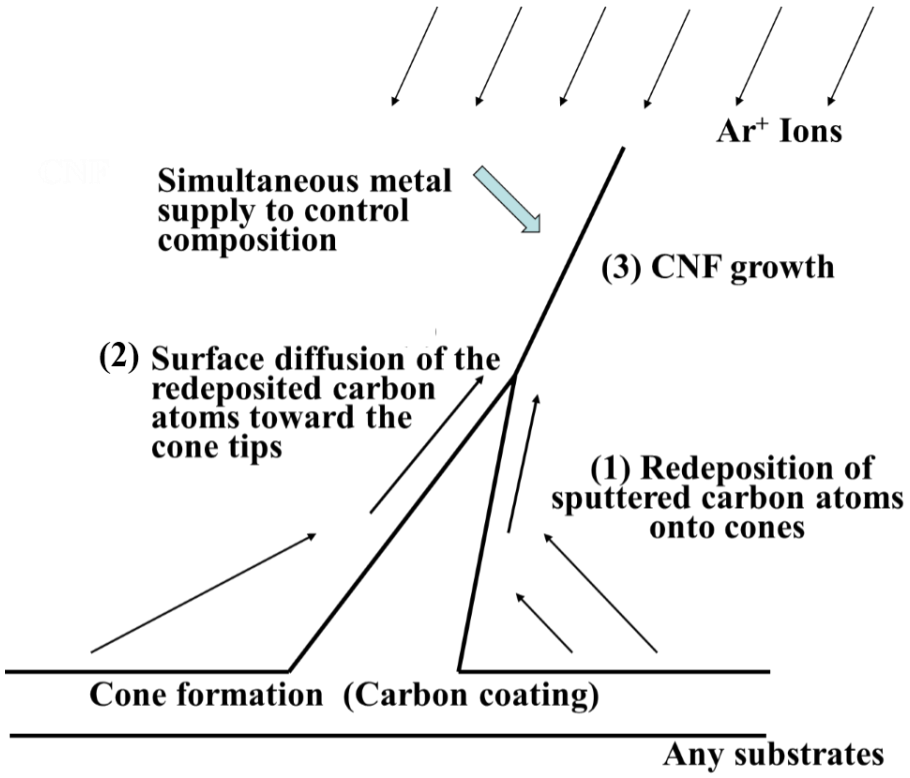

Figure 2.5: Schematic illustration of ion-induced CNF growth with a simultaneous metal supply at RT [12].

2.2. Characterizations

2.2.1. Scanning Electron Microscopy (SEM)

The SEM is a type of electron microscope which, by scanning the surface with an electron beam, provides details of surface information [13]. For the characterization of graphene morphology, SEM is routinely used. SEM can generate high-resolution images of specimens by using secondary scattered electrons obtained from the sample's surface on the SEM detector when a focused beam of high-energy electron beam occurring on the surface. **Fig. 2.6** displays the schematic diagram of SEM technology. The electron beam traces the sample in a raster pattern of this type of electron beam microscope. The SEM images provided in this thesis were

obtained using JEOL JSM-5600 operated in the accelerating voltage range of 2-20 keV. Low and high magnification images were recorded. For the CNFs case, images were taken up with a magnification scale of 20X to around 30.000X and spatial resolution of 50 to l00 nm.

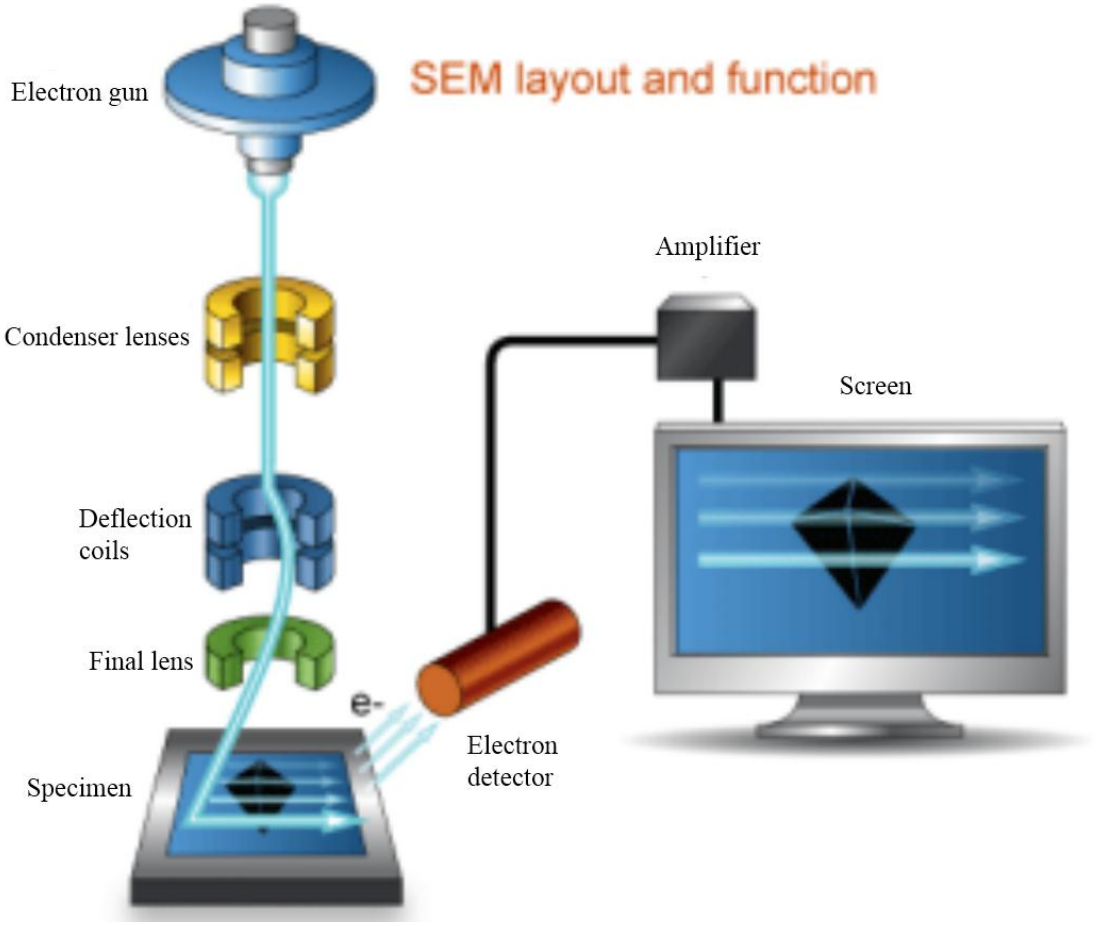

Figure 2.6: Schematic diagram of a scanning electron microscope [14].

2.2.2. Transmission Electron Microscopy (TEM)

2.2.2.1. Brief History

The TEM is a quite effective method for the study of the characteristics of very small samples in material science. TEM can be used to describe the morphology, crystal structure, and elemental details of membrane materials. According to its optical functions, a TEM can be split into three main components: (a) illumination component, (b) objective lens system component, and (c) magnification component [15]. In **Fig. 2.7**, a schematic diagram showing

imaging and diffraction modes which are the three parts of the TEM is shown. TEM generally consists of three stages of lensing, stages include the condenser lenses, the objective lenses, and the projector lenses. The first stage is the main beam forming condenser lenses, the second is the objective lenses that concentrate on the beam that passes through the sample, and the last stage is projector lenses that are used to extend the beam to the phosphor screen. TEM utilizes the electron in which the shape is applied by electromagnetic lenses, while the visible light formed by glass lenses is used in an optical microscope as a source. In addition, TEM requires a high vacuum environment, while the optical microscope requires only ambient pressure. **Table 2.1** summarizes the comparison between the optical microscope and TEM.

Table 2.1. Comparison between optical microscope and TEM construction [9].

	Optical Microscope	TEM
Illumination system	Visible light	Electron gun
Lenses	Glass lenses	Electromagnetic lenses
Surrounding	Atmosphere	High vacuum

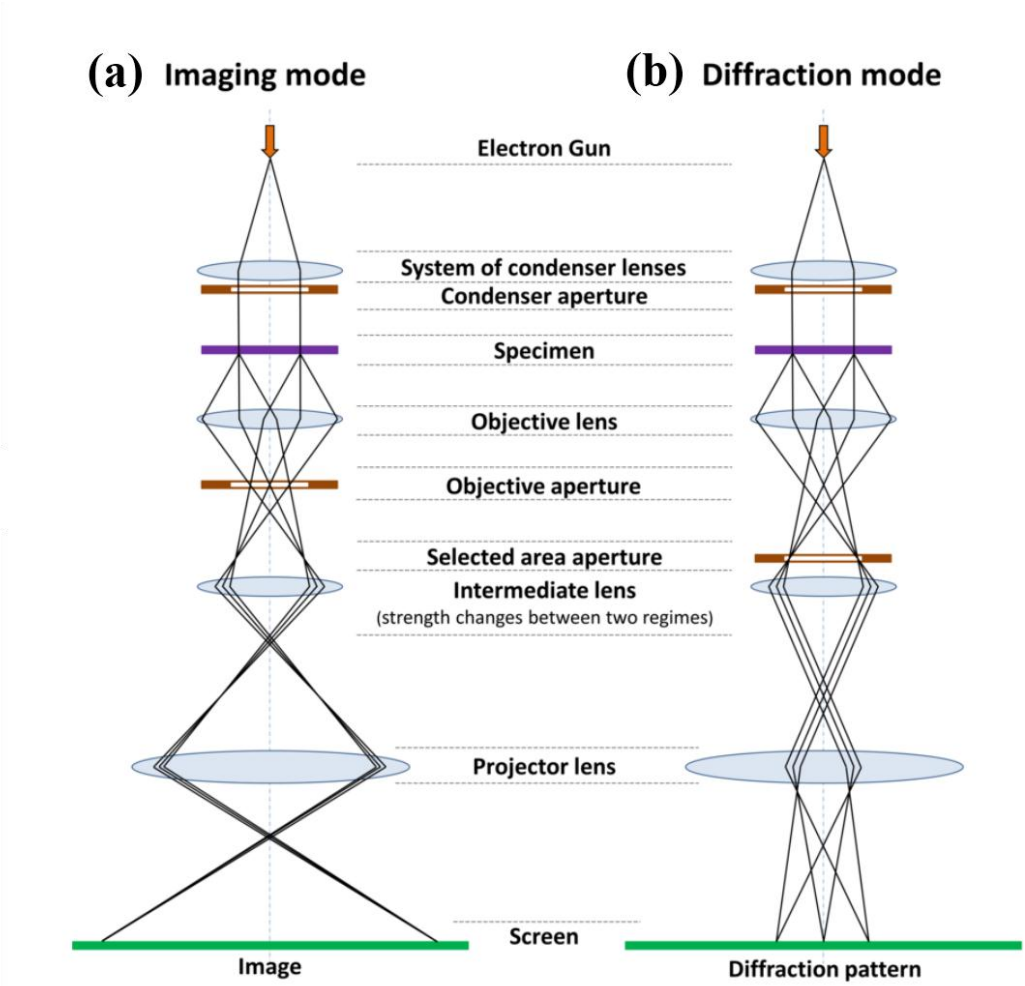

Figure 2.7: Two basic TEM imaging system operations: (a) imaging mode, and (b) diffraction mode [16].

Figure 2.8: TEM model: JEM-ARM200F (JEOL) used in the thesis [17].

2.2.2.2. Imaging and Diffraction Modes

Imaging and diffraction modes are the two basic TEM operating modes. **Fig. 2.7** illustrated these two basic modes. In both cases, the specimen is illuminated by the parallel beam generated by electron beam shaping with the system of condenser lenses and a condenser aperture. There are two groups of electrons after the sample interaction, which are unscattered and scattered electrons.

In the back focal plane (BFP) of objective lenses, where the diffraction spots are formed, an objective aperture can be inserted. A bright-field image (BF image) is obtained if the objective aperture with a central beam region is chosen (the rest of the signal is blocked). A dark-field image (DF image) is made if we select an area and exclude the central beam. Then, the selected signal is magnified and projected on a screen or on a camera with the help of an intermediate and projector lenses. Image of the sample is received.

In diffraction mode, in order to obtain a diffraction pattern from a local region, a selected area aperture is used to select a specimen area of interest. The area of the sample from which the diffraction pattern is obtained can be controlled depending on the aperture size. It is possible to use selected area electron diffraction (SAED) to identify crystal structures that are similar to X-ray diffraction. However, SAED has an advantage in carrying out analysis at an area as small as the nanoscale level. In a TEM, a thin crystalline sample is subjected to high-energy electron parallel beams. The diffraction mode enables an amorphous, polycrystalline, or single-crystal material to be revealed.

2.2.2.3. Lattice Image Observation

The interlayer spacing of lattice images can be determined by applying high-resolution TEM (HRTEM) observation, so it can be measured using the Gatan microscopy suite software. For example, **Fig. 2.9** displays the profile picture of the layer intensity, indicating an interlayer spacing of 0.345 nm for bilayer graphene [18].

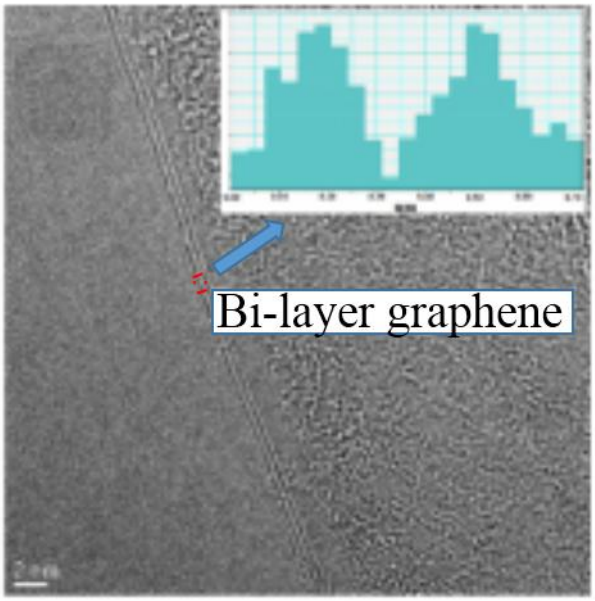

Figure 2.9: Example of interlayer spacing measurement [18].

2.2.2.4. Microanalysis in TEM

Not only high-resolution imaging but also the combination of these imaging techniques with the other generated signals to investigate the chemistry of the specimens is one of the key benefits of TEM investigations. A microanalysis is a study using the analytical TEM (ATEM) to analyze specimen chemistry. It should be noted that most modern TEMs operating at intermediate voltages of 200/300 keV are fitted with TEM ((S) TEM) scanning functions, energy dispersive X-ray spectroscopy (EDX), and complementary electron energy loss spectroscopy (EELS) techniques. In this thesis, EDX and EELS have been used in the experiments performed for the microanalysis.

2.2.2.4.1. Energy-Dispersive X-Ray Spectroscopy (EDX) Analysis

Energy-dispersive X-ray spectroscopy (also referred to as EDS, EDX, or EDXA) is a powerful analytical technique used for the identification and quantification of a sample's elemental composition. Because of the atom is ionized by the accelerated electrons within the TEM specimen, there is a possible transition within the atom's internal shells associated with the emission of a characteristic X-ray which has specific energy for that element. Special detectors are used to obtain the emitted X-ray photons and plots of X-ray counts versus X-ray energy. The elemental composition of a specimen can be quantified and estimated from the intensities of the peaks. Conventional X-ray detectors are semiconductor-based detectors such as lithium (Li) doped silicon (Si) that are shielded during collection by an ultra-thin window cooled by liquid nitrogen to reduce thermal noise.

2.2.2.4.2. Electron Energy Loss Spectroscopy (EELS)

EELS is an analytical technique focused on the inelastic dispersion in a thin specimen of fast electrons. EELS is an extremely effective characterization tool in the TEM, which provides spatially resolved data on elemental composition, chemical bonds, optical properties, and modes of vibration. In the last decade, this technique has seen significant success, largely due to the advancement of transformative instrumentation. Monochromatic electron sources and high-resolution spectrometers enhance the resolution of energy more than an order of magnitude, improve the analysis of the near-edge energy loss structure (ELNES), and enable the study of phonons and optical properties. When an electron beam is an incident into a specimen, a part of the electrons is inelastically scattered and loses a part of the energy. Analyzing the energy with the spectroscope attached under the electron microscope (EELS) can be determined elemental composition and atomic bonding state.

2.2.3. Raman Spectroscopy

Raman spectroscopy is a technique commonly used to obtain the structural and electronic characteristics of the sample by using monochromatic light source inelastic dispersion to shape the sample in a vibrational mode. Raman spectroscopy is a relatively simple, non-destructive, non-contacting, and quick measurement method for measuring the inelastic dispersion of light from the sample surface at ambient pressure and RT. Notably, This technique been has used to determine the number of graphene layers by probing the phonon spectrum of graphene [19, 20]. Raman spectra of graphene presented in this thesis were obtained by using NRS-3300 Raman spectrometer with a laser source of wavelength 532.8 nm at RT.

In graphic materials, three important peaks are observed [21–23]. The graphic peak about 1582 cm^{-1} (called the G band) is induced by sp^2 carbon atoms (E_{2g} phonon) in-plane vibration; the appearance of a G band in the Raman spectra suggests that sp^2 carbon networks are included in the sample. The signal intensity of the D band, located about 1350 cm^{-1} and due to the boundary phonons of the first-order region, strongly depends on the quantity of disorder in the graphic material [24] and is absent in defect-free graphene. The D band is triggered in the event of a network defect [25, 26]. The third peak about 2690 cm^{-1}, (called the 2D band) as an overtone of the D band, is induced by second-order zone boundary phonons that exhibit a strong frequency dependence on the excitation laser energy and is correlated with stacking orders. The 2D band was used to calculate the number of graphene layers of the considered graphene samples [26, 27]. The shift in position of individual peaks are strongly associated with the light source used for the detection of spectra as well as the layer numbers of graphene [28]. The intensity ratio I_{2D} /I_G of the 2D and G bands, respectively, is generally used to describe the number of layers in the synthesized graphene film. A high ratio indicates monolayer graphene and the lower the ratio, the more layers, with 1 being bilayer graphene and below 1 for

multilayer graphene. Also, for the determination of the number of layers of the graphene samples, the Full Width at Half-Maximum (FWHM) of 2D bands can be used. Monolayer graphene shows a very sharp, symmetric, and Lorentzian 2D band. The 2D band becomes broader, less symmetric, and decreases in strength with the increase in the number of layers: the FWHM rises. For monolayer, bilayer, and multilayer graphene, the FWHM of the 2D band would usually be 30, 50, and 80 cm^{-1}, respectively.

2.2.4. Optical Microscope

The optical microscope also referred to as a light microscope, is a type of microscope that generally uses visible light and a lens system to create magnified images of small objects as shown in **Fig. 2.10**. Optical microscopes are the oldest type of the microscope and were probably invented in the 17th century in their present compound form. The advantages of the optical microscope are direct imaging without the need for sample pre-treatment, the only true microscopy of color imaging, fast and adaptable to all types of sample systems, from gas to liquid and solid sample systems, in any shape or geometry, and simple to integrate with digital data storage and analysis camera systems. And it also has some disadvantages, low resolution, typically down to only sub-microns or a few hundreds of nanometers, mostly due to the limit of light diffraction. An optical microscope is found to be a straight-forwarded characterization tool for the identification of exfoliated graphene onto the SiO_2/Si substrate [29-31]. The optical transparency of graphene decrease with increasing layers numbers, resulting in distinguishable optical contrast on SiO_2/Si. An OM (VHX-500) with a Moticam 2000 2.0 Mpixel camera in reflectance mode has been employed to obtain the optical images. OM is used to examine the various samples easily, including substratum surface morphologies, grown material confirmation, graphene layer number identification on SiO_2, etc.

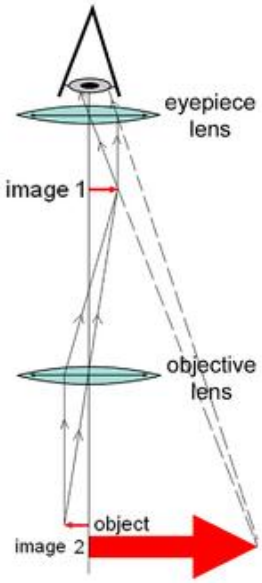

Figure 2.10: Diagram of basic microscope compounds [32].

2.2.5. X-Ray Photoelectron Spectroscopy (XPS)

XPS is a photoelectric-based surface-sensitive quantitative spectroscopic technique that can classify the elements that exist within or cover the surface of a material (elemental composition) as well as their chemical state and the overall electronic structure and density of the electronic states in the material. XPS is a powerful method of measurement since it not only indicates what components are present but also what other elements to which they are bound. XPS is measured the elemental composition of a sample surface by irradiating a substrate with monochromatic X-rays. The photo-emitted electrons from the sample surface (5-10 nm surface depth) are obtained and hence produced by the electron energy analyzer. Thus, binding energy spectra and photoelectron peak intensity spectra are generated from which the elemental composition, chemical state, and quantity of a detected element can be calculated. In this thesis, the chemical state analysis of foreign elements on grown materials (graphene) was acquired by XPS (a Kratos Analytical Axis UltraDLD UHV spectrometer) using a monochromatized Al Kα X-ray source (1486.6 eV).

2.2.6. X-Ray Diffraction (XRD) Analysis

XRD is a very essential experimental method that has long been used to tackle all issues related to solid crystal structure, including lattice constants, identification of single crystal orientation of unknown materials, and preferred polycrystal orientation [33]. The crystallographic structure was carried out by a Cu target fitted XRD system (Rigaku RINT 2100 diffractometer). The Ni-filtered Cu Kα radiation (λ=1.5408 Å) was used. The X-ray tube voltage and current were 40 kV and 30 mA, respectively. XRD's knowledge is concerned with the periodicity of a system. Each atom serves as a scattering point for waves in a periodic structure. These scattered waves can interfere constructively in order to create sharp intensity peaks. The requirements for constructive interference are defined by Bragg's law [33, 34], as given below in **Eq. 1** with an assumed simplified model in **Fig. 2.11**.

$$2d_{hkl}\sin\theta = n\lambda \quad (1)$$

where, n is a positive integer, λ is the wavelength of the incident wave, d is the distance between the periodic atoms and θ is the diffraction angle. As a function of the scattering angle 2θ, the measured intensity provides information on the spacing between the planes of atoms in the crystal structure, and also the atom sites inside the crystal structure.

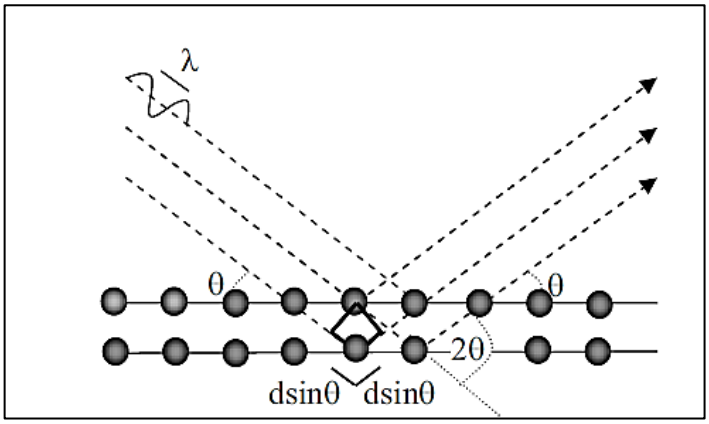

Figure 2.11: Diffraction as described in Bragg's Law in an atomic lattice [33].

2.3. References

[1] M. Ohring, Materials Science of Thin Films: Deposition and Structure 2nd Edition, Academic Press, London, UK, 2002, ISBN: 0-12-524975-6.

[2] Kiyotaka Wasa, Isaku Kanno, Hidetoshi Kotera Handbook of Sputter Deposition Technology, Second edition, William Andrew is an imprint of Elsevier, 2012.

[3] M. Ohring, S.P. Baker, Materials science of thin films: deposition and structure. San Diego, CA: Elsevier Science & Technology Books, 2016.

[4] B. Chapman. Glow Discharge Processes: Sputtering and Plasma Etching. Wiley, New York, 1980.

[5] K. Wasa, S. Hayakawa. Handbook of Sputter Deposition Technology: Principles, Technology, and Applications. William Andrew Publishing, 1992.

[6] K. Wasa, M. Kitabatake, H. Adachi. Thin Film Materials Technology: Sputtering of Compound Materials. Springer, 2004.

[7] R. Kukla. Surf. .Coat. Technol., 1997, **93**, 1

[8] M. Lieberman, A. Lichtenberg. Principles of Plasma Discharges and Materials Processing. Wiley Online Library, 2005.

[9] M. Tanemura, T. Okita, H. Yamauchi, S. Tanemura, and R. Morishima, Appl. Phys. Lett., 2004, **84**, 3831.

[10] M. Tanemura, H. Hatano, M. Kitazawa, J. Tanaka, T. Okita, S. P. Lau, H. Y. Yang, S. F. Yu, L. Huang, L. Miao, and S. Tanemura, Surf. Sci.., 2006, **600**, 3663.

[11] M. Tanemura, T. Okita, J. Tanaka, M. Kitazawa, K. Itoh, L. Miao, S. Tanemura, S. P. Lau, H. Yang, and L. Huang, IEEE Trans. Nanotechnol., 2006, **5**, 587.

[12] M. Tanemura and S. P. Lau: "Flexible Field Emitters: Carbon Nanofibers (Chapter 15)" in "Carbon Nanotube and Related Field Emitters: Fundamentals and Applications" Edited by Y. Saitoh, Wiley-VCH Verlag GmbH & Co. KGaA (Weinheim) 2010.

[13] P. E. J. Flewitt, R. K. Wild, Physical Methods for Materials. Characterization, IOP Publishing, Bristol, Chapter 6, 1994, 515.

[14] Australian Microscopy and Microanalysis Research Facility, "My Scope-training for advanced research" http://www.ammrf.org.au/myscope/sem/background/Accessed online on 3-5-2018.

[15] D. B. Williams and C. B Carter, Transmission Electron Microscopy, Part I: Basics, Springer Science, Second Edition, 2009, 3-22.

[16] http://mtrmika.Technion.ac.il/wp-content/uploads/2014/02/6_52_Double_Tilt_Heat_ Holder_Dsheet_FL5.pdf.

[17] http://www.beyondnano.it/?q=instruments-beyond-nano-center-catania 2020/10/16.

[18] M. Z. Yusop, G. Kalita, Y. Yaakob, C. Takahashi, and M. Tanemura, Appl. Phys. Lett., 2014, **104**, 093501.

[19] M. A. Pimenta, G. Dresselhaus, M. S. Dresselhaus, L. G. Cançado, A. Jorio, R. Saito, Phys. Chem. Chem. Phys., 2007, **9**, 1276.

[20] P. Klar, E. Lidorikis, A. Eckmann, I. A. Verzhbitskiy, A. C. Ferrari, C. Casiraghi, Phys. Rev. B, 2013, **87**, 205435.

[21] Ni Z. Wang, T. Yu, Z. Shen, H. Wang, Y. Wu, W. Chen, A. T. S. W. Wee, The J. Phys. Chem. C, 2008, **112**, 10637.

[22] D. Graf, F. Molitor, K. Ensslin, C. Stampfer, A. Jungen, C. Hierold, L. Wirtz, Nano Lett., 2007, **7**, 238.

[23] A. C. Ferrari, J. C. Meyer, V. Scardaci, C. Casiraghi, M. Lazzeri, F. Mauri, S. Piscanec, D. Jiang, K. S. Novoselov, S.Roth, A. K. Geim, Phys. Rev. Lett., 2006, **97**, 187401.

[24] A. Eckmann, A. Felten, A. Mishchenko, L. Britnell, R. Krupke, K. S. Novoselov, Nano Lett., 2012, **12**, 3925.

[25] F. Tuinstra, J. L. Koenig, the J. Chem. Phys., 1970, **53**, 1126.

[26] Y. Zhu, S. Murali, W. Cai, X. Li, J. W. Suk, J. R. Potts, R. S. Ruoff, Advan. Mater., 2010, **22**, 3906.

[27] Y. Hao, Y. Wang, L. Wang, Z. Ni, Z. Wang, R. Wang, C. K. Koo, Z. Shen, J. T. L. T. Thong, Small , 2010, **6**, 195.

[28] A. C. Ferrari, Solid State Commun., 2007, **143**, 47.

[29] A. K. Geim, I. V. Grigorieva, Nature 2014, **499**, 419.

[30] K. S. Novoselov, D. Jiang, F. Schedin, T. J. Booth, V. V. Khotkevich, S. V. Morozov, A. K. Geim, Proc. Natl. Acad. Sci. 2005, **102**, 10451.

[31] C. Lee, Q. Li, W. Kalb, X. Z. Liu, H. Berger, R. W. Carpick, J. Hone, Science, 2010, **328**, 76.

[32] https://en.wikipedia.org/wiki/Optical_microscope, 2020/10/20

[33] B. D. Cullity, "Elements of x-ray diffraction", Addison-Wesley publishing company Inc. 1978.

[34] W. Callister and D. Rethwisch, Fundamentals of Material Science and Engineering, Wiley, 4th edition, Chapter 3, 2013.

Chapter 3

3. Room Temperature Graphitization in Solid Phase Reaction Using Ni Nanoparticles

3.1. Introduction

As described in the previous chapter, up to now, all the reports, even the report by Asaka et al., showed no distinct 2D peak in the Raman spectra (evidence of graphitized layers) for the as-deposited films of the well-known catalyst Ni. For example, CVD temperature was reduced to 500^{o}C under ultra-high vacuum conditions by tuning the growth parameters for the carbon source of C_2H_4 [1]. Besides the CVD technique, Kwak et al. have demonstrated the formation of graphene films directly on glass and plastic substrates using graphite powders at 25-160°C via diffusion-assisted synthesis (DAS) method, where graphite powders were converted into graphene film through the diffusion of carbon along the Ni grain boundaries under quite high mechanical pressure (<1MPa) [2]. Xiong et al. [3] used magnetron sputtering to explore the growth mechanism of graphene from a solid carbon source through a nickel catalyst layer. They demonstrated a solid-state reaction between nickel and diffusing carbon forming a metastable nickel carbide compound at temperatures as low as 400^{o}C. Recently, Lu et al. have synthesized graphene at 350°C, by vacuum annealing of a thin film of Ni-C-Ni sandwiched structure on a SiO_2/Si substrate [4]. So, the graphene growth at temperatures lower than 350^{o}C is still challenging especially for Ni catalyst. Very recently, Asaka et al. have demonstrated the spontaneous local graphitization around Ni NPs even without heat treatment for amorphous carbon film deposited onto NaCl substrates with a pre-deposition of Ni NPs [5]. They observed the disordered graphitic structure around Ni NPs by HR-TEM. However, no trace of the 2D

peak was detected by Raman spectroscopy. Stimulated by this result, I launched the systematic investigation on the low-temperature graphitization for amorphous carbon films containing Ni NPs, which were prepared by a simple one-step magnetron sputtering method. If the metallic Ni NPs are used as the catalyst, does the graphitized form without any heat treatment? And I will deal with the temperature and Ni content dependences of graphitization. This is also a very interesting subject.

3.2. Experimental Method

Amorphous carbon films containing Ni NPs (referred to Ni-C films hereafter) were deposited onto commercially available microgrids (NS-M15, Okenshoji Inc.) for TEM and SiO_2 covered Si substrates (Ni-C/SiO_2/Si) by a magnetron sputtering system (SCOTT-C3 (VTR-151M/SRF), ULVAC KIKO Inc.). A microgrid is a well-known porous carbon film used to support a fine specimen like powders for TEM. For the Ni-C film deposition, a carbon (graphite) disk of a diameter 50 mm with an attachment of small Ni platelet (referred to a Ni-C target hereafter) was prepared. The thicknesses of the Ni-C film were 7 nm. In order to investigate the effect of the Ni concentration in the Ni-C film, different size of Ni platelets; 5×5 and 5×15 mm^2, were prepared for the attachment to the carbon disk. So, the area ratios of the Ni platelet to the carbon disk were 0.25:19.4 and 0.75:18.9, respectively. The background pressure of the chamber was 1.20×10^{-5} pa and high purity Ar (99.999%) was used as a sputtering gas at a power of 30 W for 5 minutes. In order to investigate the temperature dependence of the graphitization, the Ni-C films were deposited at RT and at 50 ^{o}C. After the deposition of Ni-C films, plan view Raman spectroscopy (NRS 3300 laser Raman spectrometer) with a laser excitation energy of 532.08 nm and TEM (JEM ARM 200F) operated at 200 kV were used for the characterization of the samples.

3.3. Results

3.3.1. Films prepared by a Ni-C target with a Ni platelet of 0.25 cm^2 (referred to 0.25-Ni-C film and 0.25-Ni-C target, respectively)

Fig. 3.1(a) shows a typical TEM image of a 0.25-Ni-C film deposited onto a microgrid at RT, disclosing that the Ni-C film was featured by the dispersion of NPs with weak black contrast. Some of the NPs are indicated by arrow-heads in **Fig. 3.1(a)**. The upper inset in **Fig. 3.1(a)** shows a fast Fourier transform (FFT) taken for a rectangular region in **Fig. 3.1(a)**. The FFT confirmed that the graphitization occurred at RT which is relatively intense ring pattern resulted from the graphite (002). **Fig. 3.1(b)** shows the size distribution of the NPs measured for **Fig. 3.1(a)**, revealing that the NPs ranged from ~0.7 to ~2.3 nm in size with an average size of about ~1.3 nm. Since the carbon film deposited by the C disk without any Ni platelet contained no NP with black contrast, the NPs should be the Ni NPs. In fact, a small amount of Ni was detected by compositional energy dispersive x-ray spectroscopy (EDS) analysis for the 0.25-Ni-C film [**Fig. 3.1(c)**]. It should be stressed that the ordered lattice fringes of short-range are observable at many regions by a careful inspection of **Fig. 3.1(a)**. As shown in a lower inset in **Fig. 3.1(a)**, the spacing of the ordered fringes was measured to be ~0.36 nm which corresponds to the lattice spacing of graphite (002). Asaka et al.[14] observed such a spontaneous local graphitization at around the Ni NPs for amorphous C film deposited on a NaCl substrate with the pre-deposition of Ni NPs. Different from their observation, the spontaneous local graphitization was observed also in the region between Ni NPs [see upper inset in **Fig. 3.1(a)**].

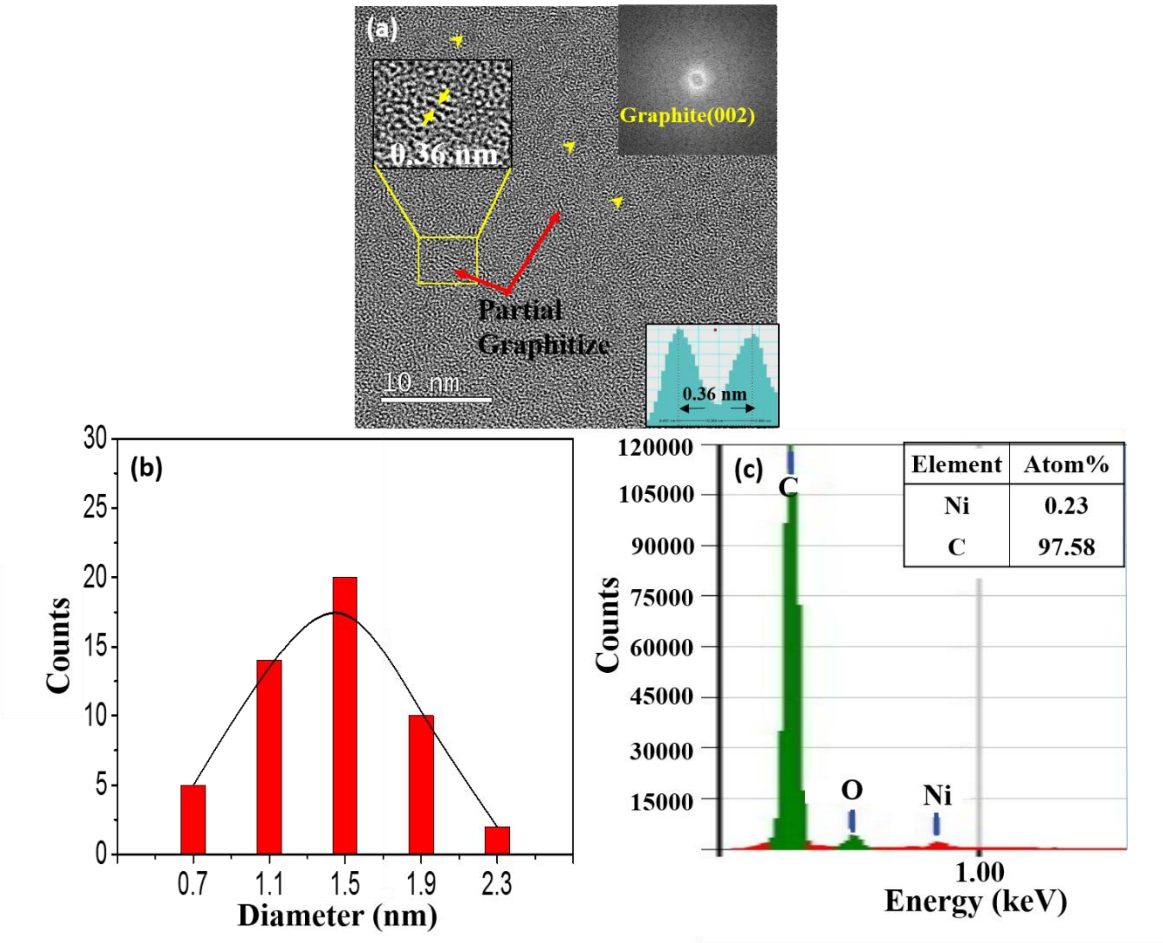

Figure 3.1: (a) TEM image of a 0.25-Ni-C film deposited on a microgrid at RT. The upper insets show an FFT image and an enlarged image of the rectangular region. The lower inset represents an intensity line profile of the arrow indicated lattice region in the upper inset, indicating the interlayer spacing of 0.36 nm. (b) Size distribution of Ni NPs in (a). (c) EDS corresponding to (a).

Fig. 3.2 shows a typical TEM image of a 0.25-Ni-C film deposited at 50^{o}C. The number density of Ni NPs of the film decreased. Obviously, the lattice fringes with the spacing of 0.34 nm corresponding graphite (002), which are ordered in short ranges, were more prominent compared with the film prepared at RT [**Fig. 3.1(a)**]. The FFT images of small rectangular regions of Ni-C film deposited at 50^{o}C in **Fig. 3.2(a)** [A-D] are shown in **Fig. 3.2(b)**, revealing Deby ring corresponding to graphite (002). Compared with the RT deposited film [**Fig. 3.1(c)**],

the size distribution of the particles was slightly shifted to the larger size, 1.3 to 2.7 nm with an average size of 2 nm, as shown in **Fig. 3.2(c)**. The effect of the deposition temperature on both the graphitization and the size of Ni NPs will be discussed later.

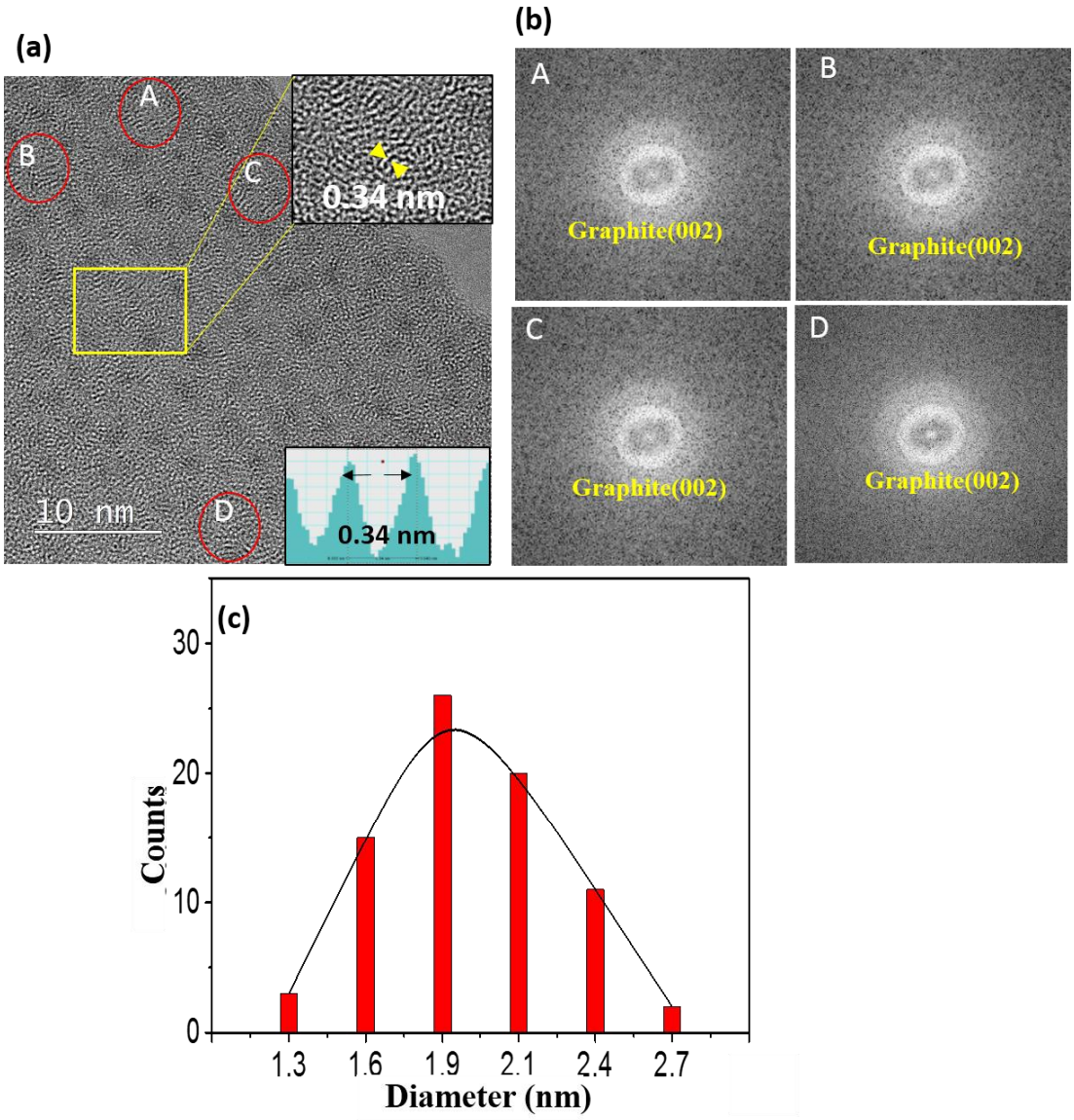

Figure 3.2: (a) TEM image of a 0.25-Ni-C film deposited at 50°C. The upper inset in (a) shows an enlarged image of the rectangular region. The lower inset in (a) shows an intensity line profile of the lattice image of the arrow indicated lattice region in the upper inset, indicating the interlayer spacing of 0.34 nm corresponding to graphite (002). (b) FFT images of the Ni-C film taken in small selected region [A-D] in (a). (b) Size distribution of Ni NPs in (a).

In order to confirm the graphene formation (graphitization) more quantitatively, those 0.25-N-C films were also analyzed by Raman spectroscopy. Because the Raman analysis was difficult for the microgrid samples, the films simultaneously deposited onto SiO_2 covered Si substrates were used for the Raman analyses. **Fig. 3.3** shows their optical images and typical Raman spectra. At a glance of the optical images for the RT and 50^{o}C deposited films shown in **Fig. 3.3(a, b)**, respectively, there were agglomerated-like regions in greenish color (referred as region A hereafter) on the flat surfaces in blue color (referred as region B hereafter) for both samples. The agglomerated-like regions were more prominent for the 50^{o}C deposited film. **Fig. 3.3(c, d)** shows their Raman spectra, respectively. As seen in **Fig. 3.3(c)**, the region A shows intense G and 2D peaks centered at 1583 and 2694 cm^{-1}, respectively, with an intense D peak at 1349 cm^{-1}, while region B was characterized by very weak D and G peaks at 1352 and 1581 cm^{-1}, respectively, without 2D peak.

It was also the case for the 50^{o}C sample as shown in **Fig. 3.3(d)**. The region A was characterized by G and 2D peaks centered at 1581 and 2693 cm^{-1}, respectively, with a less intense D peak at 1355 cm^{-1}, whereas the region B was characterized by the small bumps corresponding to D and G peaks at 1367 and 1595 cm^{-1}, respectively, without 2D peak. The intensity ratio of D and G peaks (I_D/I_G) of the films deposited at RT and 50^{o}C were measured to be ~0.7 and 0.5 for the region A, respectively. In their research, Lu, et al. demonstrated that the I_D/I_G was ~1.8 for graphene formed at 350°C using a Ni-C-Ni thin film sandwiched structure on an isolator substrate (SiO_2/Si) [4]. The Raman spectrum for the RT and 50^{o}C deposited films of the region B was different from that of the amorphous C film [6] and quite similar in shape and intensity to that of the C film deposited on the NaCl substrate with the pre-

deposition of Ni NPs by Asaka et al. [3, 7]. So, the presented work realized higher graphitization at lower temperature.

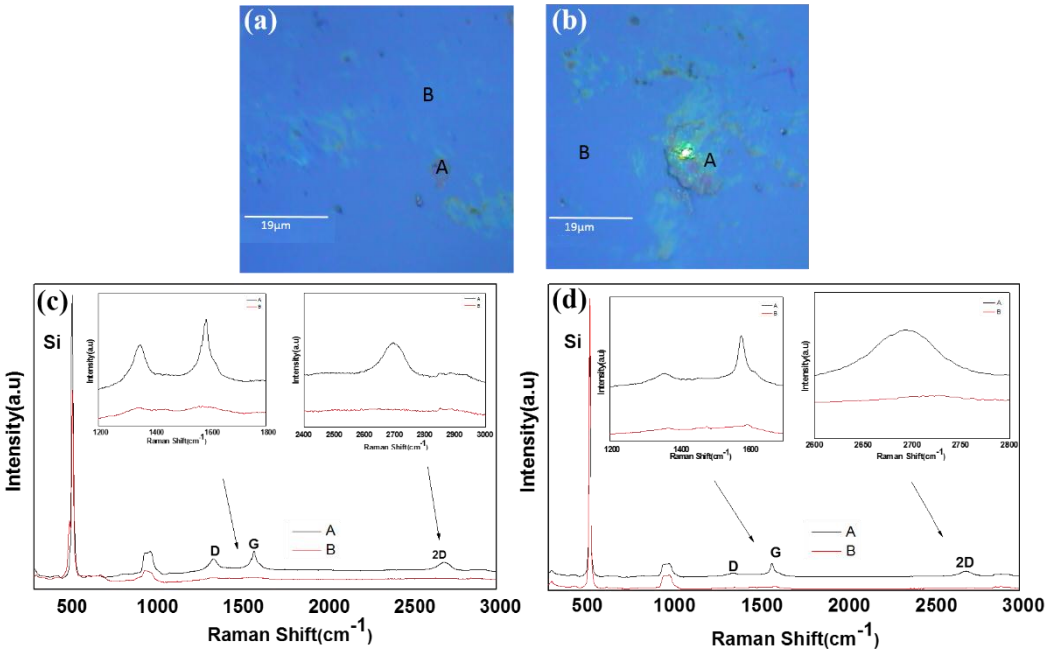

Figure 3.3: (a) and (b) optical images of the 0.25-Ni-C films deposited at RT and 50^{o}C, respectively. (c) and (d) Raman spectra of the 0.25-Ni-C films deposited at RT and 50^{o}C, respectively. The insets in (c) and (d) are the magnified spectra around D, G and 2D peaks.

3.3.2. Films prepared by a Ni-C target with a Ni platelet of 0.75cm^2 (referred to 0.75-Ni-C film and 0.75-Ni-C target, respectively)

In order to check the effect of Ni/C ratio, films with higher Ni concentration were prepared using a 0.75-Ni-C target. **Fig. 3.4(a)** shows a typical TEM image of a 0.75-Ni-C film deposited onto a microgrid at RT. Similar to the 0.25-Ni-C film case (shown in **Fig. 3.1**), the 0.75-Ni-C film was featured by the distributed NPs. For this 0.75-Ni-C film also, short range graphitization, whose interlayer spacing was measured to be 0.36 nm, was observed at many regions as exemplified by the inset in **Fig. 3.4(a)**. Different from the 0.25-Ni-C film case, however, NPs were dispersed more densely in the 0.75-Ni-C film and were featured by broad Deby rings corresponding to Ni (200), Ni (220) planes as shown in **Fig. 3.4(b)**. **Fig. 3.4(c)**

shows a size distribution of Ni NPs measured in **Fig. 3.4(a)**, revealing that the average size of the Ni NPs was about ~2.1 nm, which was larger than that of 0.25-Ni-C film deposited at RT. The relatively larger Ni NPs would be responsible for the observed Deby rings. The larger amount of Ni was also confirmed by EDS spectrum as shown in **Fig. 3.4(d)**. In **Fig. 3.4(d)**, distinct oxygen peak was also detected. This point will be discussed in detail later combined with the graphitization mechanism.

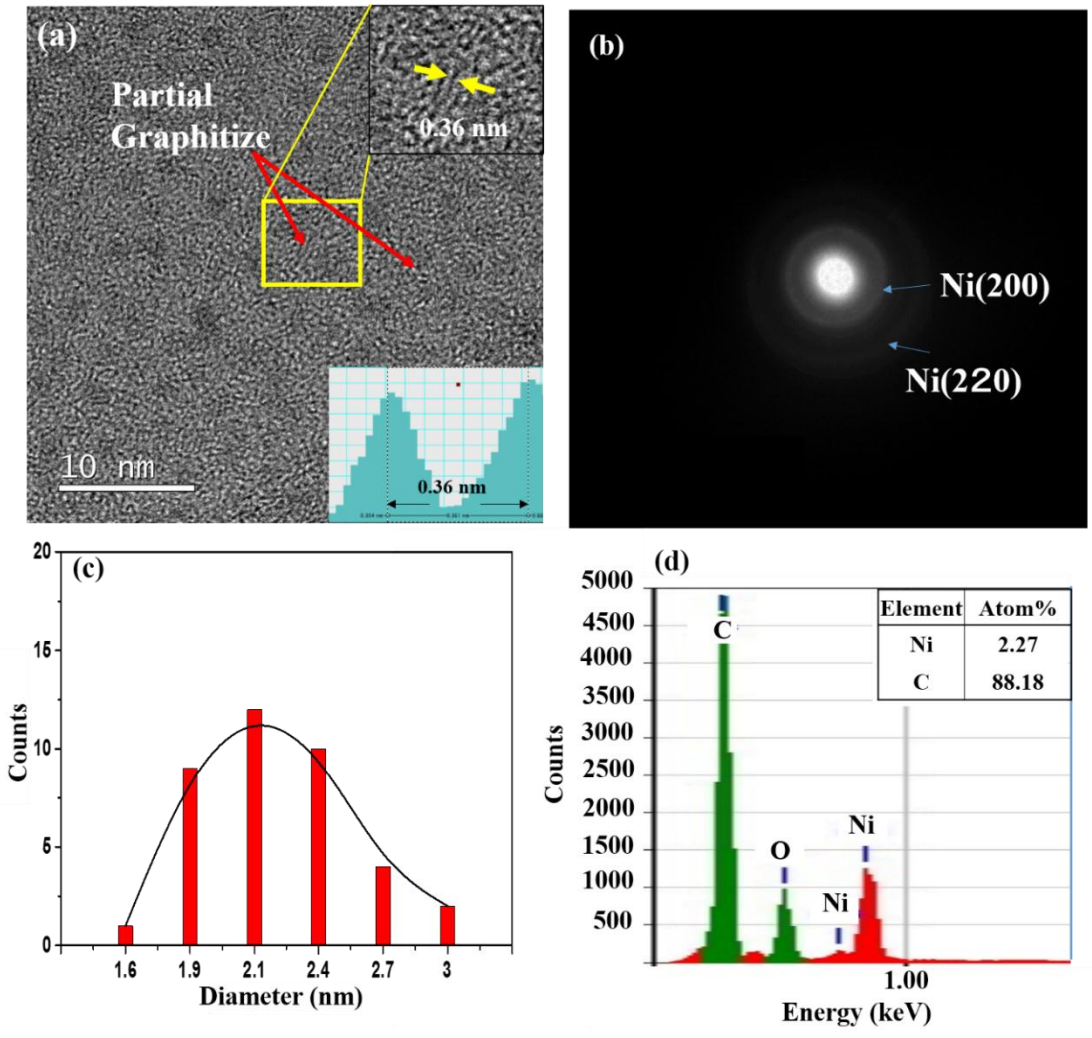

Figure 3.4: (a) TEM image of a 0.75-Ni-C film deposited on a microgrid at RT. (b) SAED pattern corresponding to (a). (c) and (d) Size distribution of Ni NPs and EDS spectrum measured in (a), respectively.

Fig. 3.5(a, b) show a typical TEM image and a corresponding SAED for 0.75-Ni-C film deposited at 50°C. Obviously, in **Fig. 3.5(a)**, NPs were densely dispersed, and lattice fringes corresponding to graphite (002) lattice are also observable by careful inspection. It should be stressed that Ni oxides (weak NiO (021) Deby ring) were contained together with metallic Ni NPs in the 0.75-Ni-C film, as seen in **Fig. 3.5(b)**. **Fig. 3.5(c)** shows the size distribution of NPs measured for **Fig. 3.5(a)**, revealing that the average size of the NPs is about ~2.5 nm, which is larger than that of 0.25-Ni-C films.

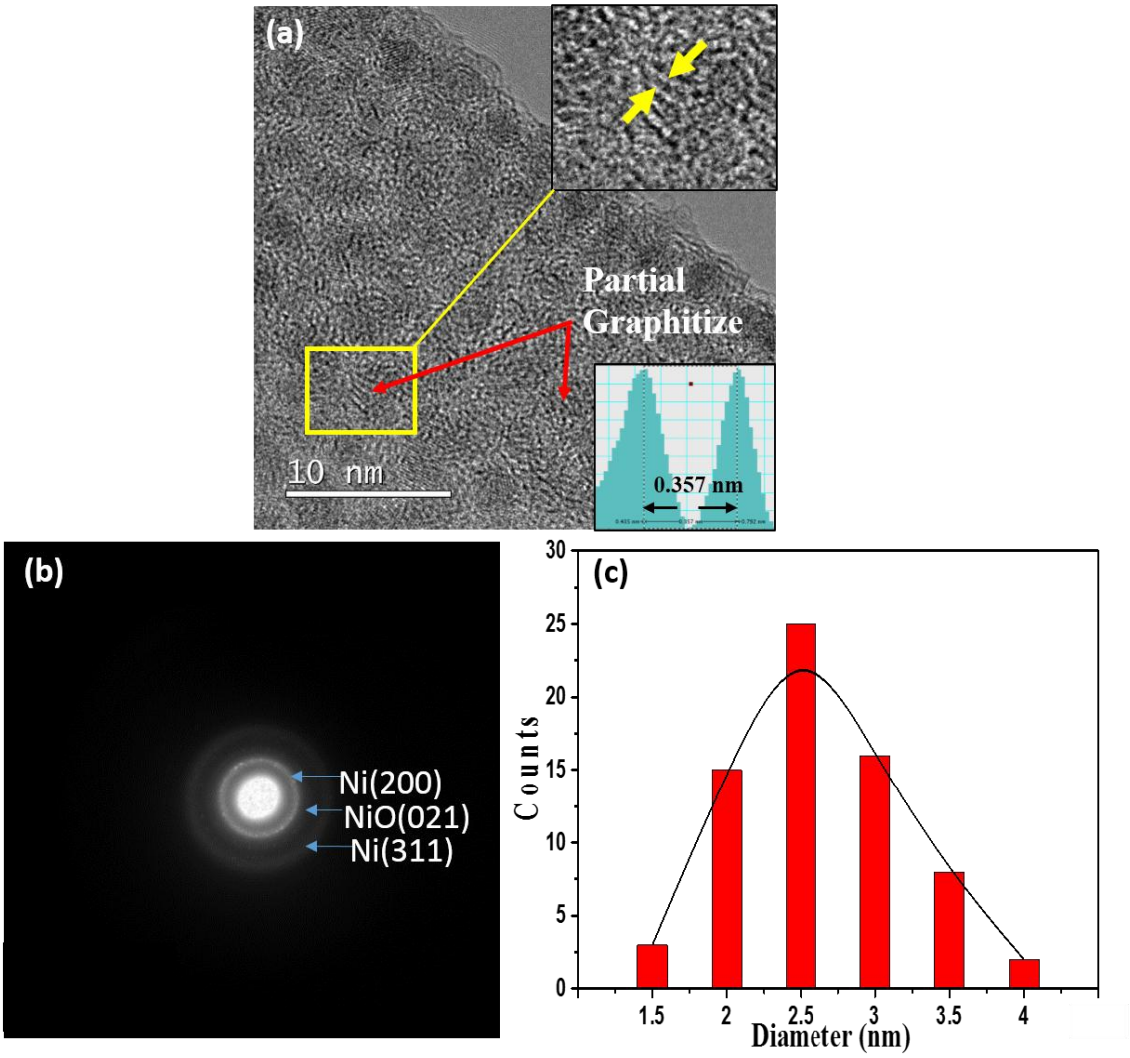

Figure 3.5: (a) TEM image of a 0.75-Ni-C film deposited at 50°C. (d) and (c) SAED pattern corresponding to (a), and size distribution of Ni NPs measured in (a), respectively.

In order to confirm the graphitization for the 0.75-Ni-C films more quantitatively, the Raman analyses were also performed of the Ni-C/SiO_2/Si at RT and 50^{o}C. **Fig. 3.6** shows their optical microscope images and Raman spectra. Similar to the 0.25-Ni-C films, the agglomerated-like regions in greenish color were observed in the optical microscope images in **Fig. 3.6(a, b)**. However, different from the 0.25-Ni-C films, no distinct 2D peak was detected even at the agglomerated-like greenish regions for the 0.75-Ni-C films independent of the deposition temperature. The 0.75-Ni-C films were feature by two peaks corresponding to D and G peaks at 1354 and 1565 cm^{-1} for the film deposited at RT, and 1356 and 1585 cm^{-1} for the film deposited at 50^{o}C. The peak–intensity ratio of the D to G peaks (I_D/I_G) were about 0.9 independent of the deposition temperature for 0.75-Ni-C films. Those spectra were almost similar to that observed at region B for the 0.25-Ni-C film deposited at RT and 50^{o}C.

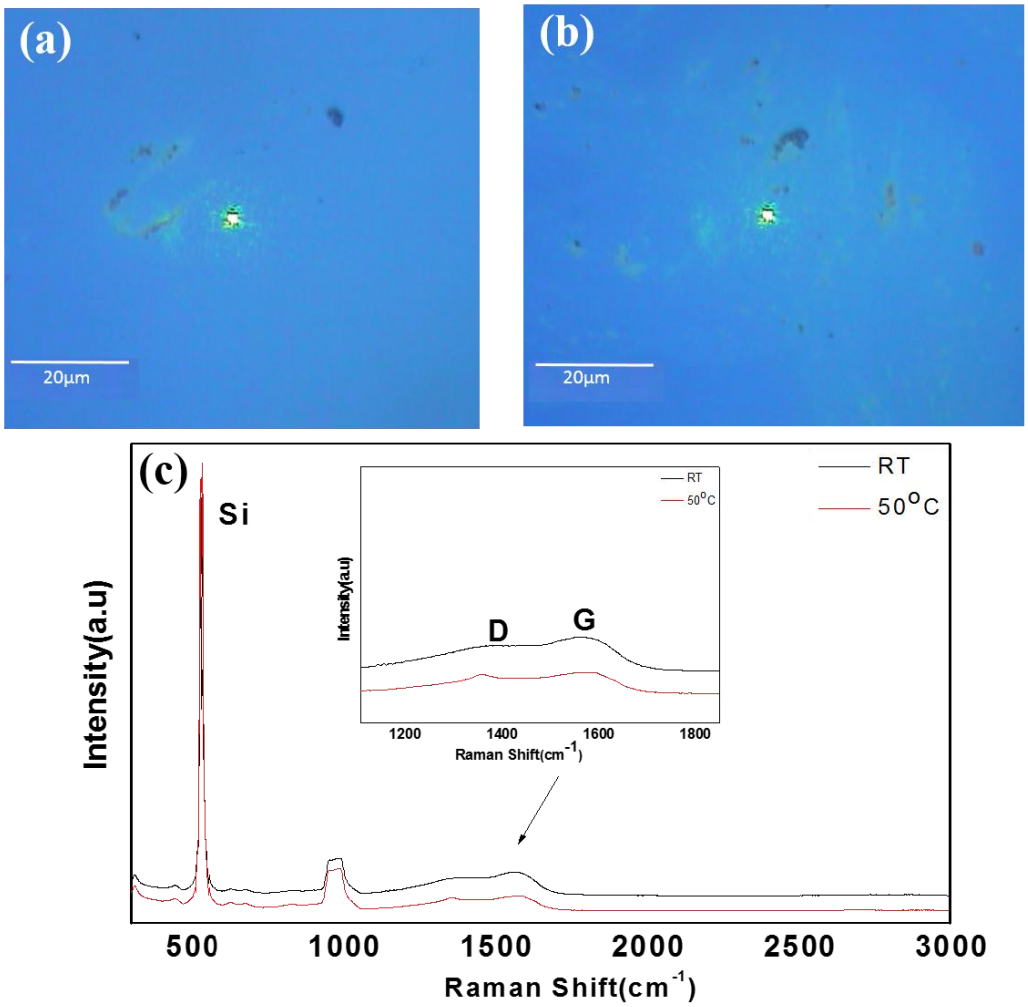

Figure 3.6: (a) and (b) optical images of the 0.75-Ni-C films deposited at RT and 50°C, respectively. (c) Raman spectra obtained at the agglomerated-like regions for the 0.75-Ni-C films deposited at RT and 50°C.

3.4. Discussion

As was newly found above, the spontaneous graphitization was enhanced at the deposition temperature of 50°C. However, this phenomenon was prominent only for the 0.25-Ni-C film. What is the mechanism for the spontaneous graphitization, and for its enhancement at 50°C? Why was it prominent only for the 0.25-Ni-C film?

For Ni-graphene system, based on the graphene growth performed under the ultra-high

vacuum conditions using single crystal Ni, different types of graphene growth modes have been identified depending on the growth temperature [8]. In brief, the ordered surface carbide formed first transforms to graphene at temperatures below 500^{o}C, whereas the carbon diffusion into Ni and the precipitation of graphene is the main mechanism at the high temperature growth. In the latter case, the carbon solubility is an important factor.

In the present experiments, no trace of carbide was detected. So, the low-temperature growth mode of the transformation from carbide to graphene would be ruled out. As is well-known, melting point strongly depends on the size of the crystal. It decreases with a decrease in crystal size. So, in the present case, Ni NPs would be in the similar situation to the high temperature growth mode. In addition, carbon solubility of NPs generally tends to increase with decreasing the size, because a large fraction of C should be expected close to the surface and the surface to volume ratio becomes larger for the smaller size of NPs [9–13]. This is also the case for Ni NPs [12]. The high carbon solubility into the catalyst usually yields the MLG readily. Furthermore, atomic diffusion on metal surfaces for NPs is commonly predictable to be much faster than for the bulk [14, 15]. These would be the driving force of the spontaneous graphitization observed here.

The enhancement of the spontaneous graphitization at 50^{o}C would be readily understandable, because the solubility and diffusion rate generally increase with an increase of the temperature [16]. At the deposition temperature of 50^{o}C, NPs were slightly larger in average size than those prepared at RT. This would be due to the enhanced agglomeration at the elevated deposition temperature. In this agglomeration process, C solubility would slightly decrease with increasing the size, yielding graphitized layer behind the trace of the moved and agglomerated NPs, as is depicted in **Fig. 3.7(a)**. This would be the reason why graphitization occurred not only at the surrounding of Ni NPs, but also in-between NPs.

Such a remarkable spontaneous graphitization occurred only for the 0.25-Ni-C film. As

seen in **Figs. (3.4 and 3.5)**, larger NPs were densely dispersed in the 0.75-Ni-C films. In addition, in those films, intense oxygen peak and Debye ring corresponding to Ni oxide were observed in EDS and SAED, respectively. From those facts, some parts of the NPs were thought to be out of the film plane to be oxidized as depicted in **Fig. 3.7(b)**. Once Ni NPs are oxidized, graphitization is known to be disturbed [5]. In addition, C solubility would be lower for the 0.75-Ni-C film, because, the size of NPs was larger for the 0.75-Ni-C film than that of 0.25-Ni-C film. These would be the reason why the less prominent spontaneous graphitization occurred for the 0.75-Ni-C films.

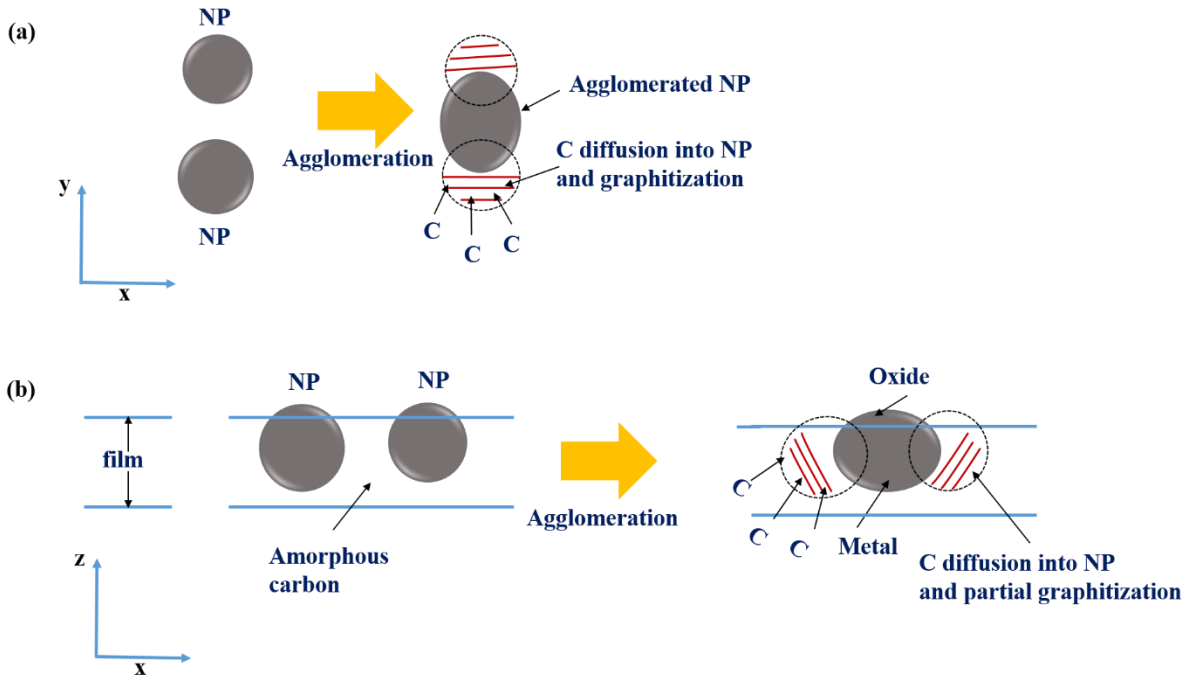

Figure 3.7: Schematic (a) top-view and (b) side-view illustrations of the graphitization in agglomeration process during the film deposition for the 0.25-Ni-C at RT and 0.75-Ni-C at 50^{o}C films, respectively.

3.5. Conclusions

In conclusion, the spontaneous graphitization was demonstrated for C films containing Ni NPs deposited on SiO_2/Si and microgrid substrates by magnetron sputtering at RT and at 50^{o}C, as confirmed by TEM and Raman spectra. The spontaneous graphitization was attributed mainly to the increased solubility for metallic Ni NPs, and was enhanced at the deposition temperature of 50^{o}C. For the C films contained larger and denser NPs, the accelerated spontaneous graphitization was not prominent, due to the partial oxidization of Ni NPs. The graphitization using NPs will open up a new strategy for the lower temperature growth of graphene.

3.6. References

[1] R. Addou, A. Dahal, P. Sutter and M. Batzill, Appl. Phys. Lett., 2012**, 100**, 21601.

[2] J. Kwak, J. H. Chu, J. K. Choi, S. D. Park, H. Go, S. Y. Kim, K. Park, S. D. Kim, Y. W. Kim, E. Yoon, S. Kodambaka and S. Y. Kwon, Nat. Commun., 2012, **3**, 645.

[3] W. Xiong, Y.S. Zhou, W.J. Hou, T. Guillemet, J.F. Silvain, Y. Gao, M. Lahaye, E. Lebraud, S. Xu, X.W. Wang, D.A. Cullen, K.L. More, L. Jiang, Y.F. Lu, RSC Adv. 2015, **5**, 99037.

[4] L. Lu, J. T. M. De Hosson and Y. Pei, Mater. Des., 2018, **144**, 245.

[5] K. Asaka and Y. Saito, Carbon, 2016, **103**, 352.

[6] A. C. Ferrari and J. Robertson, Phys. Rev. B, 2001, **64**, 75414.

[7] K. Asaka and Y. Saito, Surf. Interface Anal., 2016, **48**, 1203.

[8] A. Dahal and M. Batzill, Nanoscale, 2014, **6**, 2548.

[9] A. G. Nasibulin, P. Queipo, S. D. Shandakov, D. P. Brown, H. Jiang, P. V. Pikhitsa, O. V. Tolochko and E. I. Kauppinen, J. Nanosci. Nanotechnol., 2006, **6**, 1233.

[10] S. Reich and C. Thomsen, Philos. Trans. R. Soc. A, 2004, **362**, 2271.

[11] R. B. Mclellan, Scr. Met., 1969, **3**, 389.

[12] M. Diarra, A. Zappelli, H. Amara, F. Ducastelle and C. Bichara, Phys. Rev. Lett., 2012, **109**, 185501.

[13] L. Baraton, Z. He, C. S. Lee, J. L. Maurice, C. S. Cojocaru, A. F. Gourgues-Lorenzon, Y. H. Lee and D. Pribat, Nanotechnology, 2011, **22**, 85601.

[14] R. Anton, Carbon, 2009, **47**, 856.

[15] Helveg S, Lo´pez-Cartes C, Sehestad J, Hansen PL, Clausen BS, Rostrup-Nielsen JR, J. R. Rostrup-nielsen, F. Abild-pedersen, J. K. Nørskov, Nature, 2004, **427**, 5.

[16] Y. Bleu, V. Barnier, F. Christien, F. Bourquard, A. Loir, F. Garrelie and C. Donnet, Carbon, 2019, **155**, 410.

Chapter 4

4. One-Step Synthesis of Spontaneously Graphitized Nanocarbon Using Co Nanoparticles

4.1. Introduction

In this chapter, the strategy to reduce the graphitization temperature using NP form was tested for another catalyst metal, Co. Co is a well-known catalyst for graphene growth and possesses a higher C solubility than Ni [1]. Thus, a similar catalytic ability in the low-temperature graphitization may be expected for Co NPs [2-4]. In addition, C film containing Co NPs (referred to a Co-C film hereafter) attracts the great interest for various applications such as magnetic data storage and magnetic resonance imaging [5]. So, the successful low-temperature graphene growth will be essential for a wider range of practical applications. Abd Elhamid et al. have synthesized graphene at RT by pulsed laser deposition (PLD) of highly oriented pyrolytic graphite target on complex Ni-Cu substrates [6]. Very recently, Nakajima et al. have demonstrated the formation of MLG films directly on SiO_2 glass substrate using amorphous carbon at a temperature as low as 400°C by a simple sputtering technique using Co catalysts with high carbon solid solubility of Co [7]. In what follows, I will deal with the spontaneous graphitization at RT by simple one-step syntheses of Co-C films for the first time, leading to a strategy to achieve the ultra-low temperature graphene growth.

4.2. Experimental Method

The deposition of Co-C films was performed at RT onto commercially available microgrids (NS-M15, Okenshoji) for TEM and SiO_2 covered Si substrates (SiO_2/Si) using radiofrequency (RF) magnetron sputtering (SCOTT-C3 (VTR-151M/SRF), ULVAC KIKO Inc.) under base pressure of 3.0×10^{-4} Pa. Ar plasma was used for the film deposition. The RF power was set to 30 W and the deposition time was 5 min. For the Co-C film deposition, a carbon (graphite) disk 50 mm in diameter with an attachment of a small Co platelet (referred to a Co-C target hereafter) was prepared. The thicknesses of the deposited Co-C film were 7 nm.

The prepared films were analyzed by Raman spectroscopy (NRS 3300 laser Raman spectrometer), at laser wavelength 532.08 nm. TEM analyses were performed using a high resolution TEM, JEM ARM 200F, operating at 200 kV, equipped with dispersive x-ray spectroscopy (EDS). The crystallographic structure was analyzed by an x-ray diffraction (XRD) system (Rigaku RINT 2100 diffractometer) equipped with a Cu target. The Ni-filtered Cu Kα radiation (λ=1.5408 Å) was used. The X-ray tube voltage and current were 40 kV and 30 mA, respectively. For the chemical state analysis of the film, XPS measurements were performed using a Kratos Analytical Axis UltraDLD UHV spectrometer with a monochromatized Al Kα X-ray source (1486.6 eV). The take-off angle was 90^o and the constant analyzer energy mode was employed. The pass energy of the survey scan was 120 eV and the narrow scan was 20 eV. In order to obtain the in-depth information of the Co-C films, light sputtering with Ar^+ ions at 5 kV for 1 min was done. The ion incidence angle was 60^o normal to the surface. The ion current density and the etching rate were 0.5 mA/cm^2 and ~1 nm/min, respectively. During the ion etching, the working pressure was kept at 1×10^{-5} Pa, due to the differential pumping. The XPS spectra obtained were deconvolved using curve fitting on an 80/20% Gaussian/Lorentian peak. All the resolved peaks were used for both qualitative

identification and semiquantitative calculations. Regarding the peaks used, the sufficient background was fulfilled for the comparison.

4.3. Result and Discussion

Fig. 4.1(a) shows a typical high-magnification TEM image of a Co-C film deposited onto a microgrid. At a glance, black contrast parts dispersed over the film. As is typically exemplified by rectangular A in **Fig. 4.1(a)**, a careful inspection of some black contrast parts showed the lattice fringes of 0.202 nm spacing corresponding to Co (002), indicating that the black contrast parts were Co NPs. An inset in **Fig. 4.1(a)** is a further magnified image of the rectangular region B in **Fig. 4.1(a)**, disclosing the ordered lattice fringes of the short-range between the black contrast parts. The spacing of the ordered fringes was measured to be ~0.345 nm which corresponds to the lattice spacing of graphite (002). Such a short-range ordering corresponding to graphite (002) was observed over the film and some of them were indicated by yellow arrows in **Fig. 4.1(a)**.

Fig. 4.1(b) shows a fast Fourier transform (FFT) image taken from the whole area shown in **Fig. 4.1(a)**. The FFT is composed of spotty rings and a relatively broad ring corresponding to the graphite (002) plane. The relatively broad ring indicates that the crystallite was quite small in size, agreeing well with the observation in **Fig. 4.1(a)**. In **Fig. 4.1(b)**, spotty ring patterns corresponded to Co (002), (101), (102), (103), and CoO (002) planes. The size distribution of the Co NPs (black contrast parts) in **Fig. 4.1(a)** is shown in **Fig. 4.1(c)**, revealing that the NPs ranged from ~1.8 to ~2.8 nm in size with an average size of ~2.1 nm and the number density of the NPs was ~6.3×10^4 μm^{-2}. The Co/C concentration ratio was determined to be 2.78/88.85 from EDS analysis, as seen in **Fig. 4.1(d)**. Agreeing with the FFT in **Fig. 4.1(b)**, the oxygen peak in the EDS spectrum is approximately as large as the Co peak.

Fig. 4.2 shows the XRD pattern for a Co-C film deposited onto a SiO_2/Si. It can be seen that the as-prepared sample shows a broad diffraction peak at about 2θ=20° (see **Fig. 4.2(b)**) corresponding to graphite (002) plane commonly observed for reduced graphene oxides (rGOs) [8-10]. The broad peak would be due to the localized graphitized region and the imperfect crystallinity of the graphitic layers as seen in the TEM image (**Fig. 4.1(a)**). The XRD pattern in **Fig. 4.2** exhibits the peaks indexed as Co (004), CoO (111), Si (400) and Co (110) at 2θ = 33, 62, 69 and 75°, respectively.

In order to confirm the graphitization more quantitatively, the film deposited onto a SiO_2/Si substrate was analyzed by Raman spectroscopy. An optical microscope image is shown in **Fig. 4.3(a)**, disclosing those flake-like regions of dark contrast indicated by arrows located on the flat surface of blue color (background-like region). **Fig. 4.3(b, c)** show Raman spectra obtained at the flake-like region and the surrounding background-like region in **Fig. 4.3(a)**, respectively. As seen in **Fig. 4.3(b)**, the spectra obtained from the flake-like region consists of intense G and 2D peaks centered at 1587 and 2700 cm^{-1}, respectively, with an intense D peak at 1355 cm^{-1}, revealing the formation of MLG with defects. By contrast, the Raman spectrum of the background-like region [**Fig. 4.3(c)**] was characterized by D and G peaks at 1390 and 1560 cm^{-1}, respectively. Although the distinct 2D peak was not observable in the Raman spectrum of the background-like region, the Raman spectrum for this region was different from the amorphous carbon film [11]. Also, the spectrum for the background-like region was quite similar to the spectra reported previously for partially graphitized samples [12,13]. The intensity ratios of D and G peaks (I_D/I_G) were calculated to be ~0.79 and 0.92 for the flake-like and background-like regions, respectively. The difference in Raman spectra for those regions would be explained as follows: Different from the surface of amorphous porous C microgrid for TEM, the deposited Co-C would agglomerate readily relatively in long-range, resulting in

the macroscopic flake-like region on the SiO_2 surface for Raman analysis. In this macroscopically agglomerated area, namely the flake-like regions, due to the easier movement of atoms, the inclusion of C atoms into clustering Co-C and precipitation of graphitic layer would occur more actively than at the surrounding area. The graphitization mechanism will be discussed later in detail. The present observations suggest that the spontaneous graphitization of a-C catalyzed by Co NPs occurs even at RT, similar to the case of Ni NPs [12].

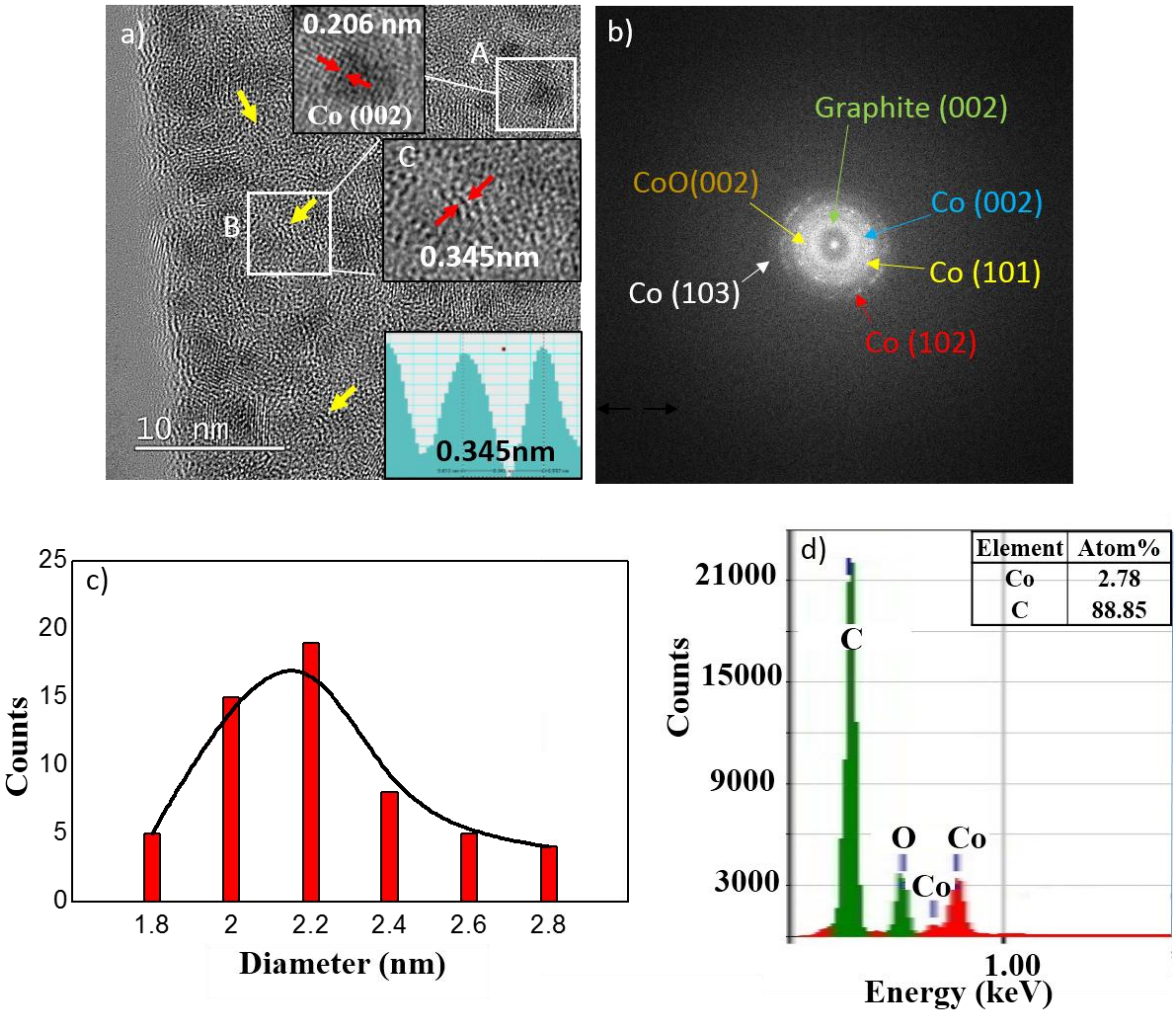

Figure 4.1: (a) TEM image of a Co-C film deposited on a microgrid at RT. The upper inset in (a) shows an enlarged image of the rectangular region B. The lower inset represents an intensity line profile of the arrow-indicated lattice region in the upper inset, indicating the interlayer spacing of 0.345 nm. (b) FFT image corresponding to (a). (c) Size distribution of Co NPs in Fig. 4.1(a), and (d) EDS spectrum of the Co-C film to estimate the Co content.

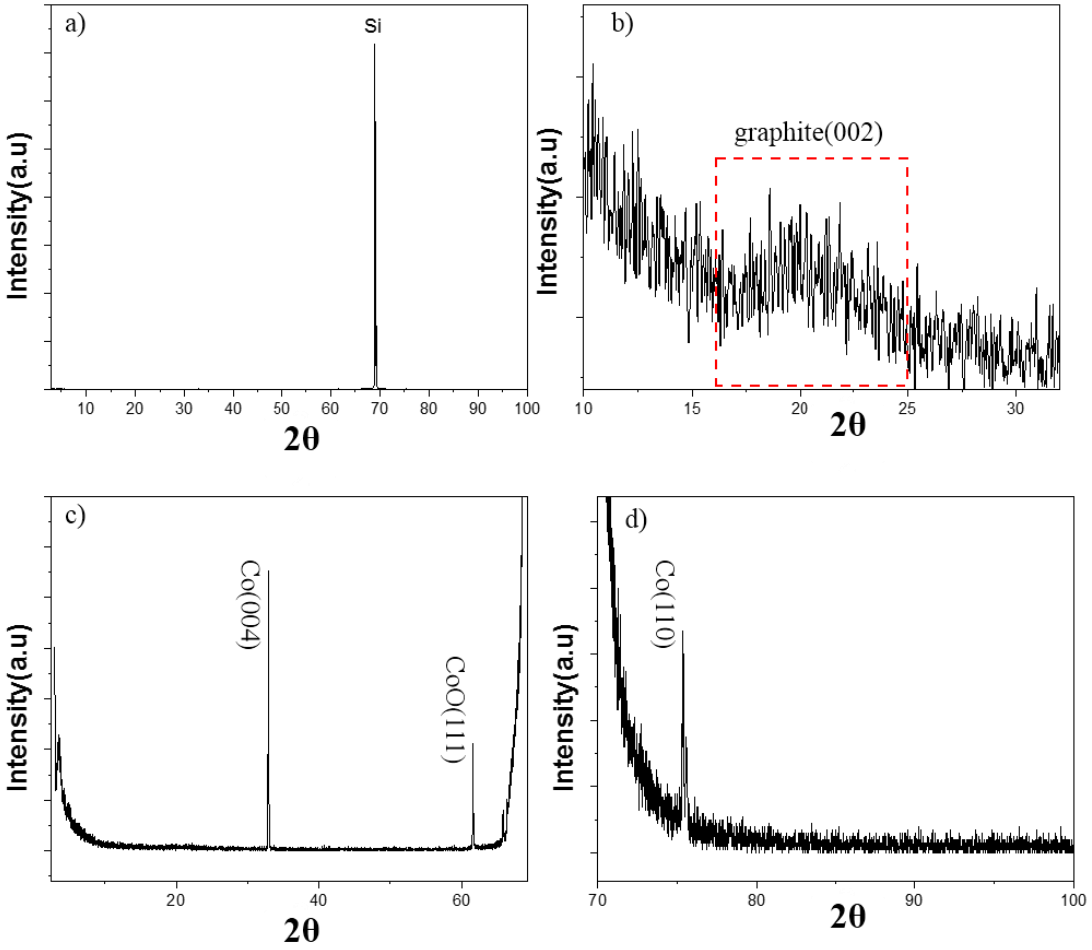

Figure 4.2: XRD spectra for a Co-C film deposited onto a SiO_2/Si. (a) Wide chart for the overall analysis, and (b)-(d) narrow charts. The dashed rectangular indicates the broad peak corresponding to the graphite (002) plane.

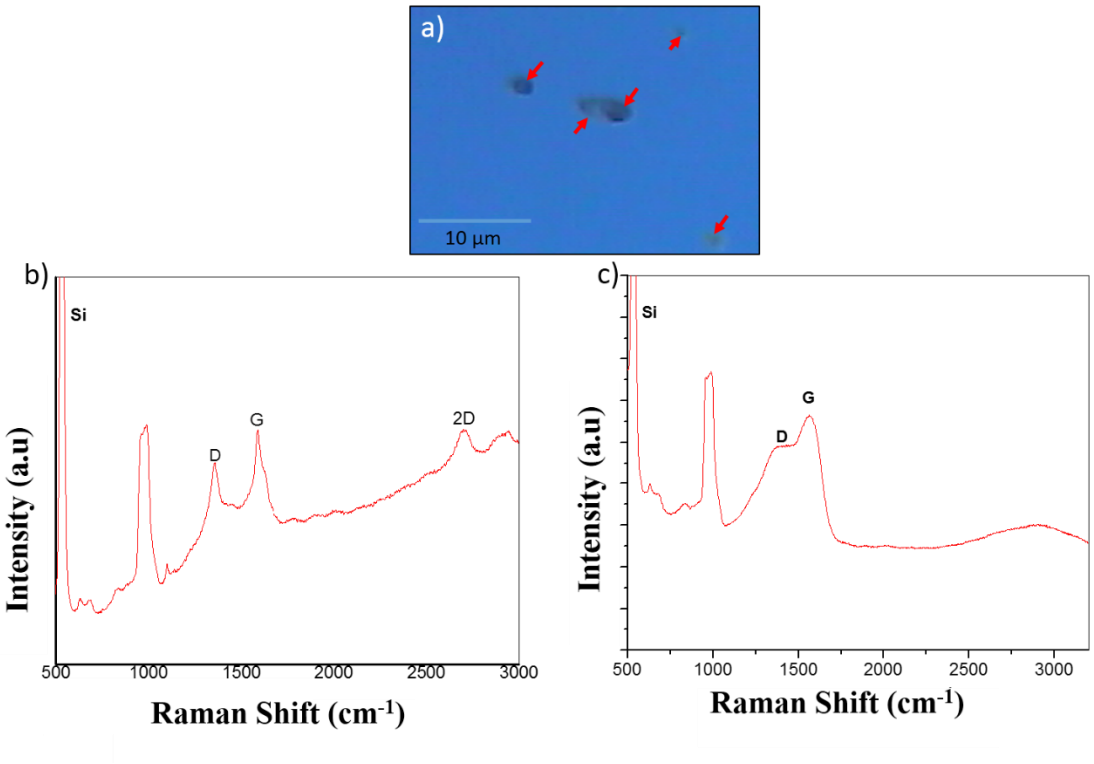

Figure 4.3: (a) optical microscope image of a Co-C film deposited on SiO_2/Si at RT. (b) and (c) Typical Raman spectra taken at one of the arrow-indicated flake-like regions of the dark contrast and surrounding region of the blue color in (a), respectively.

For the further confirmation of the chemical states of the respective elements, XPS measurement before and after the light sputtering was carried out for a Co-C film deposited on a SiO_2/Si at RT. **Fig. 4.4(a)** shows the survey spectra of the C-Co film, revealing that Co was prominent after the light sputtering. As is also seen in Co 2p3/2 peak, **Fig. 4.4(b)**, the chemical states of Co NPs in the film was different from that at the top surface; metallic Co was preserved in the film even after the exposure to air, whereas the metallic state was not clear at the top surface due to the surface oxidization and contamination. **Fig. 4.4(c)** shows a narrow spectra of the C1s peak. The peaks at about 284~285 and ~288.6 eV were assigned to C-C and C=O components, respectively, and a bump at ~286 eV was attributed to the C-O component. For NPs in the film, C=O and C-O components dramatically reduced and the splitting of C-C

related peak was observable. For precise analysis, deconvolution of the C1s spectrum obtained after light sputtering was carried out as shown in **Fig. 4.4(d)**. Apparently, C-C related peak consisted of two components peaked at 283.52 and 284.53 eV. The former peak position is closed to the reported value for the graphitic sp^2 carbon [14], while the latter would be general C-C bonding including the sp^3 component [15]. From the XPS analyses, it is concluded that the metallic state of Co NPs was preserved and the graphitization occurred in the film. This agrees well with the TEM observation shown in **Fig. 4.1**

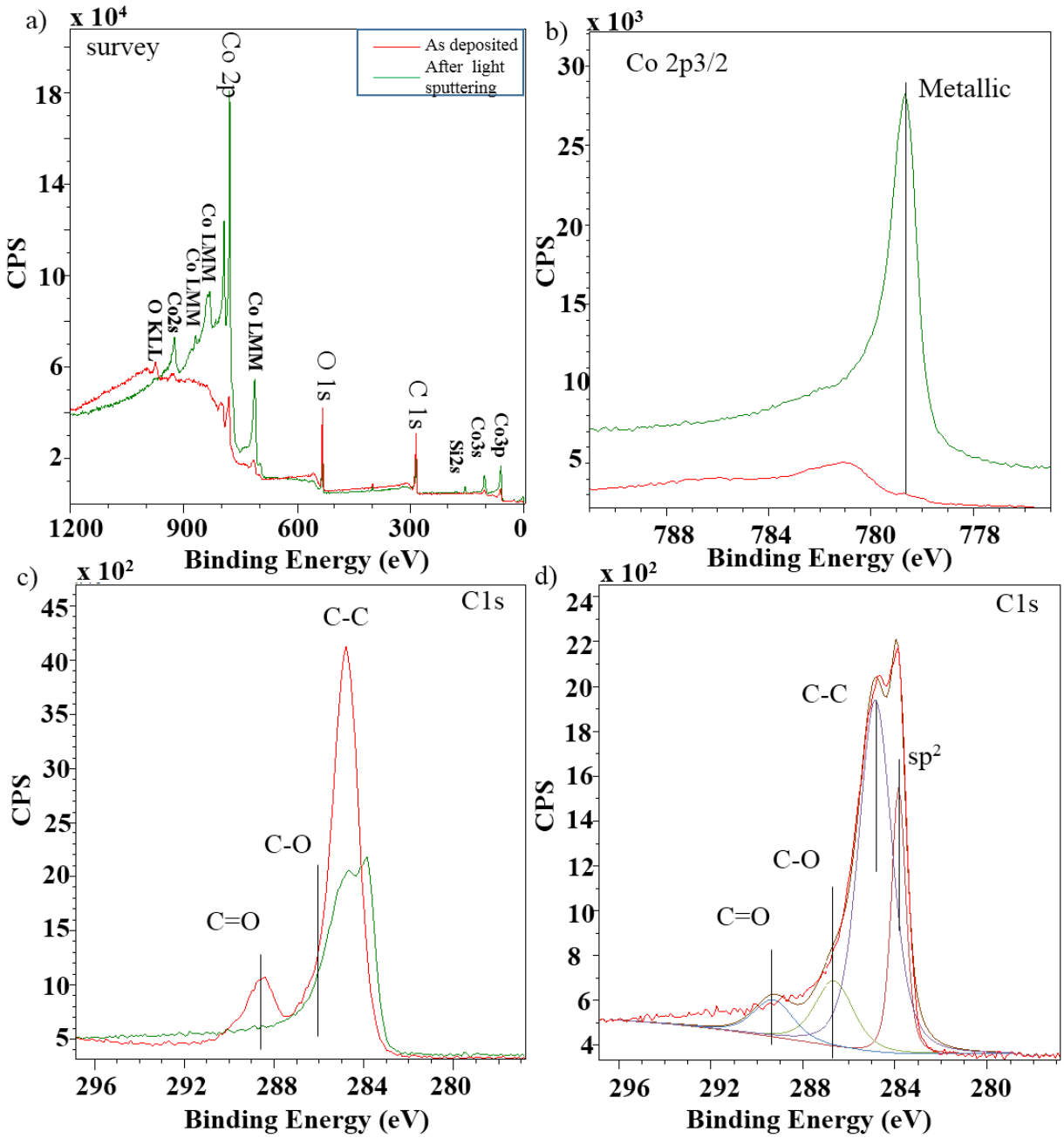

Figure 4.4: XPS spectra of a Co-C film deposited on a SiO_2/Si substrate. (a) Survey and narrow spectra of (b) Co $2p_{3/2}$ and (c) C 1s taken before (red line) and after (green line) light sputtering of the film. (d) The curve fitting result of the C 1s peak for the spectrum taken after light sputtering in (c).

The mechanism of the graphitization of NPs-carbon composite films at RT and the negative effect of the oxide in the graphitization were discussed elsewhere for Ni NPs [17]. In brief, with a decrease in particle size, in general, the melting point decreases while the carbon solubility increase [16-18]. For NPs-carbon composite films, due to the decrease in melting point, the situation of C atoms would be similar to that at high temperatures even at RT, namely, C atoms readily displace to form sp^2 bonding [9, 10]. In the film deposition process, agglomeration of NPs would occur, and the solubility of C would slightly decrease with increasing NP size in the agglomeration process, yielding a graphitized layer behind the trace of moving agglomerated NPs. It is also the case for Co NPs observed here.

It is interesting to compare the catalytic activity of NPs in graphitization at low temperature for Co with Ni. For the Ni NP case as was reported previously [12], no distinct 2D peak was detected in the Raman spectrum for the Ni-C film deposited on a SiO_2/Si at RT, where the average diameter of the Ni NPs (~2.1 nm), the atomic concentration ratio of Ni/C determined by EDS (2.27/88.18), and the partially oxidized situation of NPs were almost the same as the Co-C film tested here [12]. These facts indicate that the catalytic activity in low temperature graphitization is higher for Co than Ni. The heat of oxide formation is almost identical for Ni and Co [15], and the melting point is also almost identical for Ni (1728 K) and Co (1768 K). So, the possible reason for the difference in their catalytic activities in low temperature graphitization would be the difference in carbon solubility (2.03 for Ni, and 3.41 for Co at 1000 ^{o}C [1]). At an early stage of the film deposition, clustering of Co atoms would occur and a higher amount of C atoms would be included in clustering Co than in clustering Ni. Then, with their agglomeration, the C solubility would decrease slightly, resulting in a precipitation of graphitized layer behind the trace of agglomeration. The amount of the precipitation of graphitized layer would depend on the initially involved C content. This would

be the reason why Co is superior to Ni in the catalytic activity. The precipitation process will be similar to the growth process in the CVD. In fact, for the CVD growth also, better catalytic activity in graphene growth for Co films than Ni films was observed [4]. We are now planning the systematic investigation on the lower temperature graphitization using NPs for various metals. This is my future subject

4.4. Conclusions

In summary, I have studied the spontaneous graphitization of as-grown amorphous carbon films containing Co NPs catalyst at RT. Local graphitization has been confirmed by high-resolution TEM, XRD, Raman, and XPS analyses. Also, it was demonstrated that the metallic Co NPs were preserved even after the air exposure of Co-C films. Moreover, Co NPs showed better catalytic properties in the low-temperature graphitization than Ni NPs, likely due to the higher C solubility than Ni. Based on these findings, it was concluded that the amorphous C films containing Co NPs will be promising for the low-temperature graphitization.

4.5. References

[1] A. Dahal, and M. Batzill, Nanoscale. 2014, **6**, 2548.

[2] E. Kim, H. An, H. Jang, W.-J Cho., N. Lee, W.-G. Lee, and J. Jung, Chem. Vap. Deposition, 2011, **17**, 9.

[3] G. Amato, Materials, 2018, **11**, 257.

[4] P. Macháč, P. O. Hejna, P. Slepička, J. Electr. Eng., 2017, **68**,79.

[5] J. Majewska, B. Michalkiewicz, Appl. Phys. A., 2013, **111**, 1013.

[6] A. Elhamid, M. Abd, M. A. Hafez, Diam. Relat. Mater. 2017, **80** 162.

[7] Y. Nakajima, H. Murata, N. Saitoh, N. Yoshizawa, T. Suemasu, K. Toko, ACS Omega. 2019, **4**, 6677.

[8] C. Zhang, X. Zhu, Z. Wang, P. Sun, Y. Ren, J. Zhu, Zhu, D. Xiao, Nanoscale Res. Lett., 2014, **9**, 490.

[9] B. Gupta, N. Kumar, K. Panda, V. Kanan, S. Joshi, I. V. Fisher, Sci. Rep., 2017, **7**, 45030

[10] J. Yan, Z. Fan, T. Wei, W. Qian, M. Zhang, F. Wei, Carbon, 2010, **48**, 3825.

[11] A. Cuesta, P. Dhamelincourt, J. Laureyns, A. M. Alonso, J. M. D. Tascon, Carbon, 1994, **32**, 1523.

[12] S. Elnobi, S. Sharma, I. Araby, B. Paudel, G. Kalita, M. Z.M. Yusop, M.E. Ayhand, M. Tanemura, RSC Advances. 2020, **10**, 914.

[13] K. Asaka, Y. Saito, Carbon, 2016, **103**, 352.

[14] C. J. Thambiliyagodage, S. Ulrich, P. T. Araujo, M. G. Bakker, Carbon, 2018, **134**, 452.

[15] J. Park, W. C. Mitchel, S. Elhamri, L. Grazulis, J. Hoelscher, K. Mahalingam, C. Hwang, S. K. Mo, J. Lee, Nat. Commun., 2015, **6**, 5677.

[16] L. Lu, J. D. Hosson, Y. Pei, Mater. Des. 2018, **144**, 245.

[17] E. A. Sutter, P. W. Sutter, J. Mater. Sci., 2011, **46**, 7090.

[18] R. B. Mclellan, Scr. Met. 1969, **3**, 389–391.

Chapter 5

5. Synthesis and Characterization of Li-C Nanocomposite for Easy and Safe Handling

5.1. Introduction

As summarized in chapters 3 and 4, metal NP is promising for LTG, and oxide formation impedes the LTG. Specifically, encouraged by the previous success that the metallic state of NPs dispersed in the carbon matrix was preserved, I challenged the fabrication of the Li-C NCs in this chapter. Li-C NC is expected to be promising as the catalyst for the LTG, because the movement of Li atoms during the charge-discharge process in the battery operation will induce the graphitization of a-C. So, this will be also a new strategy for LTG. Of course, Li-C NC will be attractive as the anode material of the LIBs of next generation. Li-C NC will be advantageous also for the easy and safe handling of Li, which is known to be quite reactive in the ambient air.

Various works have demonstrated the use of metallic Li as an anode material for LIBs. These works generally focus on finding a stable host material for Li storage [1–3], minimization of Li dendrite formation by electrolyte engineering [4], use of solid electrolytes [5, 6], and interface engineering [7, 8]. Stabilization of highly reactive Li metal by surface coating seems promising for stable SEI formation. Coating the Li anode with conductive oxides and sulfides has shown promising results [9, 10]. However, use of chemical reagents for surface coating requires perfect control to minimize the non-uniformity of the surface. Use of three-dimensional structures such as wires, fibers and tubes as current collectors has demonstrated a drastic reduction of Li dendrite formation [11, 12]. Yang et al. showed that uniform

electroplating of Li could be obtained on Cu nanowires, leading to a dendrite-less anode [11]. A carbon matrix has been traditionally used to encapsulate metal/metal oxides, such as NiO, $NiCo_2O_4$, Fe_2O_3, Fe_3O_4, MnO_2, CuO, ZnO, Ge and Sn/SnO_2, forming carbon–metal composites used as anode materials for LIBs. A carbon-based scaffold prevents the large volumetric change during charge/discharge cycles, improving the performance of the battery [13–22].

5.2. Materials and Methods

Li-C NC was fabricated on the edge of a graphite foil. **Fig. 5.1(a)** shows the schematics of the sample fabrication method. Commercially available graphite foils, PERMA-FOIL®, TOYO TANSO Co. Ltd., with dimensions of 10 mm × 20 mm × 0.1 mm, were used as substrates. The graphite foil was placed vertically on a thick graphite sheet. Three to four shots of Li were placed in front of the standing graphite foil. Ar^+ ions with energy of 700 or 1000 eV were continuously bombarded on the graphite foil and Li shots at 45° for at least 30 min to form Li-embedded NC. During Ar^+ ion bombardment, C and Li atoms were ejected and redeposited in the form of conical structures, with Li nano-crystallites embedded in the C matrix to form conical Li-C NC (**Fig. 5.1(b, c)**). As seen in **Fig. 5.1(c)**, carbon-based nanofibers (CNFs) sometimes grew on the respective conical tips. A Kaufmann-type ion gun (Iontech. Inc. Ltd., model 3-1500-100FC) was used for the Ar^+ irradiation. Further information on the detailed fabrication process can be found elsewhere [23-28]. Characterization of synthesized Li-C NC was done using TEM JEM ARM 200F operated at 200 kV. A double-tilt TEM holder (JEOL; EM-Z02154T) was used without a liquid N_2-based cooling system for TEM observations. It is to be noted that no inert gas or vacuum system was used for the preparation and transfer of TEM samples. As synthesized, the sample was directly mounted onto a TEM holder for the TEM characterization.

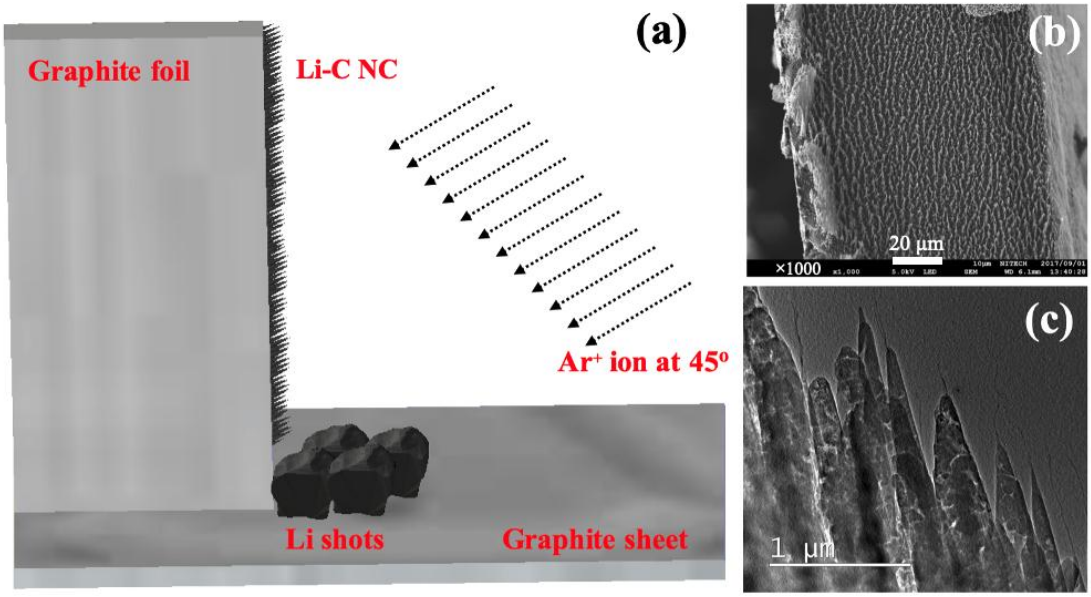

Figure 5.1: (a) Schematics showing sample setup for Li-C NC preparation. (b) SEM image showing the top view of Li-C NC grown on the edge of graphite foil. (c) Low-Mag TEM image showing Li-C NC fabricated by Ar^+ ion irradiation at 700 eV. CNFs grew on top of several conical structures, as exemplified by arrows.

5.3. Results

Fig. 5.1(b, c) shows the SEM and TEM images of the as-synthesized Li-C NC, respectively. The conical structures are almost unidirectional and freestanding. Their length and density can be controlled by changing the Ar^+ irradiation angle and the time of irradiation. As synthesized, Li-C NC was further characterized at higher magnification to confirm the presence of Li atoms. **Fig. 5.2(a)** shows the typical Li-C NC with a short CNF on top. CNFs of longer and slenderer size are unstable under an electron beam, making atomic-scale characterization difficult. Therefore, we selected the Li-C NC with a short CNF. **Fig. 5.2(b)**, shows the high magnification TEM image taken around the red squared area of **Fig. 5.2(a)**, showing the presence of Li atoms. The FFT corresponding to the electron diffraction pattern taken around the white square clearly shows sharp diffraction points, indicating the presence of crystalline Li. A high magnification TEM image was taken on the crystalline lattice of **Fig.**

5.2(b), as shown in **Fig. 5.2(c)**. Individual Li atoms were clearly visible, with a lattice distance of 0.24 nm corresponding to the (110) plane of Li [29]. It is to be noted that this the first report on the atomic-level observation of Li atoms under 200 keV TEM operating voltage without the use of a cooling holder and special sample fabrication methods, as reported in previous works [30]. During TEM observation, no damage to the Li lattice was observed, implying stability of Li nano-domains embedded in an amorphous carbon matrix. Elemental analysis of the Li-C NC was carried out using EELS. EELS spectra of **Fig. 5.2(d)** clearly show the Li peak at 57 eV, which is close to the reported value [18, 19]. It is clearly observed that Li-C NC can act as a host material to store Li, even in ambient conditions.

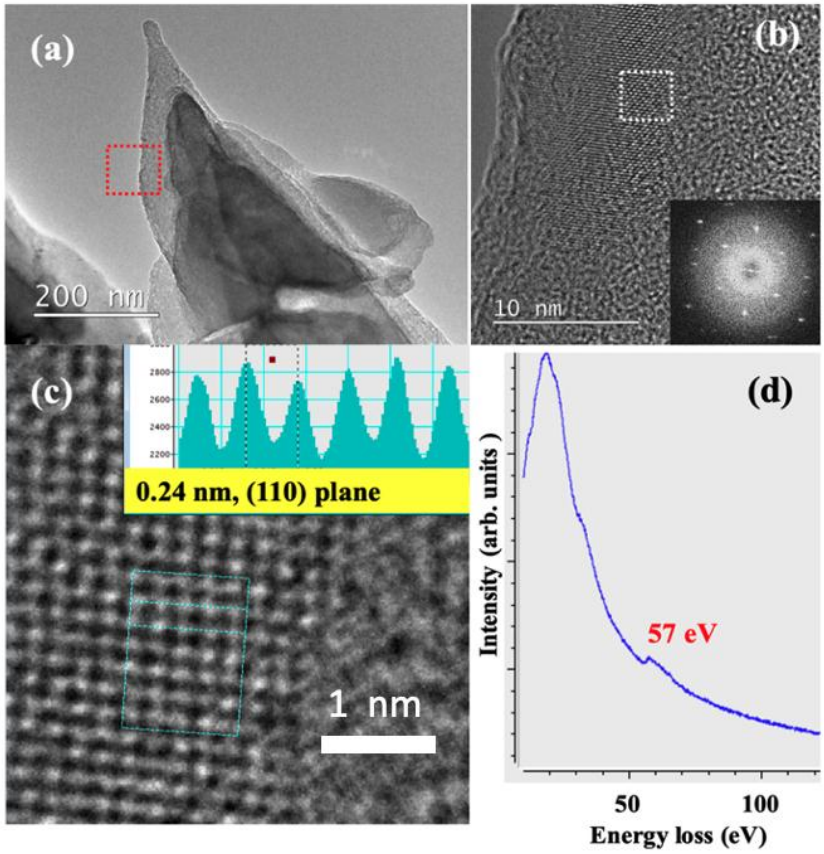

Figure 5.2: (a) TEM image of a typical Li NC (b) High mag TEM image of the squared area of Figure 2a (the inset shows the fast Fourier transform (FFT) pattern of the area indicated by the white square). (c) High mag TEM of the squared area of **Fig. 5.2(b)** showing Li lattice embedded in the C matrix. (d) EELS spectra showing the presence of Li at 57 eV.

After the optimization of the experimental conditions for the synthesis of Li-C NC, the effect of Ar^+ ion energy on the morphology and Li storage of Li-C NC was analyzed in the second set of experiments. To study the effect of the higher Ar^+ energy, Li-C NC was synthesized at 1 keV of beam energy. **Fig. 5.3(a)** shows the low magnification TEM image of the as-fabricated sample with Ar^+ ions sputtered at 1 keV. Interestingly, no particular array of Li-C NC was observed, contrary to the samples synthesized using 700 eV. The presence of a conical structure is observed at only a few places (inside the rectangular area), with most of the samples showing minor protrusions or the deposition of amorphous carbon. However, a large amount of Li was confirmed, as shown in **Fig. 5.3(b)**. During TEM observation, the expansion of a Li ball-like structure was observed, as indicated by arrows in **Fig. 5.3(b)**. **Fig. 5.3(c)** shows an example of rarely present conical NC, showing a large amount of Li attached to the surface of the NC (of the rectangular area of **Fig. 5.3(a)**). The inset shows the presence of Li on the tip of the conical NC. Interestingly, no Li lattice was observed inside the C matrix, but a Li-related lattice was visible on the surface of the conical NC, as shown in **Fig. 5.3(d)**. As seen in the inset, the line profile taken for the air-exposed atomic lattice shows a higher separation value of 0.257 nm, corresponding to Li_2O_2 (JCPDS card No. 01-074-0115). From this observation, it can be concluded that under the higher ion beam energy of 1 keV, an excess of Li, which is reactive in air, is sputtered and supplied onto the Li-C NC, suggesting that the Li-C NC formed at higher ion energy densities would be less suitable for battery applications. Previous works have also shown that for the fabrication of metal-embedded CNF, the quantity of metal should be optimum. It can be clearly observed that 700 eV is the preferable energy for the fabrication of Li-embedded NC.

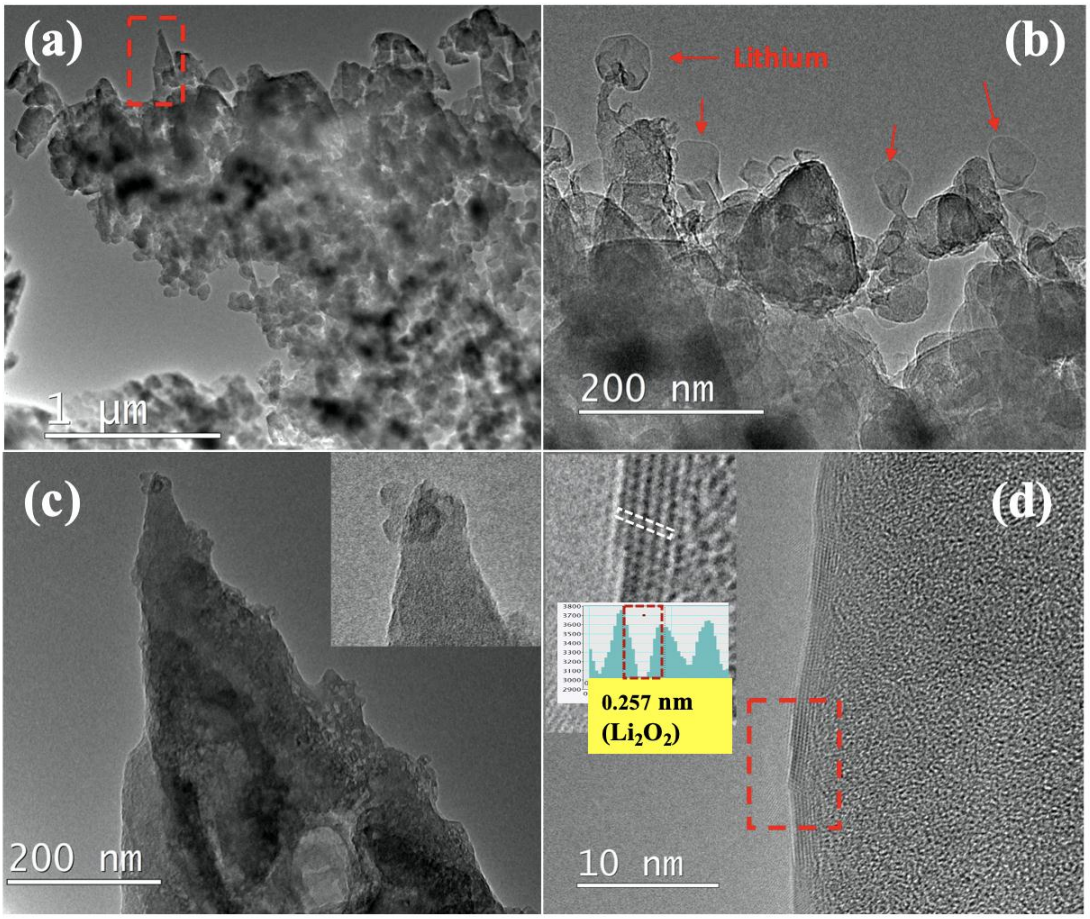

Figure 5.3: (a) Low mag. TEM image showing Li-C NC fabricated at 1keV of Ar^+ (b) Red arrows showing Li balls observed during TEM observation (c) Conical Li-C NC synthesized at 1 keV (of the area indicated by the rectangular selection of **Fig. 5.3(a)**). (d) Edge of the conical Li-C NC showing the presence of the atomic lattice. The inset shows the presence of the Li_2O_2 lattice in the area indicated by the red rectangle.

Next, we deposited Li-C NC film on a microgrid TEM mesh so that the deposited film could be characterized without any transfer steps. **Fig. 5.4(a)** shows the low magnification TEM image of Li-C NC film on a Cu microgrid TEM mesh. **Fig. 5.4(b)** shows the patches of light and dark contrasted micro-areas, indicating different Li and C distributions. C is higher in atomic weight compared to Li, yielding darker contrast, whereas the Li-rich area appears as

bright micro-areas. A high magnification TEM image clearly shows the presence of the Li lattice (**Fig. 5.4c**).

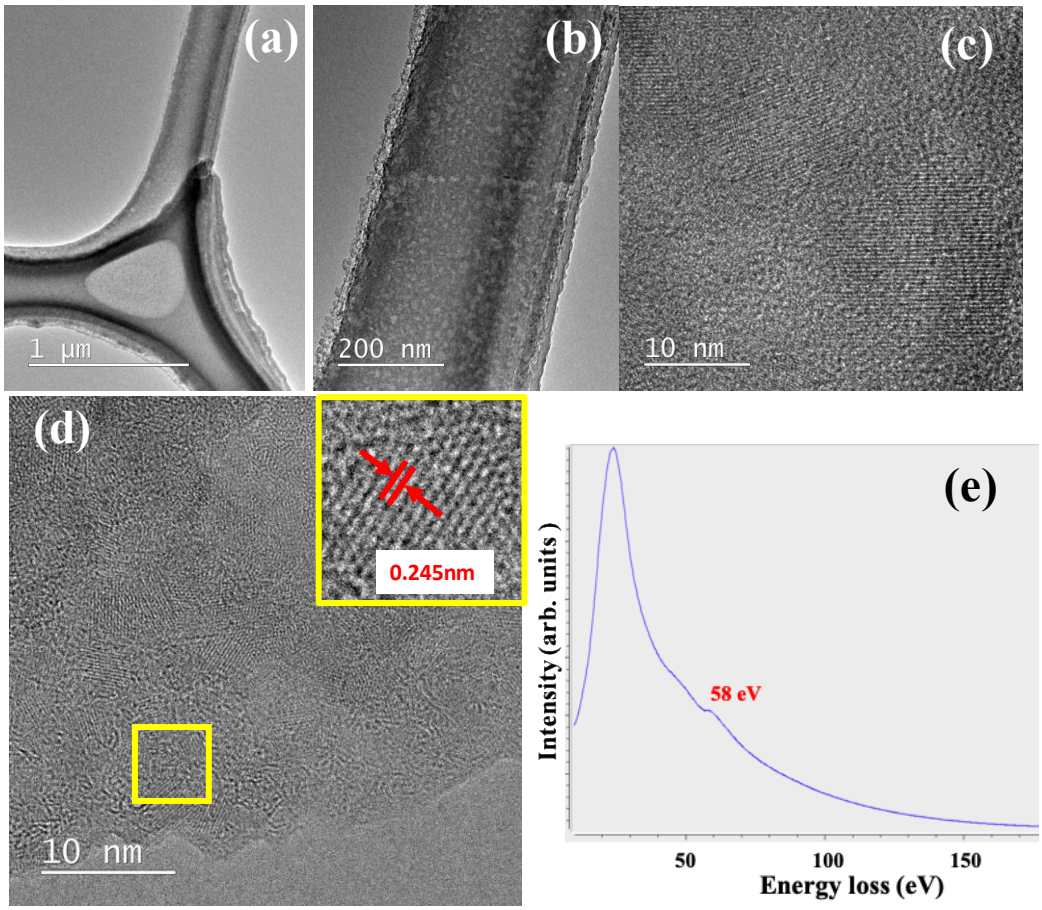

Figure 5.4: (a) Low mag. TEM showing Li-C NC film deposited on TEM mesh. (b) Typical Li-C NC film showing dark and bright spots indicating different distributions of Li and C. (c) High mag TEM image showing Li lattice in C matrix before annealing. (d) Li-C NC film after annealing for 10 min at 300°C. The inset presents the squared area showing the intact Li lattice (e) EELS spectra taken on the annealed sample showing the presence of pristine Li.

In order to study the role of the C matrix in protecting embedded Li crystallites, we heated a Li-C NC film deposited on a microgrid TEM mesh over a hot plate at 300°C for 10 min in ambient conditions. **Fig. 5.4(d)** shows a typical TEM image for the Li-C NC film after heating for 10 min. It is observed that Li lattices are protected in ambient conditions without apparent oxidation or change in morphology. The inset of **Fig. 5.4(d)** shows a high magnification TEM

image, revealing the pristine Li lattice with a lattice distance of 0.24 nm, corresponding to the (110) plane, and the preservation of Li was further confirmed by an EELS spectrum peaking at about 58 eV (**Fig. 5.4(e)**). This shows that amorphous C acts as a buffer, protecting Li from oxidation or exposure to moisture.

This simple ion beam-based Li-C NC fabrication can be adopted for the industrial-scale development of pre-lithiated anode material for battery applications. Li-C NC should be accessible for the electrochemical processes, as carbon in Li-C NC is mostly amorphous carbon, which is not much different from carbonaceous materials that are commonly used in commercial batteries. In order to confirm this, we are now planning to measure its charge/discharge property by assembling a prototype of a battery, and to also carry out the in-situ TEM observation of this charge/discharge process using Li-C NC and Li-C composite films based on our in-situ TEM technique using CNFs [23, 24, 31]. The results will be reported in forthcoming papers.

5.4. Conclusions

In summary, I developed a novel method for the fabrication of Li-embedded NC using an ion beam setup. Li inside NC was found to be well preserved from oxidation during handling in ambient conditions. Further, no significant electron beam-related damage was observed on the Li lattice during TEM measurements. Since Li is pre-stored inside the NC, Li-C NC can be attractive as the anode material for the LIB battery. Further, the method was extended to fabricate Li-C NC films on microgrid TEM meshes, which can be easily extended to deposit Li-C NC films on any arbitrary substrates for the fabrication of battery electrodes. The next step is the in-situ TEM observation of the Li-C NC during the charge-discharge process for the low-temperature graphene formation. This is my future subject.

5.5. References

[1] D. Lin, Y. Liu, Z. Liang, H.-W. Lee, J. Sun, H. Wang, K. Yan, J. Xie, Y. Cui, Nat. Nanotechnol., 2016, **11**, 626.

[2] Y. Liu, D. Lin, Z. Liang, J. Zhao, K. Yan, Y. Cui, Nat. Commun., 2016, **7**, 10992.

[3] Z. Liang, D. Lin, J. Zhao, Z. Lu, Y. Liu, C. Liu, Y. Lu, H. Wang, K. Yan, X. Tao, Proc. Natl. Acad. Sci. USA, 2016, **113**, 2862.

[4] Y. Lu, Z. Tu, L. A. Archer, Nat. Mater., 2014, **13**, 961.

[5] N. Kamaya, K. Homma, Y. Yamakawa, M. Hirayama, R. Kanno, M. Yonemura, T. Kamiyama, Y. Kato, S. Hama, K. Kawamoto, Nat. Mater., 2011, **10**, 682.

[6] X. Han, Y. Gong, K. K. Fu, X. He, G. T. Hitz, J. Dai, A. Pearse, B. Liu, H. Wang, G. Rubloff, Nat. Mater., 2017, **16**, 572.

[7] G. Zheng, S. W. Lee, Z. Liang, H.-W. Lee, K. Yan, H. Yao, H. Wang, W. Li, S. Chu, Y. Cui, Nat. Nanotechnol., 2014, **9**, 618.

[8] N.-W. Li, Y.-X. Yin, C.-P. Yang, Y.-G. Guo, A Adv. Mater., 2016, **28**, 1853.

[9] A. C. Kozen, C.-F. Lin, A. J. Pearse, M. A. Schroeder, X. Han, L. Hu, S.-B. Lee, G. W. Rubloff, M. Noked, Acs Nano, 2015, **9**, 5884.

[10] Y. Cao, X. Meng, J. W. Elam, Chem. Electro. Chem., 2016, **3**, 858.

[11] C.-P. Yang, Y.-X. Yin, S.-F. Zhang, N.-W. Li, Y.-G. Guo, Nat. Commun., 2015, **6**, 8058 .

[12] A. Zhang, X. Fang, C. Shen, Y. Liu, C. Zhou, Nano Res., 2016, **9**, 3428.

[13] M. Y. Cheng, B. J. J. Hwang, J. Power Sources, 2010, **195**, 4977.

[14] Z. Fan, B. Wang, Y. Xi, X. Xu, M. Li, J. Li, G. Yang, Carbon, 2016, **99**, 633.

[15] M. Nagao, M. Otani, H. Tomita, S. Kanzaki, A. Yamada, R. Kanno, J. Power Sources, 2011, **196**, 4741.

[16] L. Zeng, C. Zheng, C. Deng, X. Ding, M. Wei, ACS Appl. Mater. Interfaces, 2013, **5**, 2182.

[17] F. Wu, R. Huang, D. Mu, X. Shen, B. Wu, J. Alloys Compd., 2014, **585**, 783.

[18] M. Yang, Q. Gao, Microporous Mesoporous Mater., 2011, **143**, 230.

[19] R. Guo, L. Zhao, W. Yue, Electrochim. Acta., 2014, **152**, 338.

[20] L. Shen, E. Uchaker, C. Yuan, P. Nie, M. Zhang, X. Zhang, G. Cao, ACS Appl. Mater. Interfaces, 2012, **4**, 2985.

[21] J. Ma, D. Xiang, Z. Li, Q. Li, X. Wang, L. Yin, CrystEngComm, 2013, **15**, 6800.

[22] X. Xu, Z. Fan, X. Yu, S. Ding, D. Yu, X. W. Lou, Adv. Energy Mater., 2014, **4**, 1400902.

[23] S. Sharma, M. S. Rosmi, Y. Yaakob, M. Z. M. Yusop, G. Kalita, M. Kitazawa and M. Tanemura, Carbon, 2018, **132**, 165.

[24] M. S. Rosmi, M. Z. Yusop, G. Kalita, Y. Yaakob, C. Takahashi and M. Tanemura, Sci. Rep., 2015, **4**, 7563.

[25] M. S. Rosmi, Y. Yaakob, M. Z. M. Yusop, S. Sharma, R. Vishwakarma, M. Ibrahim, G. Kalita and M. Tanemura, RSC Adv., 2016, **6**, 82459.

[26] Y. Yaakob, Y. Kuwataka, M. Z. M. Yusop, S. Tanaka, M. S. Rosmi, G. Kalita, M. Tanemura, Phys. Status Solidi (b), 2015, **252**, 1345.

[27] M. Tanemura, T. Okita, H. Yamauchi, S. Tanemura, R. Morishima, Appl. Phys. Lett., 2004, **84**, 3831.

[28] M. Tanemura, H. Hatano, M. Kitazawa, J. Tanaka, T. Okita, S.P. Lau, H.Y. Yang, S.F. Yu, L. Huang, L. Miao, Surf. Sci., 2006, **600**, 3663.

[29] Y. Li, Y. Li, A. Pei, K. Yan, Y. Sun, C.-L. Wu, L.-M. Joubert, R. Chin, A.L. Koh, Y. Yu, et al. Science, 2017, **358**, 506.

[30] X. H. Liu, J. Y. Huang, Energy Environ. Sci., 2011, **4**, 3844.

M. Z. M. Yusop, P. Ghosh, Y. Yaakob, G. Kalita, M. Sasase, Y. Hayashi and M. Tanemura, ACS Nano., 2012, **6**, 9567.

Chapter 6

6. Conclusions

6.1. Overall Conclusions

Most of the reported graphene synthesis include the high-temperature process. Nevertheless, low-temperature growth should be succeeded for a wider range of applied applications. Therefore, many efforts have been devoted to the lower temperature graphene synthesis and its low-temperature growth is still challenging in the graphene research field. To achieve this, metallic NP catalysts have been proposed in this thesis.

Two strategies were attempted to achieve the low-temperature graphene growth; the first one is the nano-sized catalyst to decreasing the melting point of the catalyst metal and to increase the carbon solubility and carbon diffusion. The second one is the decrease in the oxide formation. By using these strategies, the spontaneous graphitization was demonstrated for C films containing Ni or Co NPs deposited on SiO_2/Si and microgrid substrates by magnetron sputtering at RT and at 50^{o}C, as confirmed by TEM and Raman spectra. In both Ni and Co cases, a clear 2D peak in Raman spectra, which is the evidence of the graphene formation, was observed. The spontaneous graphitization was attributed mainly to the increased solubility for metallic NPs, and was enhanced at the deposition temperature of 50^{o}C as confirmed for Ni case. For the C films contained larger and denser Ni NPs the accelerated spontaneous graphitization was not prominent, due to the partial oxidization of Ni NPs. Co NPs showed better catalytic properties in the LTG than Ni NPs, likely due to the higher C solubility than Ni. Thus, the use

of NPs was concluded to be a key for LTG in the solid phase reaction. This finding will open up a new strategy for the lower temperature growth of graphene.

For the application of carbon matrix encapsulated metal/metal oxides, carbon-metal composites reported to display high catalytic activity for graphene formation at lower temperatures and high specific capacity and excellent cycling performance as anode materials of LIBs. So, novel method for the fabrication of Li-embedded NC has been developed using an ion beam setup. Li inside NC has been found to be well preserved from oxidation during handling in ambient conditions. The movement of Li atoms during the charge-discharge process in the battery operation is expected to induce the graphitization of a-C. So, this will be also the new strategy for the low temperature graphitization.

6.2. Future Prospect of the work

Some recommendations for future work were clarified based on the result and conclusion obtain from this work. As my next step, I will carry out the systematic investigation on the lower temperature graphitization using NPs for various metals to know what kind of metal is the best for the LTG. Also, I will challenge the synthesis of graphene "film" using the best catalyst determined in a series of my research work for the device application such as a transparent electrode and interconnection.

By lowering the graphene synthesis temperature, I will try to fabricate high quality graphene on various substrates including plastic substrates at ultra-low temperature with different combination of metals and study their catalytic properties especially for the development of energy-related applications, such as super capacitors, Li-air batteries. After the graphene film growth, surface morphologies, thickness, graphene quality, and crystalline structure will be examined by field emission SEM, atomic force microscope, Raman

spectroscopy, and atomic resolution TEM, respectively. Also, I will deal with the in situ TEM of charge-discharge cycles using Li-CNFs as an electrode for the development of batteries of next generation.

6.3. List of publications

1) Mona Ibrahim Araby, Subash Sharma, **Sahar Elnobi**, Golap Kalita, Masashi Kitazawa, Masaki Tanemura, Temperature dependence of catalytic activity in graphene synthesis for Sn nanoparticles, Journal of Materials Science: Materials in Electronics, 30 (2019) 12796–12803.

2) Subash Sharma, Balaram Paudel Jaisi, Mona Ibrahim Araby, **Sahar Elnobi**, Muhammed Emre Ayhan, Golap Kalita, Masaki Tanemura, The Mo catalyzed graphitization of amorphous carbon: an in situ TEM study, RSC Adv., 9 (2019) 34377.

3) **Sahar Elnobi**, Subash Sharma, Mona Ibrahim Araby, Balaram Paudel, Golap Kalita, Mohd Zamri Mohd Yusop, Muhammed Emre Ayhan, Masaki Tanemura, Room-temperature graphitization in a solid-phase reaction, RSC Adv., 10 (2020) 914.

4) Subash Sharma, Tetsuya Osugi, **Sahar Elnobi**, Shinsuke Ozeki, Balaram Paudel Jaisi, Golap Kalita, Claudio Capiglia, Masaki Tanemura, Synthesis and characterization of Li-C nanocomposite for easy and safety handling, Nanomaterials, 10 (2020) 1483.

5) Balaram Paudel Jaisi, Subash Sharma, **Sahar Elnobi**, Amr Attia Abuelwafa, Yazid Yaakob, Golap Kalita, and Masaki Tanemura, Graphitization of gallium-incorporated

carbon nanofibers and cones: In situ and Ex Situ transmission electron microscopy studies, Phys. Status Solidi B, 257 (2020), 2000309.

6) **Sahar Elnobi,** Subash Sharma,Tetsuya Ohsugi, Balaram Paudel, Golap Kalita, Mohd Zamri Mohd Yusop, Muhammed Emre Ayhan, Zhen Quan Cavin Ng, Daniel H.C. Chua, and Masaki Tanemura, One-step synthesis of spontaneously graphitized nanocarbon using cobalt-nanoparticles, SN applied science, 2 (2020) 2147.

6.4. List of conferences

1) Mona Ibrahim Araby, Subash Sharma, **Sahar Elnobi,** Golap Kalita, and Masaki Tanemura. Temperature dependence of catalytic activity in graphitization for Sn nanoparticles. 31st International Microprocesses and Nanotechnology Conference November 13-16, 2018, Sapporo Park Hotel, Sapporo, Japan.

2) Mona Ibrahim Araby, **Sahar Elnobi**, Subash Sharma, Golap Kalita, Masaki Tanemura, Mohd Zamri MohdYusop. Play with nanocarbon (low-dimensional carbon materials): From nanomaterials science to the real world, advanced nanomaterials and nanotechnology, January 2019, Mumbai, India.

3) Mona Ibrahim Araby, **Sahar Elnobi**, Subash Sharma, Golap Kalita, Masaki Tanemura, Mohd Zamri MohdYusop. Catalytic Activity on Low temperature graphene growth based on dynamic TEM Observations, International Conference on Advances in Materials Science & Applied Biology (AMSAB), January 2019, Mumbai, India.

4) Mona Ibrahim Araby, **Sahar Elnobi**, Subash Sharma, Golap Kalita, Masaki Tanemura, TEM in nanomaterials science-from nanoworld to real world**,** 10th International

Conference on Nanoscience and Nanotechnology 2019 (NANOSciTech 2019), Mar 2019, Shah Alam, Selangor, Malaysia.

5) Masaki Tanemura, Subash Sharma, Mona Ibrahim Araby, **Sahar Elnobi**, Mohamad Saufi Rosmi, Yazid Yaakob, Golap Kalita, Mohd Zamri MohdYusop, In-situ TEM visualization of graphitization process: Towards interconnection and nanosoldering applications for future nanodevices, The 2nd Global Forum on Advanced Materials and Technologies for Sustainable Development, Jul 2019, Toronto, Canada.

6) Masaki Tanemura, Subash Sharma, **Sahar Elnobi**, Mona Ibrahim Araby, Balaram Paudel Jaisi, Golap Kalita, Mohamad Saufi Rosmi, Yazid Yaakob, ontrollable synthesis and nano-soldering of graphitized nanocarbon towards the interconnection application, Graphene Week, Sep. 2019, Helsinki, Finland.

7) Masaki Tanemura, **Sahar Elnobi**, Subash Sharma, Mona Ibrahim Araby, Balaram Paudel Jaisi, Golap Kalita, M.E.Ayhan Mohd Zamri Mohd Yusop, Low-temperature growth of graphitized nanocarbon for flexible electrodes for wound healing process sensors, Graphene Week, Sep. 2019 Helsinki, Finland.

8) **Sahar Elnobi**, Subash Sharma, Golap Kalita, Masaki Tanemura, Room temperature graphitization in solid phase reaction, 11th International Conference on Nanoscience and Nanotechnology 2019 (NANOSciTech 2019) 28 Feb. 2020-02 Mar 2020, Shah Alam, Selangor, Malaysia.

9) **Sahar Elnobi**, Subash Sharma, Mona Ibrahim Araby, Balaram Paudel Jaisi, Golap Kalita, M.E.Ayhan Masaki Tanemura, Novel approaches to grow graphene at lower temperatures, 11th International Conference on Nanoscience and Nanotechnology 2020 (NANOSciTech 2020), 28 Feb.–02 Mar. 2020, Shah Alam, Selangor, Malaysia.

10) **Sahar Elnobi**, Subash Sharma, Golap Kalita, Masaki Tanemura, Room temperature graphitization of carbon-Ni composite films, ISPlasma 2020/IC-PLANTS2020, 8–11 Mar. 2020, Nagoya university, Nagoya, Japan.

11) **Sahar Elnobi**, Subash Sharma, Golap Kalita, Masaki Tanemura, Room temperature graphitization using Ni nanoparticles as a catalyst, The 81st Japan Society of Applied Physics (JSAP) Autumn Meeting 2020, 8–11 September 2020, Japan.

12) **Sahar Elnobi**, Subash Sharma, Golap Kalita, Masaki Tanemura, Room temperature graphitization in solid phase reaction using Ni nanoparticles, 33rd International Microprocesses and Nanotechnology Conference MNC 2020, 9–12 Nov. 2020. Japan.